UNIVERSITÉ DE STRASBOURG

ÉCOLE DOCTORALE MSII (ED N°269)

laboratoire des sciences de l'ingénieur, de l'informatique

et de l'imagerie (ICUBE)-UMR 7357

THÈSE présentée par :

Guixian LIU

soutenue le : **23 Mai 2019**

pour obtenir le grade de : **Docteur de l'université de Strasbourg**

Discipline/ Spécialité : Mécanique/ Génie Civil

Modélisation aux éléments discrets du renforcement des bétons bitumineux par des grilles en fibre de verre.

THÈSE dirigée par :

M. CHAZALLON Cyrille	Professeur, INSA de Strasbourg
M. DAOUADJI Ali	Professeur, INSA Lyon

RAPPORTEURS :

M. DESCANTES Yannick	Chargé de recherche (HDR), IFSTTAR
M. CHEVOIR François	Directeur de recherches, IFSTTAR

AUTRES MEMBRES DU JURY :

M. RAGUENEAU Frédéric	Professeur, ENS Cachan
M. KOVAL Georg	Maître de conférences, INSA de Strasbourg

UNIVERSITY OF STRASBOURG

Discrete element modelling of asphalt concrete reinforced with fiber glass grids

by

Guixian LIU

A thesis submitted in partial fulfillment for the

degree of Doctor of Philosophy

in the

Doctoral School of MSII

Mai 2019

Acknowledgements

This PhD work is under the guidance of my supervisor Cyrille CHAZALLON, associate professor Georg KOVAL, and co-director Ali DAOUADJI. My deepest gratitude goes foremost to my advisers, Georg KOVAL, Cyrille CHAZALLON, and Ali DAOUADJI, who provided helpful advice, and continuous encouragement and support. Georg KOVAL daily accompanies me during my study and gives me instructive advice and useful suggestions. Cyrille CHAZALLON is a very wise and patient professor, who gives me crucial advices.

I would like to thank my colleagues in the Group of Civil Engineering and Energy at INSA Strasbourg, Saïda MOUHOUBI, Hossein NOWAMOOZ, Juan Carlos QUEZADA GUAJARDO, for their hospitality during my time as a Ph.D. student. Special thanks to my fellow Ph.D. students, Peng JING, Xiaofeng GAO, Loba SAGNOL, Hossein ASSADOLLAHI, Fujiao TANG, Anicet DANSOU, Laura GAILLARD, Lei MA and Léo COULON for all the great moments we shared.

I am also grateful to the China Scholarship Council (CSC) who provided me with a full scholarship for three-and-a-half years that guaranteed the smooth completion of my thesis.

Finally, I give my thanks to my family for their endless and unconditional encouragement and support. I will make great efforts to repay them and give love to my babies. I am grateful to my wife who has been carefully raising our babies during my PhD.

Résumé étendu

Contexte

Le béton bitumineux (AC) a été largement utilisé sur les couches supérieures des chaussées en raison de ses bonnes performances en termes de durabilité, de confort et de facilité de maintenance. D'après les études précédentes, le béton bitumineux est un matériau macroscopiquement isotrope et homogène, avec beaucoup de micro-vides, de micro-fissures et d'autres défauts. Ces éléments structurels sont soumis à la fatigue causée par des charges de trafic répétées, des variations de température (journalières et saisonnières), des tassements de fondation, etc., entraînant de l'endommagement et de la fatigue, et ses performances sont sérieusement affaiblies. L'augmentation du trafic associée aux coûts et aux problèmes environnementaux accroît la demande pour des chaussées à haute performance.

Les méthodes de renforcement ont été largement proposées par les chercheurs. Au cours de la dernière décennie, le renforcement par des grilles en fibre de verre a été appliqué pour améliorer la réponse mécanique des matériaux de structure de chaussée, ce qui a montrée son efficacité à réduire la fissuration et à prolonger la durée de vie des chaussée en béton bitumineux. Certaines propriétés de la fibre de verre, telles que sa haute résistance, sa rigidité et son endurance, ainsi que sa faible sensibilité à la température, en font une solution intéressante et rentable. Les recherches in-situ et en laboratoire mettent en évidence certaines preuves expérimentales qui nécessitent encore une compréhension plus approfondie avant de déboucher sur des principes de conception. Une série de tests a été réalisée pour révéler le mécanisme du renforcement de grille en fibre de verre. L'étude de la performance du béton bitumineux ainsi que de l'effet du renforcement repose sur deux aspects du comportement mécanique: l'endommagement sous charge monotone et sous charge de fatigue cyclique, qui seront examinés respectivement dans cette thèse.

Une analyse de la performance des grilles en fibre de verre sur la flexion des poutres en béton bitumineux a été réalisée par Arsenie et. al, basé sur des tests de flexion alternée à 4 points (4PB). Ses résultats ont ouvert la voie au projet *SolDuGri*, financé par l'Agence nationale de la recherche (ANR), où des tests à l'échelle réelle et de laboratoire ont été effectués. Parmi ces différentes

expériences, une attention particulière est accordée aux tests de fractionnement en coin d'échantillons de chaussée avec des interfaces contenant des grillees de fibres de verre.

L'interprétation des résultats des tests 4PB était basée sur une approche de mécanique des milieux continus: mécanique de l'endommagement, en fatigue. Cela a montré la complexité d'associer un comportement local fiable à des résultats d'échantillon en raison de la localisation de contrainte et de limite liés à l'existence de grilles de fibres de verre intégrés dans le béton bitumineux. Les essais de fendage par coin ont été analysés par la mécanique de la rupture, ce qui a donné de bonnes tendances initiales concernant les propriétés des matériaux et les résultats des tests. Le fait que le béton bitumineux soit composé d'agrégats liés par une matrice bitumineuse induit une structure irrégulière pour le matériau composite. Cette propriété peut avoir des conséquences sur le comportement mécanique, en particulier la rupture. La modélisation par éléments discrets (DEM) est un outil très utile pour étudier l'effet de ce désordre naturel et ses conséquences sur la réponse mécanique du matériau.

Généralement, la théorie du comportement à la rupture d'un matériau consiste en un critère de résistance à la rupture et la mécanique de la rupture élastique linéaire (LEFM). La LEFM devrait toujours venir en premier, afin d'étudier la mécanique des matériaux béton bitumineux en termes d'initiation et de propagation de fissures. Il s'applique à la rupture des matériaux fragiles. Cependant, pour d'autres matériaux, la description théorique devrait être déterminée sur la base des résultats expérimentaux, et la zone de traitement des fissures (FPZ) peut expliquer certains phénomènes qui ne sont pas résolus par la LEFM en termes de zone de micro-fissure et de vitesse de restitution d'énergie. La fatigue des matériaux est un autre comportement mécanique. Dans cette thèse, la durée de vie en fatigue est caractérisée par la dégradation de la rigidité, et la théorie concernant l'endommagement par fatigue et la durée de vie en fatigue sera revue.

Les défauts du béton bitumineux peuvent affecter le comportement mécanique, ainsi dans l'étude numérique, leur représentation devrait être bien prise en compte. En attendant, les propriétés physiques macroscopiques doivent être reproduites. De ce point de vue, la méthode des éléments discrets (DEM) est une méthode numérique idéale sur laquelle l'accent sera mis lors de la révision de la méthode numérique. Le modèle de zone cohésive (CZM) est examiné en particulier pour l'incorporation à DEM, ce qui résout la propagation de fissure avec la FPZ sous charge monotone. La simulation numérique de l'endommagement de

fatigue nécessite également un modèle de fatigue, qui devrait bien reproduire la durée de vie en fatigue et l'évolution de l'endommagement lors d'un chargement de fatigue en DEM.

Plan de Mémoire

Objectif de la recherche

Le présent travail explorera les capacités d'un environnement DEM, notamment une description plus fine du matériau concernant son hétérogénéité interne pour simuler des échantillons de béton bitumineux et l'effet des grilles en fibres de verre sur la réponse mécanique des structures. Afin de mieux comprendre les résultats des tests de laboratoire (WST et 4PB), les objectifs principaux de cette thèse sont décrits ci-dessous: 1) Simulation en DEM du comportement cohérent du béton bitumineux en termes d'élasticité, de résistance et de ténacité. 2) Développement d'un modèle d'éléments discrets qui reproduit le comportement à la rupture du béton bitumineux sous charge monotone et l'extension à la description de la rupture de l'interface entre les grilles en fibres de verre et le béton bitumineux en mode ouverture.

Organisation de la thèse

La présente étude est composée des parties suivantes: Le premier chapitre concerne l'introduction et le contexte de mon étude. Le deuxième chapitre présente une revue de la littérature. Le comportement mécanique du béton bitumineux et des grilles en fibre de verre est présenté. Les méthodes les plus utilisées pour la modélisation théorique de la rupture sont introduites, notamment la mécanique de la rupture linéaire élastique, les notions de la FPZ. Ainsi, les méthodes numériques d'analyse de l'endommagement par fissuration et par fatigue sont passées en revue, notamment l'application de la méthode des éléments discrets (DEM). Le chapitre 3 aborde les conception de base de l'analyse par éléments discrets: génération de matériau, étalonnage de paramètres et identification de la ténacité à l'aide d'un contact linéaire collé.

Le chapitre 4 concerne la rupture monotone des matériaux en béton bitumineux comprenant l'interface avec les grilles en fibre de verre. L'application d'un modèle de contact cohésif adapté à ce type de matériau est présentée. L'essai de fendage par coin (WST) avec l'interface sont décrits (configuration expérimentale et simulations). L'analyse des expériences de WST associée à une étude paramétrique

du modèle à éléments discrets permet d'identifier le mécanisme de rupture, un modèle simplifié pour l'interface est ensuite proposé.

Au chapitre 5, la rupture par un chargement de fatigue alternatif est discutée. Une loi d'endommagement local est appliquée au niveau des contacts et adoptée pour décrire le comportement en fatigue du béton bitumineux. Le test de flexion à 4 points (4PB) adopté pour identifier l'effet des grilles de fibres de verre en fatigue est présenté. La configuration de la simulation et la représentation 2D des grilles sont détaillées. Une étude paramétrique du modèle d'éléments discrets associée à la comparaison avec les résultats expérimentaux permet d'identifier l'effet des grilles de fibres de verre sur la durée de vie en fatigue des échantillons.

Enfin, le chapitre 6 résume les résultats et conclusions de la présente étude, suivies des perspectives pour les travaux futurs.

Le comportement d'élasticité et de rupture dans le DEM

Les matériaux sont modélisés par un ensemble de particules assemblées de manière aléatoire. Une méthode une méthode dynamique de mettre à l'échelle le rayon des particules pour libération de contraintes internes a été utilisée pour induire une structure interne presque isotrope et homogène avec des vides internes réduits. Une étude paramétrique permet de relier les paramètres de contact (module de contact E_{cmod} et rapport de rigidité $k_{ratio} = k_n/k_s$) aux paramètres du matériau (module de Young E et coefficient de Poisson ν en élasticité, exprimés comme suit:

$$\nu = 0.1645 \times ln\left(\frac{k_n}{k_s}\right) + 0.0913, \tag{1}$$

$$E = \left(-0.1793 \times ln\left(\frac{k_n}{k_s}\right) + 0.8070\right) E_{cmod}, \tag{2}$$

où $0.1 < \nu < 0.34$ et $0.5GPa < E < 65GPa$ contiennent la plage habituelle du coefficient de Poisson et du module de Young du béton bitumineux.

Le comportement quasi-fragile est limité par deux mécanismes de rupture: l'un lié au niveau de contrainte et l'autre au facteur d'intensité de contrainte. Ces deux mécanismes sont généralement associés à deux propriétés du matériau, la résistance à la traction et la ténacité, respectivement. Une procédure de calibration basée sur l'analyse de la résistance nominale d'échantillons pré-fissurés a permis d'identifier la relation entre ces paramètres de matériau et les paramètres

de contact: résistance normales et tangentielles (f_n et f_s) et le rayon moyen $\bar{R}$ de la particule.

Les relations normales dues à l'étalonnage sont exprimées comme suit,

$$\Sigma^t = \frac{f_n^{max}}{\bar{R}t} \times \alpha, \tag{3}$$

$$K_{IC} = \frac{f_n^{max}}{t\sqrt{\bar{R}}} \times \beta, \tag{4}$$

où α et β sont deux variables sans dimension liées à la configuration de l'assemblage des particules dans DEM.

L'identification de α et β pour les assemblages aléatoires est présentée à l'aide d'une méthode énergétique à la figure 1, dans laquelle une transmission évidente du critère de contrainte à la LEFM est observée pour les résultats de la simulation DEM.

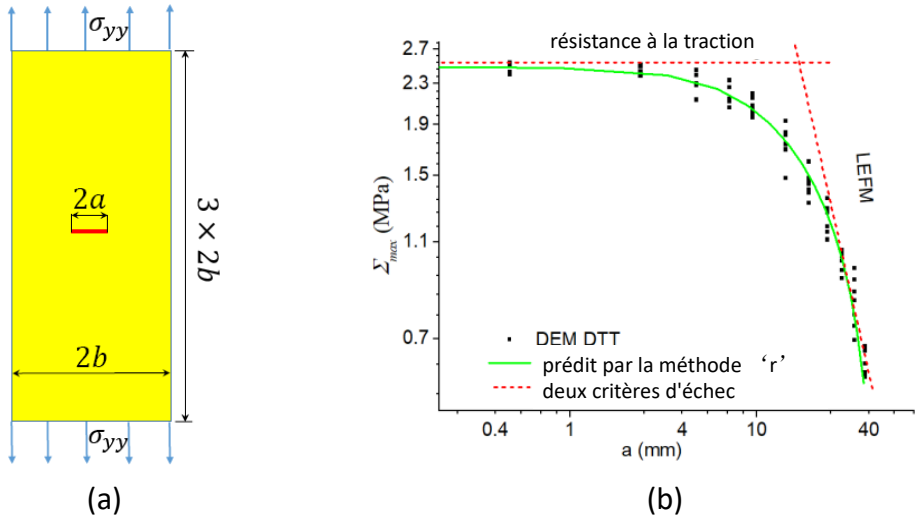

Figure 1: Résistance nominale Σ_{max} en fonction de la taille initiale de la fissure a. La ligne continue est la prédiction donnée par la formulation énergétique pour la résistance à la traction $\Sigma^t = 2.4\,MPa$, la ténacité $K_{IC} = 0.4\,MPa \times m^{0.5}$ et le paramètre $r = 2.5$.

Le contrôle des paramètres de rupture (quasi-fragile) a été vérifié en comparant les résultats de simulations de fractionnement en coin avec la prédiction de la mécanique de la rupture élastique linéaire. Sur la figure 2, le bon accord entre la

simulation et la prévision LEFM permet de vérifier la consistance des propriétés de rupture de l'ssemblage aléatoire dans DEM.

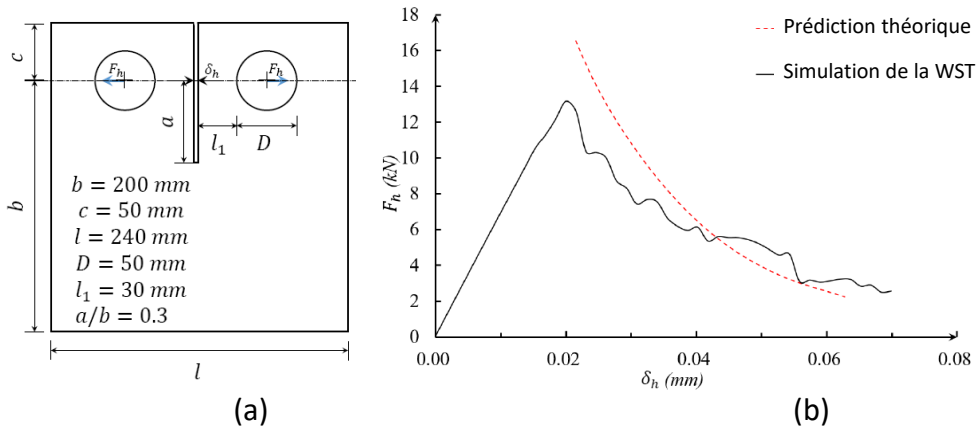

Figure 2: (a) Géométrie de la WST. (b) Le résultat de la simulation et l'ajustement par LEFM

Comportement à la rupture du béton bitumineux avec (sans) renforcement de la grille en fibre de verre sous charge monotone en mode d'ouverture

Les limites d'une approche quasi fragile sur la description du béton bitumineux sont discutées. Le taux de restitution d'énergie lors de la rupture (monotone) d'échantillons de béton bitumineux (WST) est beaucoup plus élevée que la prédiction de la mécanique de la rupture élastique linéaire, qui est basée sur la valeur de la ténacité. Cette non-linéarité associée à la rupture peut être expliquée par la notion de la zone de traitement des fissures (FPZ) présentée à la figure 3a, où nombreuses micro-fissures existent à la pointe de la macro-fissure. Le modèle de zone cohésive est généralement adopté pour étudier numériquement la FPZ, comme le montre la Figure 3b.

En termes de modélisation par éléments discrets, une loi de contact cohésif bilinéaire a été mise en œuvre, dans laquelle le contrôle de l'énergie de rupture est clairement introduit en tant que paramètre. En conséquence, des résultats de simulation réalistes du béton bitumineux sont obtenus à la figure 4.

L'analyse subséquente des essais de fractionnement en coin avec des interfaces entre le béton bitumineux et les grilles de fibres de verre a montré que le processus

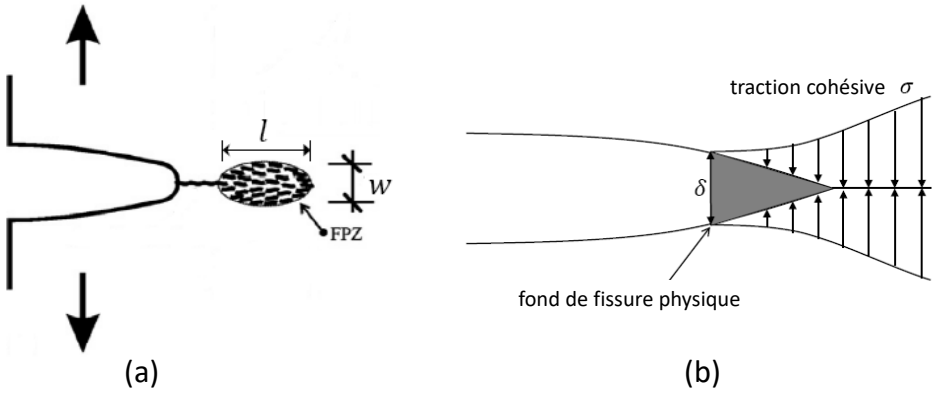

Figure 3: (a) FPZ à la macro fissure. (b) La zone de cohésion en avant du fond de fissure.

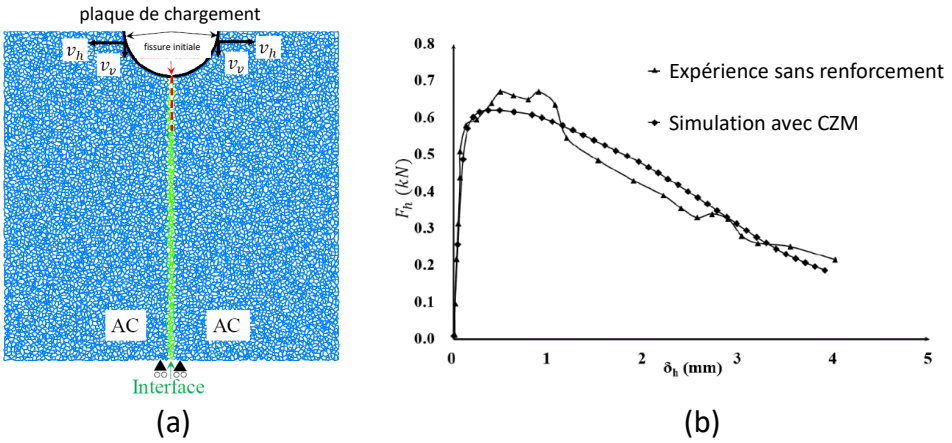

Figure 4: (a) Géométrie de la WST. (b) La comparaison entre le résultat d'expérience et de simulation.

de rupture est dominé presque intégralement par les propriétés mécaniques des interfaces. Le béton bitumineux se comportant comme un corps rigide a conduit à une modélisation simplifiée du WST basée uniquement sur les trois paramètres: rigidité, résistance et vitesse du taux de restitution d'énergie de l'interface. La figure 5 a présente le modèle d'interface. Les interfaces liées sont divisées en petits éléments et traitées comme des ressorts. La force f^j de chaque ressort suit une loi de séparation par traction bilinéaire contrôlée par la déformation du ressort. La comparaison de ce modèle d'interface a montré un bon accord avec les résultats expérimentaux. Ainsi, les propriétés de rupture (résistance à la traction Σ^t et l'énergie du rupture G_{IC}) peuvent être identifiées à l'aide du modèle d'interface proposé, comme illustré à la Figure 5b.

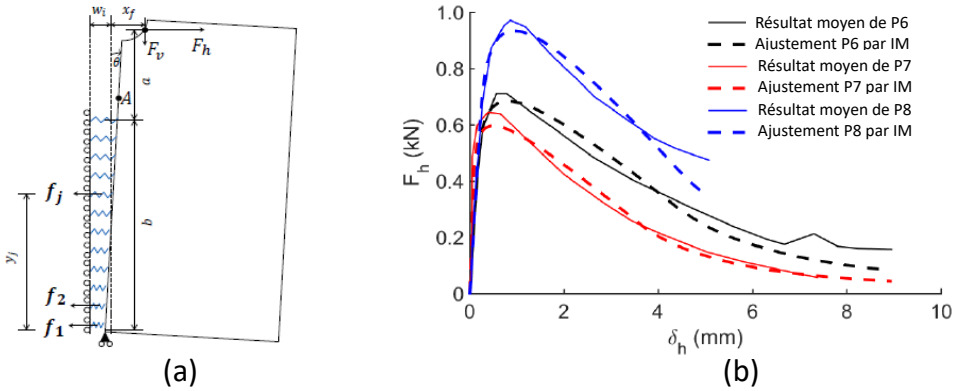

Figure 5: (a) Géométrie du modèle d'interface. (b) Comparaison des expériences et ajustement du modèle d'interface.

Comportement à la fatigue du béton bitumineux (non) renforcé avec essai de flexion en 4 points

Un modèle de fatigue alternée pour le béton bitumineux a été mis en œuvre dans la méthode des éléments discrets. Il est démontré qu'un modèle de contact d'endommagement décrivant les phases *I* et *II*, associé au désordre naturel de la structure interne du matériau dans le DEM, est capable de décrire l'ensemble du comportement en fatigue (phases *I*, *II* et *III*) à l'échelle d'échantillons. Sur la figure 6, les essais de perte de rigidité réalisées par Arsenie sont bien reproduites par le modèle de fatigue imposée dans les simulations DEM. La phase *III* apparaît comme un effet de structure se manifestant même dans des conditions aux limites uniformes, caractérisée par une perte d'homogénéité induite par la concentration de défauts et une localisation de la déformation, comme illustré à la figure 7.

Des simulations d'essais de flexion en 4 points ont ensuite été effectuées pour analyser l'influence des grilles en fibres de verre sur la réponse en fatigue de poutres composites.

Les incréments d'endommagement par cycle ont été définis par l'amplitude de déformation. Les cycles alternatifs ont été numériquement remplacés par une flexion statique des échantillons, ce qui a accéléré le calcul et a permis d'étudier le comportement en fatigue sous un nombre élevé et réaliste (10^5 à 10^6) de cycles. Une étude paramétrique et l'étalonnage des 3 paramètres de fatigue du modèle discret pour les essais 4PB ont montré les capacités du modèle à reproduire les

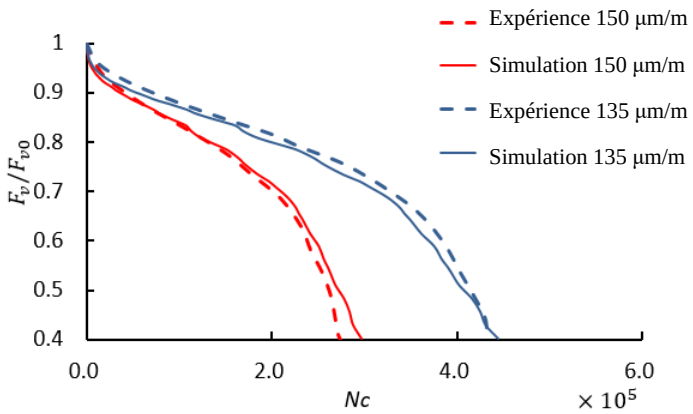

Figure 6: Comparaison d'expériences et de simulations sous différents niveaux de contrainte.

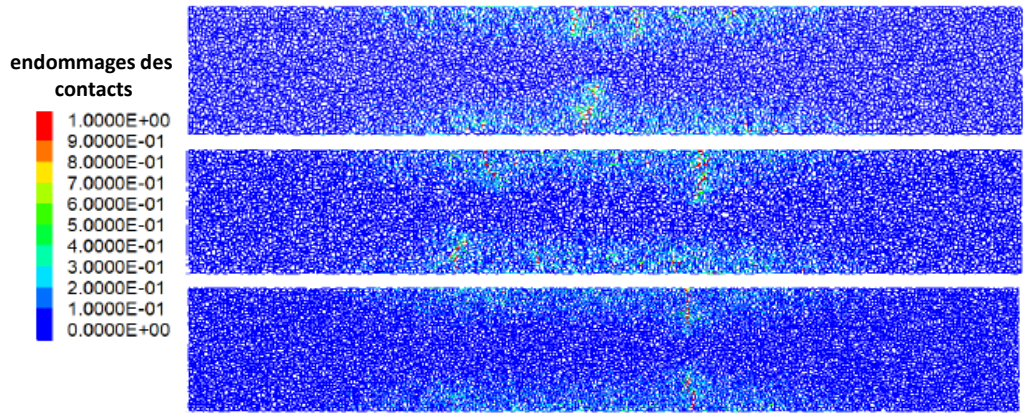

Figure 7: Cartographies des endommagements de 3 échantillons numériques à la dégradation de la rigidité $F_v/F_{v0} = 0.4$.

résultats expérimentaux d'échantillons de béton bitumineux. Ainsi, les effets des réseaux de fibres ont été analysés sous deux angles: renforcement normal et interface. Les renforcements normaux étaient représentés par des contacts élastiques complémentaires au même emplacement des grilles de fibres et présentant la même rigidité comme illustrée à la figure 8.

L'avantage de cette approche bidimensionnelle est de permettre une propagation libre de défauts à travers la grille de fibres de verre (comme cela se produit en réalité). Les vérifications de la modélisation des fibres sont effectuées sous charge monotone et charge cyclique avec des simulations 4PB, les résultats étant présentés à la figure 9. Les résultats de la simulation indiquent que les ren-

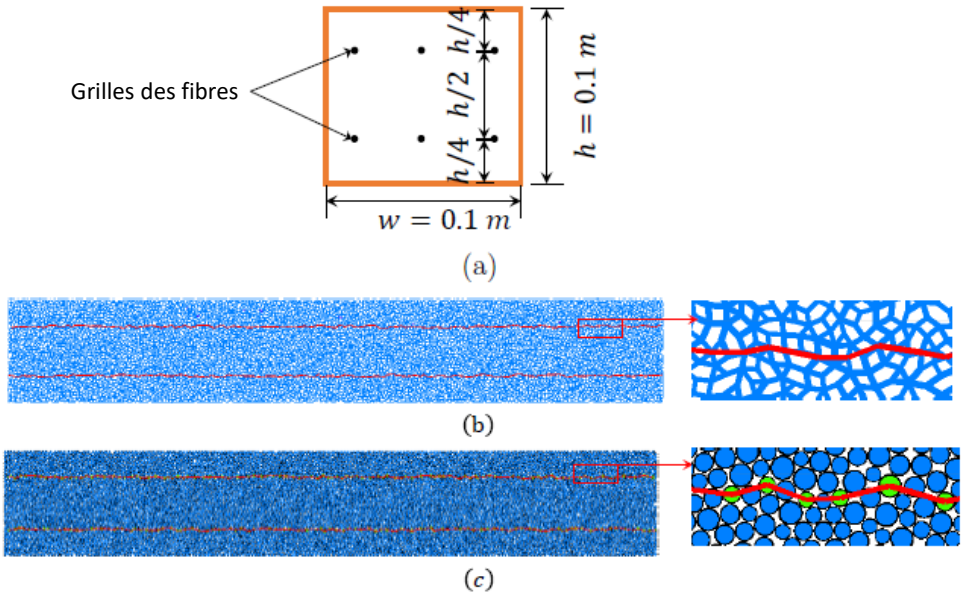

Figure 8: (a) Coupe transversale des échantillons renforcés. Représentation des barres de la grille de fibres en tant que (b) contacts élastiques supplémentaires et (c) connexion de particules dans la même couche.

forts sont activés à proximité de points très endommagés, où la déformation est localisée. La faible quantité de fibres n'est suffisante pas pour expliquer individuellement l'amélioration de la durée de vie en fatigue observée dans les expériences.

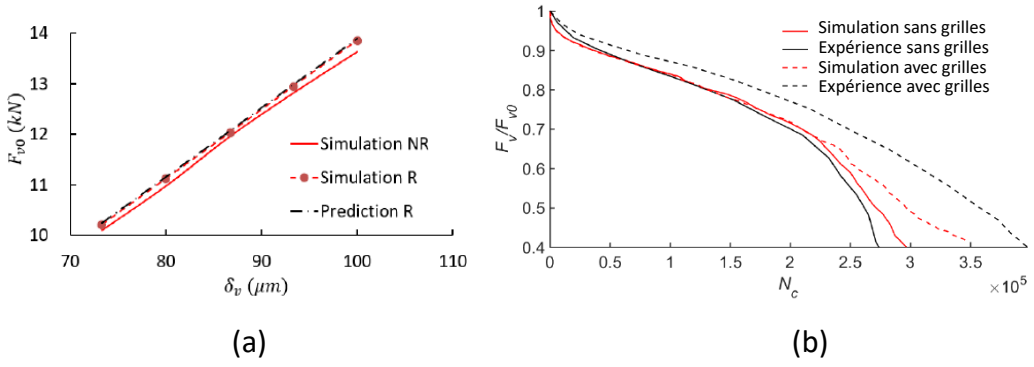

Figure 9: (a) Vérification de la modélisation de la fibre sous charge monotone de 4PB. (b) Comparaison des simulations (non) renforcées et des expériences d'Arsenie

Sur la figure 10, l'interface est caractérisée par une mince couche de particules avec une rigidité élastique moindre pour induire un glissement relatif entre deux

couches adjacentes. La contribution normale de cette couche est négligeable compte tenu de la faible section transversale de la couche d'interface.

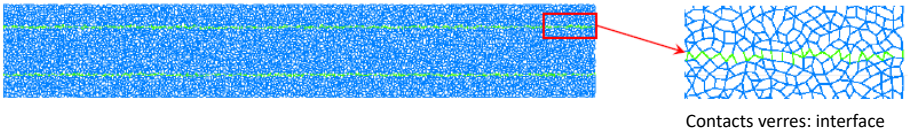

Figure 10: Modélisation d'interface en simulation avec une couche de contacts en verres.

Cependant, le glissement induit par l'interface peut entraîner une redistribution de la contrainte normale avec une réduction des valeurs maximales, ce qui allonge la durée de vie en fatigue de l'ensemble de la poutre malgré sa rigidité initiale. Compte tenu de l'effet couplé des renforts et de l'interface, la redistribution de la contrainte a pour conséquence d'augmenter l'endommagement près de la position des renforts, ce qui améliore l'efficacité des renforts. Enfin, la comparaison entre simulations et expériences a montré la cohérence du modèle et les tendances indiquées par les simulations comme présenté à la figure 11.

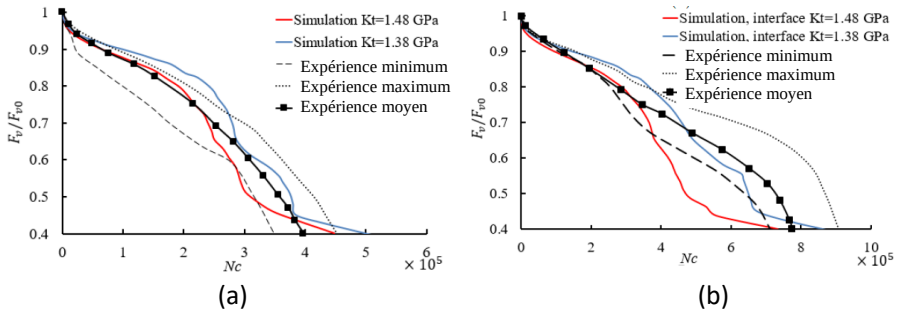

Figure 11: Comparaison de expériences et simulations d'effet collectif de grille de fibres et interface.

Conclusions et perspectives

Conclusions

Dans cette thèse, la réponse mécanique du béton bitumineux (AC) sous des chargements monotones et en fatigue a été modélisée par la méthode des éléments discrets. Sur la base de ce comportement des matériaux, l'effet des grilles en fibres de verre associées au béton bitumineux est pris en compte et son apport mécanique a été analysé.

Premièrement, la modélisation en DEM a été étudiée de manière paramétrique. La comportement des matériaux quasi-fragiles a été vérifiée par des essais de traction et des essais de fractionnement. Ensuite, la simulation de WST a mis en évidence l'effet décisif de l'interface qui a dominé la rupture des assemblages, de sorte que le modèle d'interface a été simplifié et utilisé pour identifier les propriétés de rupture du béton bitumineux renforcé par des grilles en fibres de verre.

Les essais de fatigue 4PB ont été étudiés avec du béton bitumineux (non) renforcé. Un modèle de fatigue identifiant les phases *I* et *II* a été adopté avec DEM, lequel a présenté la phase *III* naturellement dans DEM. L'effet de la grille est devenu distinct lorsque les fissures traversent la grille et les échantillons renforcés présentent une durée de vie en fatigue insuffisante en comparaison avec les expériences de AC renforcé. L'effet collectif de l'interface et de la grille présente une bonne cohérence avec les expériences.

Perspectives

Les modèles numériques développés et discutés dans cette thèse ont indiqué certaines tendances, clarifié certains résultats expérimentaux et suscité des questions. Pour tous les calculs, la granularité des matériaux simulés est restée la même.

Au chapitre 3, l'effet de la taille moyenne des particules a été augmenté dans la relation entre la résistance à la traction et la ténacité d'un matériau quasi-fragile. Comme indiqué à l'annexe B, le comportement quasi-fragile peut également dépendre de la transition entre les mécanismes de rupture fondés sur la résistance et la ténacité, caractérisée par le paramètre r. Une analyse physique de l'effet de la granularité sur la rupture des échantillons pré-fissurés peut donner une explication physique aux effets de taille en cas de rupture quasi-fragile.

Les modèles d'endommagement ont été orientés de manière à simuler le comportement du béton bitumineux et ses interactions avec les grilles en fibres de verre. Cependant, les approches en charges monotones et répétées peuvent être étendues à d'autres (géo) matériaux et à d'autres (géo) grilles.

Certains effets importants liés au comportement mécanique du béton bitumineux n'étaient pas explicitement isolés. Un aspect important à inclure dans la modélisation est l'identification des contributions élastiques et visqueuses sur la réponse du matériau. Les essais de fatigue sont généralement effectués à des fréquences relativement élevées, ce qui affecte la réponse du matériau. La

température est également un paramètre à prendre en compte à l'avenir, qui affecte la viscosité de l'asphalte en laboratoire et dans les structures réelles.

Les essais de fatigue associés aux échantillons de béton bitumineux sont généralement pilotés en déformation. Le comportement de renforcement de la grille de fibres de verre semble être activé à des niveaux d'endommagement élevés et, par conséquent, à de faibles niveaux de rigidité de l'échantillon. Les essais controlé par le stress pourraient éventuellement permettre de mieux montrer la contribution de la grille de fibres aux niveaux de rigidité résiduels.

Les propriétés des grilles en fibres de verre ont été considérées comme parfaitement élastiques dans tous les calculs. La grille elle-même présente une rigidité à peu près constante lors des essais de fatigue avec des niveaux de déformation comparables à ceux de l'essai de flexion. Cependant, le comportement de la liaison entre la fibre de verre et le béton bitumineux n'est pas forcément indépendant du nombre de cycles. Des tests d'arrachement répétés peuvent donner des informations importantes sur le comportement en fatigue de cette connexion. Le comportement normal et, en particulier, tangentiel du l'interface béton bitumineux / grilles soumis à la fatigue constitue également un apport important pour la modélisation des poutres composites. Une interface qui présente une perte de rigidité considérable lors des tests peut contribuer de manière très différente de celle proposée par les résultats numériques de ce travail. Malgré toutes les incertitudes actuelles quant à la caractérisation des interfaces, le contrôle des propriétés de ces couches minces semble être un moyen de caractériser les performances en fatigue des éléments structuraux dans le béton bitumineux.

Contents

List of Figures

List of Tables

Chapter 1

Introduction

Contents

The work of this thesis was carried out at the National Institute of Applied Sciences of Strasbourg (INSA de Strasbourg) and was funded by the China Scholarship Council (CSC). The study is related to the project *SolDuGri*, funded by the French National Research Agency (ANR).

This introduction includes the general background, research objectives and the outline of the thesis.

1.1 General background

Asphalt concrete is widely used on the upper layers of road pavements. These structural elements are subjected to fatigue by repeated traffic loads, (daily and seasonal) temperature variations, foundation settlement, etc. The increasing traffic associated to costs and environmental issues raises the demand for high performance pavements.

In the last decade, the reinforcement by fiber glass grids has been applied to improve the mechanical response of pavement structure materials. Some properties of the fiber glass like high strength, stiffness and endurance, and low sensitivity to temperature makes it an interesting and cost-effective solution. Field and laboratory research points out some experimental evidences which still request a deeper understanding before leading to design principles.

An analysis of the perfomance of fiber glass grids on the deflection of asphalt

concrete beams was performed by Arsenie et. al [1], based on 4-point alternate bending (4PB) tests. Her results opened the path for the project *SolDuGri*, funded by the French National Research Agency (ANR), where tests in real and laboratory scales have been performed. Among these different experiences, a special attention is given to wedge-splitting tests (WST) of pavement samples with interfaces containing fiber glass grids.

The interpretation of the results of 4PB tests was based on a continuum mechanics approach: damage mechanics, in fatigue. It has shown the complexity on associating reliable local behaviour to sample results due to the localization of strain and boundary effects related to the existence of fiber grids embedded in the asphalt concrete. The WST was analysed through fracture mechanics, which presented good initial trends relating material properties and test results.

The fact that asphalt concrete is composed by aggregates binded by a bituminous matrix induces an irregular structure to the composite material. That property may have consequences on the mechanical behaviour, specially the rupture. Discrete element modelling (DEM) is a very useful tool to investigate the effect of this natural disorder and its consequences on the mechanical response of the material.

1.2 Research objectives

The present work will explore the capabilities of a DEM environment, notably a finer description of the material concerning its inner heterogeneity to simulate asphalt concrete samples and the effect of the fiber glass grids on the mechanical response of the systems. In order to build a better understanding on the results of the laboratory tests (WST and 4PB), the main objectives of this thesis are described below:

1) Simulation in DEM of physically consistent behaviour of the asphalt concrete in terms of elasticity, strength and toughness.

2) Development of a discrete element model which reproduces the rupture behaviour of asphalt concrete under monotonic load and the extension to the description of the rupture of the interface between glass fiber grids and the asphalt concrete in opening mode.

3) Development of an alternate fatigue model in a discrete element approach adapted to asphalt concrete behaviour and numerically efficient to analyse the material behaviour during a very large number ($10^5 - 10^6$) of loading cycles.

4) Evaluate the contribution of the fiber glass grids under fatigue loading (4PB geometry) and identify the mechanisms inducing the observed improvement on the fatigue performance of the composite beams.

1.3 Organization of the thesis

The present study is composed by the following parts:

The first chapter presents a literature review. The mechanical behaviour of the asphalt concrete and the fiber glass grids are presented. The most used methods for theoretical modelling of rupture are introduced, including linear elastic fracture mechanics, notions of fracture process zone and fatigue. Thus, the numerical methods for fracture and fatigue damage analysis are reviewed, where the application of discrete element method is emphasized.

Chapter 3 discusses the basic elements of the discrete element analysis: material generation, calibration of parameters, and identification of the fracture toughness with a bonded linear contact.

Chapter 4 concerns the monotonic rupture of asphalt concrete materials, which includes the interface with fiber glass grids. The application of a cohesive contact model adapted to this type of material is presented. The wedge-splitting tests of the interface are described (experimental and simulations setup). The analysis of wedge-splitting experiences associated to a parametric study of the discrete element model allows the identification of the mechanism of rupture and a simplified model for the interface is then proposed.

In Chapter 5, the failure by alternate fatigue loading is discussed. A local damage law is implemented at the contact level and adopted to describe the asphalt concrete fatigue behaviour. The 4-point bending (4PB) test adopted to identify the effect of the glass fiber grids in fatigue is presented. The simulation setup and the 2D representation of the grids are detailed. A parametric study of the discrete element model associated to the comparison with experimental results allows the identification of the role of the fiber grids on the fatigue life of the samples.

Finally, Chapter 6 summarizes the conclusions and findings of the present study, which are followed by the perspectives for future work.

Chapter 2

Literature review

Contents

2.1 Introduction

Asphalt concrete (AC) has been widely used in pavement due to its good performance in terms of durability, comfort and an easy maintainability. From previous studies, the asphalt concrete is macroscopically isotropic and homogeneous material, with plenty of micro voids, micro cracks and other defects. However, different types of load are applied to the pavement materials, resulting in the damage and fatigue, and its performance is seriously weakened. The reinforcement methods have been widely proposed by the researchers. Of these methods, the fiberglass grid has been verified to be effective in reducing the fracture and prolonging the service life of AC pavement. A series of tests have been done to reveal the mechanism of fiber glass grid reinforcement. The study of AC performance as well as the effect of reinforcement lies on two aspects of the mechanical behaviour: the damage under the monotonic load and cyclic fatigue load, which will be reviewed respectively in this chapter. The wedge-splitting test and 4-point bending test are emphasised since they are studied in the following chapters.

Generally, the theory of material fracture behaviour consists of a strength failure criterion and the linear elastic fracture mechanics (LEFM). LEFM should still come firstly, in order to study the AC material mechanics in terms of the crack initiation and propagation. It applies for the fracture of brittle materials. However, for other materials, the theoretical description should be determined

based on the experimental results, and the fracture process zone (FPZ) may explain some phenomena that can not be solved by LEFM in term of the micro crack zone and energy release rate. The material fatigue is another mechanical behaviour. In this chapter, the fatigue life is characterized by the stiffness degradation, and the theory with respect to the fatigue damage and fatigue life will be reviewed.

The defects in AC material may affect the mechanical behaviour, thus in the numerical study, their representation should be well considered somehow. Meanwhile, the macroscopic physical properties should be reproduced. From this point of view, the discrete element method (DEM) seems to be an ideal numerical method which will be emphasised during the review of the numerical method. The cohesive zone model (CZM) is reviewed especially for the incorporation with DEM, which solved the fracture propagation with FPZ under monotonic load. The numerical simulation in fatigue damage also requires the fatigue model, which should well reproduce the fatigue life and the damage evolution during fatigue load in DEM.

2.2 Asphaltic pavement materials

2.2.1 Asphalt concrete

The asphalt concrete (AC) is mainly a mixture of aggregates and bitumen as binder. It is characterized by good toughness, good compression resistance, good tension resistance and bad thermostability, and it is convenient for installation and maintenance. The AC pavement also contributes to the comfortable and quiet driving experience, thus widely adopted in the road pavement, especially for the high-type pavement.

The performance of asphalt concrete is the collective effect of aggregate and bitumen. The aggregate usually have high stiffness and strength and they interlock each other by internal friction and locking force. The aggregates are the principal load-supporting components of an AC pavement. Different types of aggregates have been adopted such as sand, gravel, crushed stone or rock dust. The aggregate size, grade, shape, toughness, soundness, surface cleanliness and surface texture are important for the AC performance.

The overall asphalt binder includes bitumen (the petroleum-based asphalt, coal tar, and natural tar) as well as any material (mineral powder, fiber glass) added

to modify the original asphalt properties. It helps to provide good elasticity, resilience, high plasticity under the temperature variation, which contributes to comfort and safety of driving and durability of pavement.

There are two types of asphalt mixes: hot-mix and cold-mix. Hot-mix asphalt (HMA) is more commonly used, while cold-mix asphalt (generally mixes made with emulsified or cut-back asphalts) is usually used for light to medium traffic secondary roads, or for remote locations or maintenance use. During fabrication process, the void content and compaction level of asphalt concrete influences the performance, based on the study by [2].

Although the AC pavement presents several advantages in the performance comparing to the cement concrete, it still needs some improvements due to particular service conditions. There are several causes which lead to the pavement distress and may produce movements at discontinuously and inhomogeneously. These causes are: (a) low temperature contraction, (b) daily temperature cycles, (c) traffic loads and (d) high temperature deformation, which results in cracking and deformation.

Low temperature leads to the contraction in asphalt concrete. And it also results in lower plasticity and increases the stiffness of asphalt concrete. Consequently, the AC pavement layer is easier to crack. High temperature increases the flexibility of the asphalt concrete, thus leading to rutting problem in AC pavement layer. The heavy and cyclic traffic loads and the temperature loads directly act on the pavement, which leads to the deformation and damage of the AC pavement layer.

2.2.2 Reinforcement of asphalt concrete

AC pavement encounters a great danger of fatigue and crack propagation resulting from the repeated traffic load and climatic factors as mentioned above. When the service life is approached, the pavement suffers from an increasingly serious damage and becomes unusable for service. Thus it is an important issue to study the methodology to prolong the service life and load resistance performance of asphalt concrete. The researches cover the following aspects:
1) the type, size and volumetric content of aggregate, the type of asphalt;
2) asphalt mixed with special materials, fiber glass [3], polyester fiber [4] for example;
3) imposing grid layer for reinforcement between two AC layers.
For these points, the second and the third items can deal with the reinforcement.

Wu [5] performed a series of laboratory tests on asphalt concrete with fiber glass, the results suggested that fiber glass increased the bending failure strain but had no effect on the bending failure strength. In Guo's study [3], the fiber glass could decrease the rutting of traffic load. And under indirect tensile fatigue tests, the fatigue life had a clear improved, but less than 1.5 times. In Ge's research [6], different materials (i.e. modified asphalt, modified emulsified asphalt, fiber glass reinforced modified emulsified asphalt and modified fiber glass reinforced asphalt) were adopted for the interface between asphalt concrete and cement concrete. The result showed that all the specimens with fiber glass reinforcement presented a longer fatigue life. The problem is that it is difficult to compact even for short fibers.

Fiber glass grid is an ideal material placed between 2 layers of asphalt concrete, which has been used for decades of years, see Figure 2.1. From the literature, it is indicated that fiber glass grid helps to distribute the stress and prevent crack propagation from top to bottom and the opposite direction [7], to dissipate the stress concentration due to the reflect crack and fatigue crack, and to function as moisture barriers [8], which significantly reduces the damage and improves the service life. However, up to now, the choice of the appropriate grid (mesh size, tensile strength) and its optimal location in the pavement system are mainly based on experience from lab experiments and in-situ observations [8].

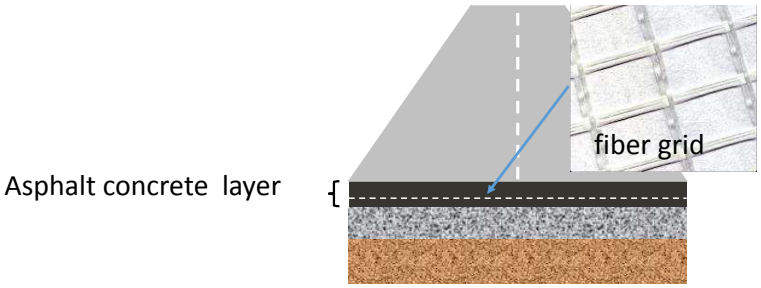

Figure 2.1: Fiber glass reinforcement in asphalt concrete.

2.2.2.1 Fiber glass grid

The present fibers are of different types: fiber glass, boron fiber, carbon fiber, organic fiber, oxidized fiber and silicon carbide fiber. The fiber glass is widely used for reinforcement with the caoutchouc reinforcement. The industrial manufacture of fiber glass began at 1930s [9] and the association of Owens Corning was built in the same period. The fiber glass possesses a good strength due to the shape

and it is of high productive efficiency.

The synthetic resin is employed as the matrix of the composite due to the advantages and properties listed below: (a) the temperature of utilisation is lower than that of metals, (b) good resistance in the corrosive media, (c) the low mechanical modulus that facilitates the transfer of charge in the fibers. It is categorised by thermoplastic and thermosetting resin, and the former one is mostly used in the fiber glass.

The fiber glass grid is the material composed by the filament of fiber glass of diameter from $10 \sim 30\,mm$, glued by a kind of synthetic resin. It has been used as the reinforcement in the road engineering since 1960s, experiences an increasing utilization in 1990s and nowadays it is used systematically and effectively [1]. Up to now, there is not the optimised position for the application of fiber glass grid in the pavement structure [8]. Since the fiber glass grid is used to stop the fracture propagation, it should be placed at the depth where the pavement was affected by the distresses seriously. However, some researchers stated that the crack may initiate at either the bottom or the top of the pavement layer, and propagates to the opposite. In practice, the fiber glass grid is usually placed in the bottom of the AC layer, between the AC layers and base course pavement layers, with a bitumen emulsion layed on the top of the base course layer. The interface plays the significant effect on the expected performance, thus the fiber glass grid should be well glued [1].

2.2.2.2 Reinforcement mechanism by fiber glass grid for asphalt concrete

Button and Lytton [10] summarized this reinforcement mechanism as follows:
1) The crack starts to propagate from its original position upward until it reaches the reinforcement layer due to thermal and traffic loading or uneven soil movements;
2) If the interlayer is stiff enough (stiffer than the surrounding materials), the crack will turn laterally and move along the interface until its energy is exhausted.
3) Based on this mechanism, a reinforcement interlayer may contribute to the structural resistance capacity of the pavement.

Evaluation of fatigue resistance is mostly based on bending tests on grid reinforced beams under cyclic loading. There are 2 aspects that influence the effect of reinforcement: interaction between the reinforcing product and surrounding

materials (e.g. bonding interface, interlocking with the aggregates), and properties of reinforcing material (e.g. tensile strength).

The fiber glass grid has regular apertures which allows the interlocking effect. The interlocking phenomena restrains lateral movement of the aggregates, and thus greatly decreases shear potential. If the aperture size is excessive large, the stress dissipating capability is weakened, while a fine grid with quite small apertures reduces the interlocking and also has bad reinforcement effect [11, 12].

When it comes to the test method, the adhesion test is normally conducted with regard to the stiffness and strength issues, with monotonic load [13–15]. The fatigue resistance test is used to investigate the damage process (crack initiation, propagation) under repeated traffic loading and thermal load [16–18]. The three point bending test by [19] proved that the application of the fiber glass grid increased 45% of the bending strength.

In the early studies, researchers found the poor performance of grid resulting from de-bonding (or de-lamination) for the glass fiber grid composite forming interface between two AC layers [20, 21], although it can be improved by the compaction from the traffic load during service [22]. To mitigate the debonding for the interface, fiber glass grids are generally used with a tack coat, which can improve the initial tensile performance [23, 24]. In the study of [24], adhesion tests were performed with different types of tack coats, different fracture energies were obtained correspondingly. To strengthen this improvement, a light polyester nonwoven was applied working together with tack coat, meanwhile permitting the aggregate pass thorough easily and thus ensuring interlocking. Recently, a new material has been developed to replace the traditional tack film, which is partially melted at the typical asphalt melting temperatures during the application, so that it significantly simplifies the installation of grids [8]. Although some encouraging results have been drawn, there are still some points to be noticed. Their main disadvantages may be the bonding with the asphalt material and difficulties to recycle the reinforced asphalt materials [8]. The cost of fiber glass should be comparable with the regular maintenance cost without reinforcement, since cost-performance should be carefully considered.

2.3 Material mechanical behaviour

Material mechanical properties consist of elasticity, plasticity, strength, toughness, fracture toughness, fatigue damage. Generally, for different materials and

different applications, one or multi properties need to be considered and studied. Some properties are sensitive to the load pattern and the temperature. For example, the strength of the materials may depends on the loading rate. The material plasticity and toughness are affected by the temperature.

The experimental study of the material mechanical behaviour is based on the experiments, thus the test methods are reviewed briefly. According to the loading direction, the tests are categorized as: tensile test (direct, indirect, confined, unconfined), compression test (confined, unconfined), shear test, splitting test, torsion test and bending test. According to the load period, the tests are categorized by monotonic test and cyclic (fatigue) test. Based on the loading rate, the monotonic tests are categorized as static and dynamic tests. There are some other test methods for special studies such as the impulse test, shock test, scratch test, creep test and so on. During the test, some necessary conditions are taken into account, such as the temperature, moisture, initial damage and crack.

In this thesis, the asphalt concrete mechanical properties such as the fracture and the fatigue damage are the main research objectives. Thus they are introduced as follows.

2.3.1 Fracture behaviour

The material failure occurs when the load is large enough so that the material (nominal) strength is reached. The material fracture behaviour including the initiation and propagation has been studied widely by researchers. It has turned out different materials (metal, engineering plastics, ceramic or ceramic composite, concrete and rock) present strongly different fracture behaviours. Normally, the study of fracture behaviour on the (quasi-)brittle material assumes that an artificial macro crack already exists in the material. For the brittle and quasi-brittle materials, the stress concentrations exist at the crack tips and the critical strengths (also called nominal strength) exist, above which the cracks begin to propagate. It has been widely demonstrated that the determination of nominal strength is highly dependent on the crack length, which will be reviewed in detail in the Section 2.4. To study the fracture behaviour, the double cantilever beam (DCB) specimen (see Figure 2.2) is suitable for both mode I and II, or the mix-mode [25].

Though the DCB test is the most direct method to investigate the fracture properties, it still presents the difficulties in loading device in practice. The single-edge

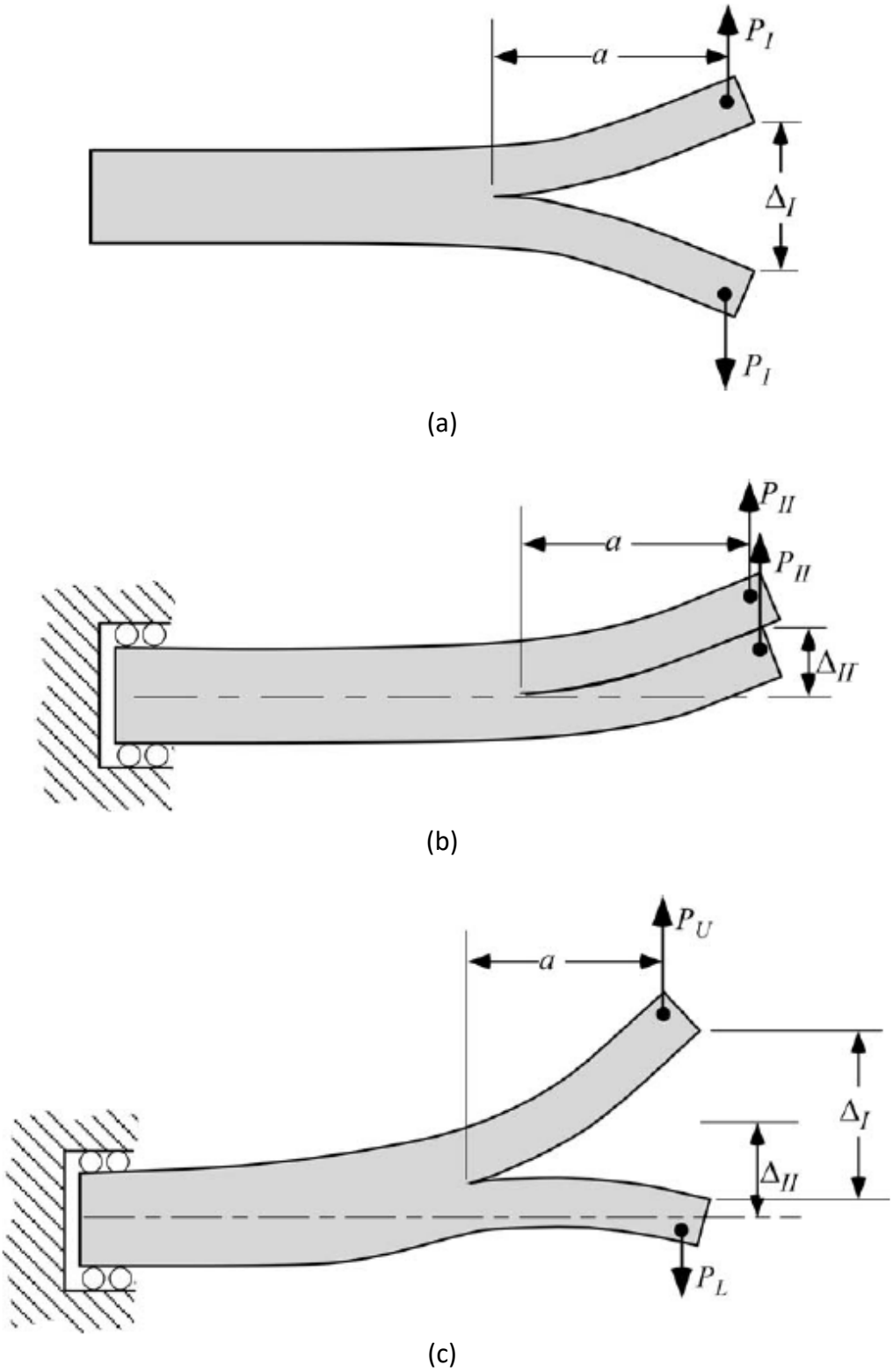

Figure 2.2: Mode I, Mode II and mix-mode loading of DCB specimens: (a) Mode I (b) Mode II and (c) Mix-mode [25]

bending test (see Figure 2.3 (a)) and the splitting test (see Figure 2.3 (b)), with the pre-notched specimen [26–28] are preferred.

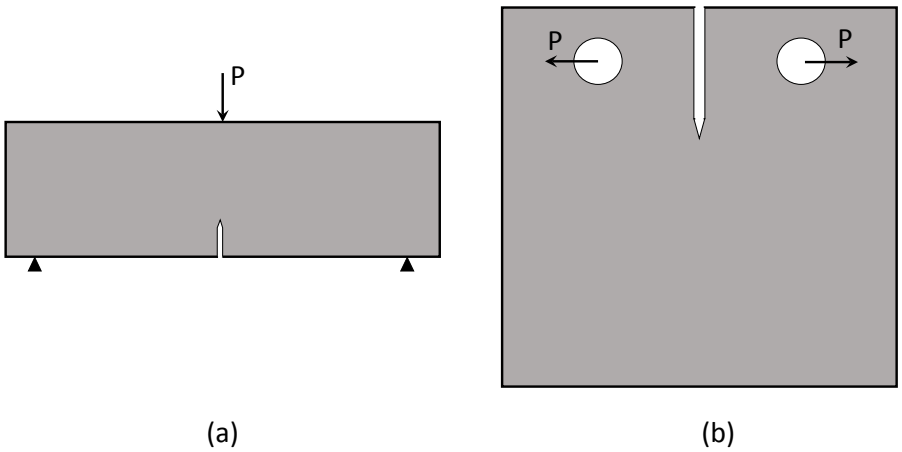

Figure 2.3: Geometry of (a) pre-notched bending test, (b) wedge-splitting test.

2.3.1.1 Wedge-splitting test of the interface between fiber glass grid and asphalt concrete

The wedge-splitting test (WST) has been widely used for the determination of fracture energy and fracture toughness on concrete-like materials, with the measurement of load and displacement. The specimen for WST can either be a cube or a cylinder [28]. WST is used especially for the study of crack of opening mode along the interface.

Tschegg [29] performed the WST with cylinder samples. The fracture behaviour of interface between asphalt overlay and interlayer with different geosynthetics reinforcement was investigated. The study indicated that good bonding between the interlayer and the asphalt layer is important for high resistance against the reflective crack propagation.

A series of WSTs were conducted by Kim and Buttlar [30–33]. The effects of specimen size, aggregate size ($9.5\,mm$ and $19\,mm$), aggregate type and environment temperature ($-10\,°C$ and $0\,°C$) on the resistance of crack propagation were studied with cylinder samples. For his result, Kim argued that a larger specimen has more significant viscoelastic behaviour. The larger aggregate size leaded to slightly smaller peak load and more compliance for the softening curves. The higher temperature leaded to larger fracture energy and smaller peak load.

In order to study the crack propagation behaviour of asphalt concrete, the experiments were performed on the (non-)reinforced AC specimens, in which the interface existed between two AC layers for both reinforced and non-reinforced AC [22,34]. For her results, the reinforced specimen, regardless of their fiber grid type, leaded to about 30% reduction of the peak load. The fracture energy was also reduced due to the application of the fiber grid.

2.3.2 Fatigue behaviour

Repeated load induces an apparent stiffness degradation of the material related to complex physical phenomena such as self-heating, thixotropy (which are reversible) and damage (not reversible) [35,36]. Related to the latter phenomenon, the propagation of defects may lead to the coalescence of cracks and the consequent failure of the structure. In the present thesis, all this processes are simply referred as fatigue damage due to the relative simplicity of its mathematical description. The fatigue failure criterion is different from the static and quasi-static strength since:
1) Enough load cycles are required before fatigue crack initializes and during the fatigue crack propagation.
2) The static strength is not reached during the repeated load.

Generally, the material fatigue is initialized because of the evolution of existing micro cracks and the generation of new micro cracks. With cumulated effort of the cyclic load, the cracks become larger and coalesce, and finally the material breaks or fails. Fatigue life is of great importance for the structure design, which can be defined as the number of load cycles before the fatigue failure. Based on the traditional fatigue failure criterion, fatigue failure is defined as the point at which the material modulus reduces to 50% of its initial value, since for most materials, the rapid damage of materials begins at around this value and the materials present bad performance of load resistance [37], while other researchers argued that the phase angle should be chosen to determine the fatigue life in fatigue test [38,39]. The fatigue life was also characterised by the yield point at Weibull plot [40].

2.3.2.1 Fatigue behaviour for asphalt concrete

Asphalt concrete is located on the first layer of the road, and suffers the distresses such as the traffic loads and climatological events during its service life [41,42]. The fatigue behaviour in asphalt concrete were widely studied in recent years.

In Moreno-Navarro's study [35], the global process involves three main phenomena: 1)accumulation of permanent deformations; 2) reversible degradation and initiation of irreversible damage (micro cracks); 3) crack propagation (the coalescence of micro cracks produces the localization and propagation of macro cracks). The results obtained in a typical cyclic loading test can be divided into three stages, as described in Figure 2.4 . Moreno-Navarro argued that the initial sharp decrease is ascribed to the permanent deformation, and this permanent deformation has an effect on the material viscoelastic properties (i.e. strain hardening phenomenon, material becomes more rigid and elastic.), resulting in the sharp decrease in fatigue process, which has also been verified by [43, 44]. Part of the stiffness loss is revisable, considering the presence of a thixotropic process in the asphalt co-existing during the damage process.

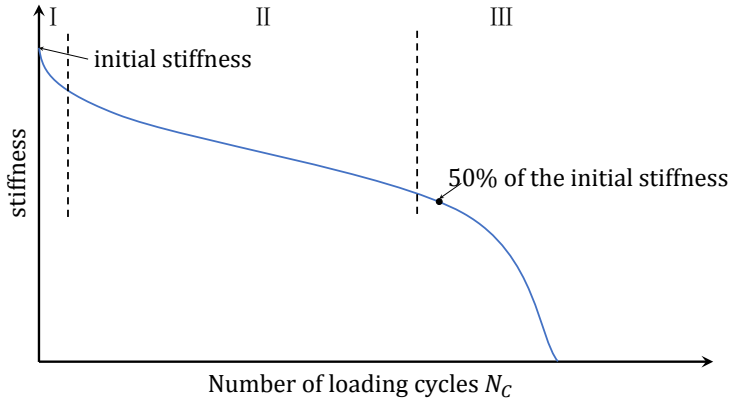

Figure 2.4: Typical evolution of stiffness during fatigue test.(Modified from [45])

2.3.2.2 Effect of the fiber glass grid in fatigue behaviour

The AC pavement is directly exposed to the traffic load, which is the typical cyclic bending load. The bending test is very popular to study the fatigue especially for the simplification of the cyclic traffic load.

Lee [19] performed the 3PB uni-directional fatigue tests shown in Figure 2.5a. The flexural strain was measured, and results showed that about $5 \sim 7$ times of fatigue life increment was obtained (See Figure 2.5 (b)). However, the stress controlled load leads to uncontrolled dramatic crack propagation in the last phase of the fatigue damage.

In Arsenie's thesis [16], the strain-controlled 4PB fatigue tests were performed (See Figure 2.6 (a)), and the bending force (F_v) is measured. The stiffness degra-

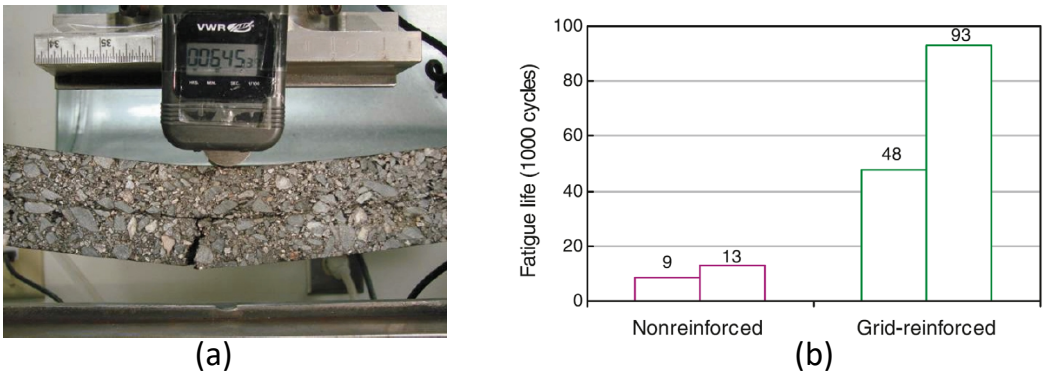

Figure 2.5: (a) Stress controlled 3-point bending cyclic test, (b) The fatigue life increment from Lee [19].

dation is obtained by the replacement of F/F_{v0} (See Figure 2.6 (b)). The study also presented an increment of about $1.5 \sim 1.8$ times on the fatigue life.

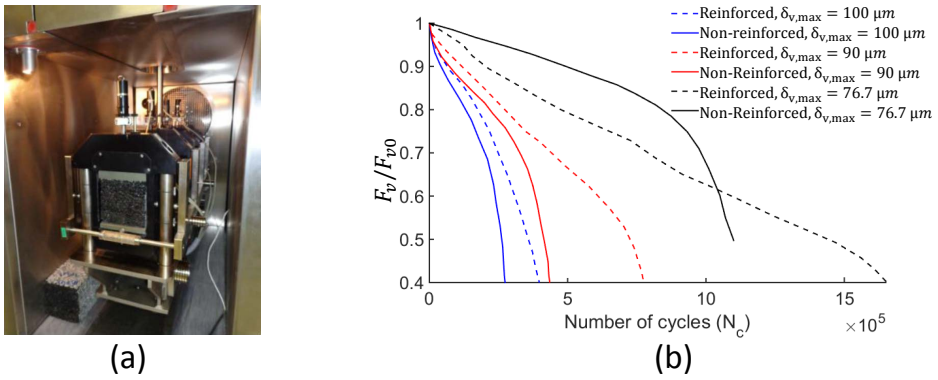

Figure 2.6: (a)Geometry of 4-point bending fatigue test, (b) the strain controlled sinusoidal loading, (c) the stiffness and fatigue life by Arsenie [16].

2.4 Material theoretical modelling

2.4.1 Material stiffness and strength

In the following sections, the material stress and strain distribution will be discussed in 3 different cases as follows:

1)For the homogeneous (quasi-)brittle material under homogeneous monotonic load, the stress is proportional to the deformation or strain, described by the elastic modulus. In this case, The breakage occurs as soon as the material strength

is reached. This material failure criteria is called strength criterion.

2)However, as the crack exists in the material, the material failure criteria transfers from strength criteria to LEFM [45], due to the stress singularity at the crack tip, in which case the stress and strain will be discussed in Section 2.4.2.

3)Another case is the material stress and strain under the fatigue model. The local strain softening occurs under low and cyclic load, which will be discussed in Section 2.7.

2.4.2 Linear elastic fracture mechanics (LEFM)

In 1920, Griffith [46] studied crack propagation problem from the point of view of energy, and he explained that the crack propagation is attributed to the energy that overcomes the material resistance. Griffith's original concept of fracture was based on the energy released during crack extension. This method was further developed by Irwin [47]. For linear elastic materials, the energy and the stress field approaches can be considered equivalent.

In energy balance criterion, the critical stress σ_c is given as follows:

$$\sigma_c = \sqrt{\frac{2E\gamma}{\pi a}} \tag{2.1}$$

where E is elastic modulus, γ is the surface energy (energy per unit area), a is half length of the crack. When the stress is larger than σ_c, the crack instability propagation is assumed to occur.

In 1947, Irwin [47] proposed a stress intensity factor K to quantitatively describe the crack tip stress field. He also found the relation between stress intensity factor and energy balance criterion, which established the foundation of fracture mechanics.

In the following part of this section, for better understanding, the near-tip crack stress field is firstly introduced and then the energy release rate.

2.4.2.1 The crack mode and elastic stress field

Among various mathematical methods in plane elasticity, the Westergaard function method [48, 49] is more convenient than the other methods to describe the basic crack problems, which is used to find the elasticity solutions for an infinite

plane with a center crack under uniform tension (mode I), in-plane shear (mode II), and anti-plane shear loading (mode III), respectively. The Westergaard solutions are given below for each of the three modes in relation to the coordinate system shown in Figure 2.7. The origins of the polar coordinate system (r, θ) and rectangular coordinate system (X, Y) are located at the crack tip, K terms are the stress intensity factor for each mode, E is the Young's modulus, ν is Poisson ratio, shear modulus $\mu = E/[2(1+\nu)]$, $\kappa = 3 - 4\nu$ for plane strain and $\kappa = (3-\nu)/(1+\nu)$ for plane stress.

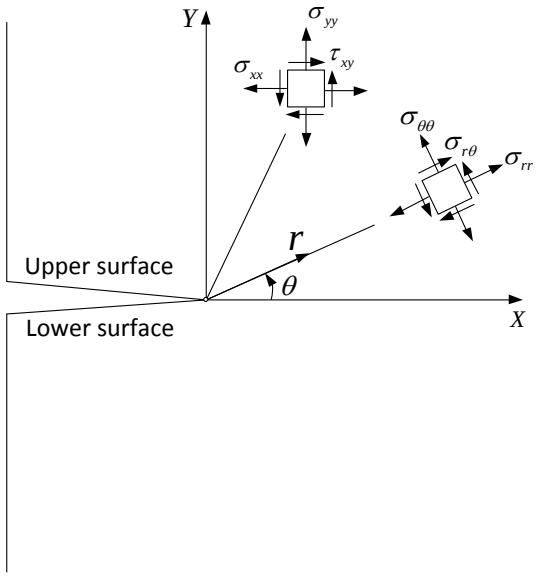

Figure 2.7: The rectangular and polar coordinate components of stress field around the crack tip (Modified from [50]).

Opening Mode, I : The two crack surfaces are pulled apart in the Y direction, that is, they move away symmetrically with respect to the undeformed crack plane (xz-plane). For the pure Mode I, the stress far from the crack tip can be described in polar coordinate in Figure 2.8.

The stress and displacement fields given by Westergaard Function Method in polar coordinate system are given by:

$$\sigma_{rr} = \frac{K_I}{\sqrt{2\pi r}} \cos\frac{\theta}{2}\left(1 + \sin^2\frac{\theta}{2}\right) \tag{2.2}$$

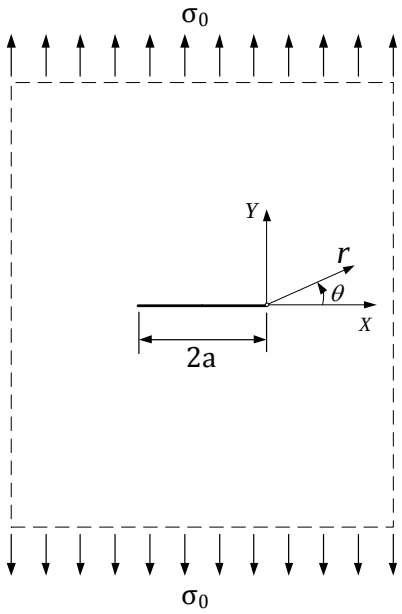

Figure 2.8: A center cracked infinite plate subjected to mode I loading (uniform tension). (Modified from [49])

$$\sigma_{\theta\theta} = \frac{K_I}{\sqrt{2\pi r}} \cos\frac{\theta}{2}\left(1 - \sin^2\frac{\theta}{2}\right) \tag{2.3}$$

$$\sigma_{r\theta} = \frac{K_I}{\sqrt{2\pi r}} \sin\frac{\theta}{2}\cos^2\frac{\theta}{2} \tag{2.4}$$

$$u_r = \frac{K_I}{8\mu\pi}\sqrt{2\pi r}\left[(2\kappa - 1)\cos\frac{\theta}{2} - \cos\frac{3\theta}{2}\right] \tag{2.5}$$

$$u_\theta = \frac{K_I}{8\mu\pi}\sqrt{2\pi r}\left[-(2\kappa + 1)\sin\frac{\theta}{2} + \sin\frac{3\theta}{2}\right] \tag{2.6}$$

Based on the Equation 2.2, the stress distribution at the crack tip is presented in Figure 2.9. The stress will be infinite (stress singularity) when it approaches the crack tip, which means that the strength criteria for the homogeneous material doesn't apply when crack exists. Thus the critical stress intensity (also called fracture toughness) is proposed as the crack propagation and the material failure criterion. Herein, the critical stress intensity factor under maximum stress with crack length $2a$ is expressed by Equation 2.7.

$$K_{IC} = \sigma_{max}\sqrt{\pi a} \tag{2.7}$$

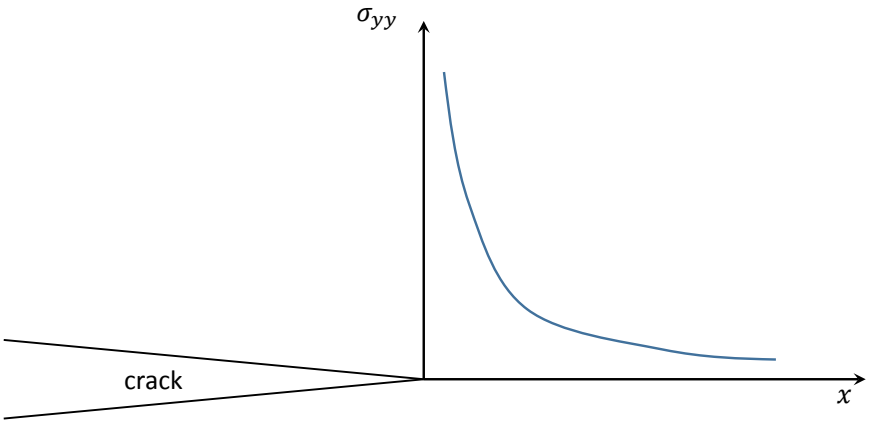

Figure 2.9: The stress distribution at the crack tip.

Shearing Mode, II : The two crack surfaces slide over each other in the x-direction, that is, they slide against each other along directions perpendicular to the crack front but in the same undeformed plane. For the pure Mode II, the stress near the crack tip can be described in polar coordinate in Figure 2.10.

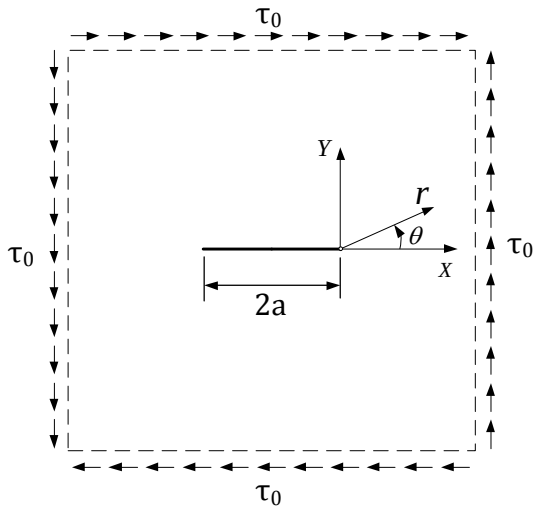

Figure 2.10: A center cracked infinite plate subjected to mode II loading (in-plane shear). (Modified from [49])

The stress and displacement fields given by Westergaard Function Method in polar coordinate system are given by:

$$\sigma_{rr} = \frac{K_{II}}{\sqrt{2\pi r}} \sin\frac{\theta}{2}\left(1 - 3\sin^2\frac{\theta}{2}\right) \tag{2.8}$$

$$\sigma_{\theta\theta} = \frac{K_{II}}{\sqrt{2\pi r}} \sin\frac{\theta}{2}\left(3\sin^2\frac{\theta}{2} - 1\right) \tag{2.9}$$

$$\sigma_{r\theta} = \frac{K_{II}}{\sqrt{2\pi r}} \cos\frac{\theta}{2}\left(1 - 3\sin^2\frac{\theta}{2}\right) \tag{2.10}$$

$$u_r = \frac{K_{II}}{8\mu\pi}\sqrt{2\pi r}\left[-(2\kappa - 1)\sin\frac{\theta}{2} + 3\sin\frac{3\theta}{2}\right] \tag{2.11}$$

$$u_\theta = \frac{K_{II}}{8\mu\pi}\sqrt{2\pi r}\left[-(2\kappa + 1)\cos\frac{\theta}{2} + 3\cos\frac{3\theta}{2}\right] \tag{2.12}$$

Tearing Mode, III : The crack surfaces slide over each other in the z-direction, that is, they tear over each other in the directions parallel to the crack front but in the same undeformed plane. Mode III is a tearing mode (see Figure 2.11).

The stress and displacement fields given be Westergaard Function Method in polar coordinate system are given by:

$$\sigma_{rz} = \frac{K_{III}}{\sqrt{2\pi r}} \sin\frac{\theta}{2} \tag{2.13}$$

$$\sigma_{\theta z} = \frac{K_{III}}{\sqrt{2\pi r}} \cos\frac{\theta}{2} \tag{2.14}$$

$$u_z = \frac{K_{II}}{\mu\pi}\sqrt{2\pi r}\sin\frac{\theta}{2} \tag{2.15}$$

Equation 2.2 to 2.14 present the stress and displacement fields of the three basic modes, solved by Westergaard Function Method. Any fracture mode in a cracked body may be viewed as a superposition of these basic modes.

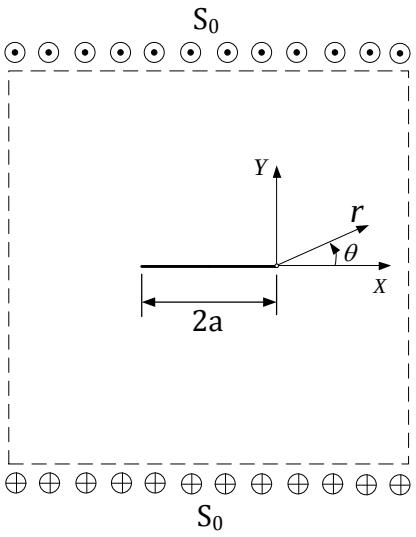

Figure 2.11: A center cracked infinite plate subjected to mode III loading (anti-plane shear). (Modified from [49])

2.4.2.2 Energy release rate

Concept of energy release rate

The stress distribution at the near-tip stress field is described above in stress field method. In the near-tip stress field method, crack growth is dominated by the local stress field around the crack tip, which is characterized by the stress intensity factor K. Fracture occurs when the stress intensity factor reaches its critical value K_c (fracture toughness). Alternatively, energy method is also a basic method of LEFM. In the energy method, the fracture behaviour of a material is characterized by the energy release rate G, which is defined as the energy dissipated during fracture per unit of newly created fracture surface area, as expressed by Equation 2.16,

$$G = -\frac{\partial(U - V)}{\partial Q}, \tag{2.16}$$

where U is the potential energy available for crack growth, V is the work associated with any external forces acting, and Q is the extended crack area for 3D problems and crack length for 2D problems.

According to Griffith's original concept [46], the work done during a crack ex-

tension must be equal to the surface energy stored in the newly created surfaces. Fracture occurs when the energy release rate reaches its critical value G_c (fracture energy, J/m^2).

Loading path independence [49]

Based on the Griffith theory for fracture of perfectly brittle elastic solids, during crack extension of da, the work done dW_e by external forces the increment of surface energy dW_s, and the increment of elastic strain energy dU must satisfy the following equation:

$$dW_s + dU = dW_e \tag{2.17}$$

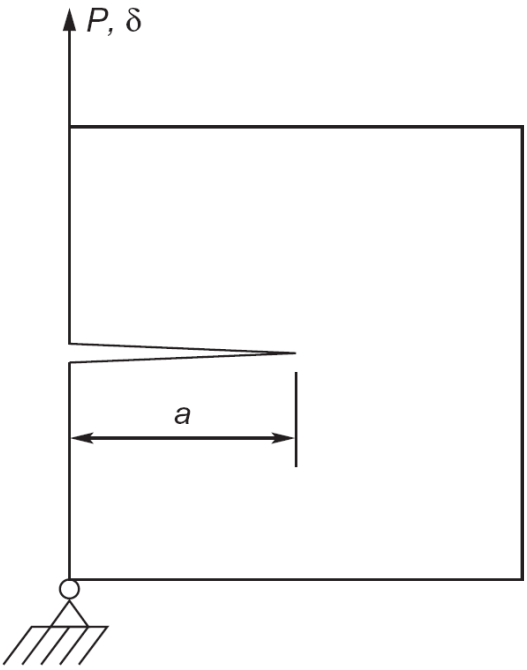

Figure 2.12: A single edge cracked specimen (Modified from [49]).

Consider a single-edge-cracked elastic specimen subjected to a tensile load P or displacement δ as shown in Figure 2.12. The relationship between the applied tensile force P and the elastic extension, or displacement, δ is

$$\delta = SP, \tag{2.18}$$

where S denotes the elastic compliance of the specimen containing the crack. The strain energy stored in this specimen is

$$U = \int_{\delta=0}^{\delta=SP} P d\delta = \int_{\delta=0}^{\delta=SP} \frac{\delta}{S} d\delta = \frac{1}{2} S P^2. \tag{2.19}$$

The compliance S is a function of the crack length. The incremental strain energy under the condition of varying a and P is

$$dU = \frac{1}{2} P^2 dS + SPdP. \tag{2.20}$$

Then two cases during the crack are discussed, respectively the fixed displacement (δ) case and fixed loading force (P) case.

Case 1, the fixed displacement:

The fixed boundary during the extension of the crack lead to $d\delta = SdP + Pds = 0$, thus we have $SdP = -PdS$. Substitution of the preceding equation in 2.20 yields

$$dU|_\delta = -\frac{1}{2} P^2 dS. \tag{2.21}$$

Furthermore, $dW_e = 0$ in this case because $d\delta = 0$ and, thus, the external load does no work. Substituting Equation 2.21 and using $dW_e = 0$, we have

$$dW_S = -dU|_\delta = \frac{1}{2} P^2 dS. \tag{2.22}$$

Thus, a decrease in strain energy U is compensated by an increase of the same amount in the surface energy. In other words, the energy consumed during crack propagation is entirely supplied by the strain energy stored in the cracked body.

Case 2, the fixed loading force:

The constant applied force P during the crack propagation leads to $dP = 0$, thus we have

$$dU|_P = \frac{1}{2} P^2 dS. \tag{2.23}$$

There is a gain in strain energy during crack propagation in this case. Moreover, we note that

$$dW_e = Pd\delta = P^2 dS. \tag{2.24}$$

Substituting Equation 2.23 and 2.24, we again obtain

$$dW_S = dU|_\delta = \frac{1}{2}P^2 dS, \tag{2.25}$$

which is half of the work done by the external force. It is interesting to note that the work done by the external force is split equally into the surface energy and an increase in strain energy. Taking case 1 and case 2 to compare, we have, FOR both boundary conditions discussed before, the energy released during crack propagation is

$$dW = dW_e - dU = \frac{1}{2}P^2 dS. \tag{2.26}$$

The corresponding energy release rate G is

$$G = \frac{dW}{da} = \frac{1}{2}P^2 \frac{dS}{da}. \tag{2.27}$$

Hence, the energy release rate is independent of the type of loading. And the released energy due to crack propagation can always be obtained by the area in Figure 2.13. Thus, the energy release rate can be calculated by

$$G = -\frac{dU}{da} = -\frac{1}{2}\frac{P_i\delta_j + P_j\delta_i}{da}. \tag{2.28}$$

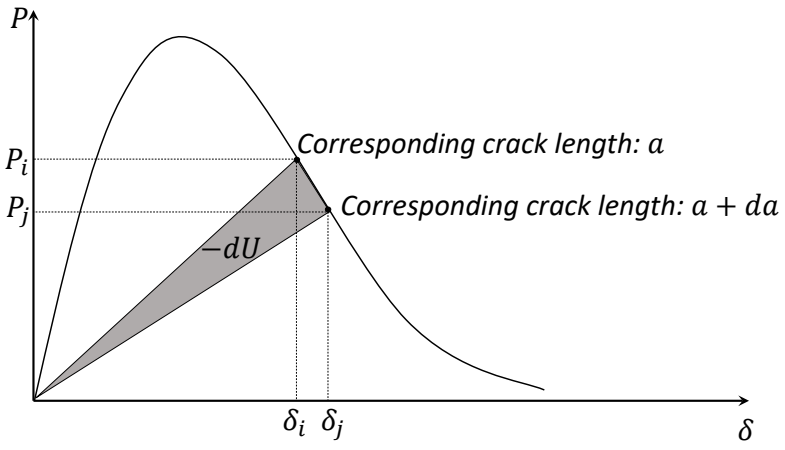

Figure 2.13: The released energy calculation by the force displacement curve.

The relation between G and K

For the linear elastic material, the energy method and the stress field method can be considered equivalent. There exists a unique relation between the energy release rate G and the stress intensity factor K. This relationship can be established by the crack closure method (CCM). CCM takes two states (i.e. crack before propagation and crack after propagation as shown in Figure 2.14) into account.

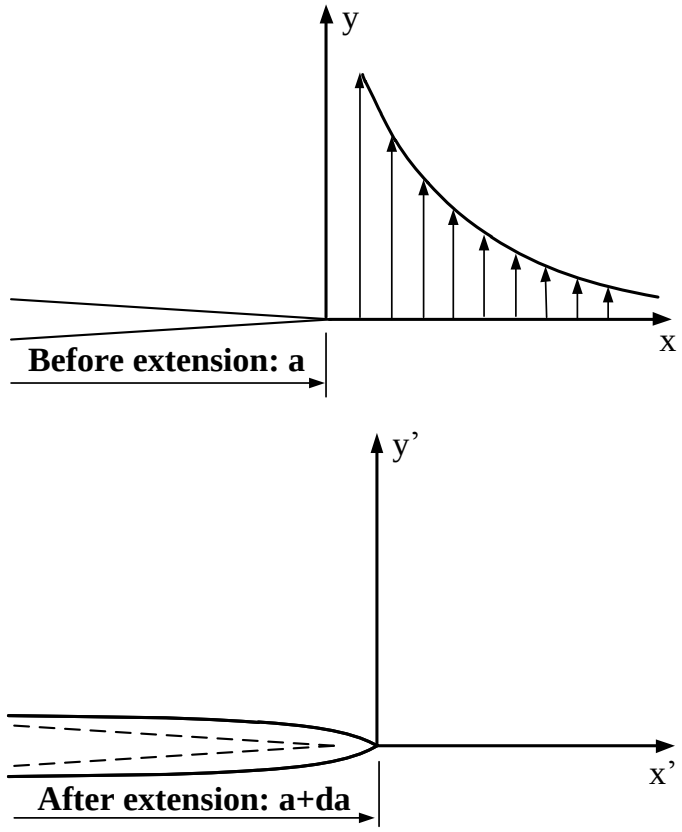

Figure 2.14: Stress distribution before extension and surface opening after extension. (Modified from [49])

The energy release rate and crack intensity factor are related by the same consumed energy during the crack propagation. The normal stress σ_{yy} ahead of the crack tip ($\theta = 0$)/ (before propagation) is

$$\sigma_{yy} = \frac{K_I(a)}{\sqrt{2\pi x}}, \tag{2.29}$$

where $K_I\,(a)$ is the stress intensity factor and the origin of the coordinate system x-y is at the crack tip.

After the assumed crack extension of da, new crack surfaces are created in $0 \leqq x \leqq da$ and the displacement of the upper face is given by [49], which can be written in x'-y' coordinates (with the origin at the grown crack tip) as

$$u_y = \frac{\kappa+1}{4\mu\pi} K_I \sqrt{2\pi(-x')} \tag{2.30}$$

For plain strain, $\kappa = 3-4\nu$, and for plain stress, $\kappa = (3-\nu)/(1+\nu)$. Noting that $x' = x - da$, we rewrite this expression as

$$u_y = \frac{\kappa+1}{4\mu\pi} K_I \sqrt{2\pi(da-x)}, \tag{2.31}$$

where $K_I = K_I(a+da)$. Because da is vanishingly small, K_I in Eq. 2.31 can be taken to be equal to $K_I(a)$.

The energy release rate can be calculated by the integration of stress and displacement at the crack tip. That is, the released energy is equal to the work done by σ_{yy} in equation 2.30 traversing u_{yy} in equation 2.31. Thus we have

$$G_I da = 2\int_0^{da} \frac{1}{2}\sigma_{yy} u_y dx, \tag{2.32}$$

where the factor 2 on the right side accounts for the two (upper and lower) crack surfaces. Substitution of Eqs. 2.30 and 2.31 into the expression 2.32 yields

$$G_I = \frac{\kappa+1}{8\mu} K_I^2. \tag{2.33}$$

For plain strain, we have

$$G_I = \frac{1-\nu}{2\mu} K_I^2 = \frac{1-\nu^2}{E} K_I^2. \tag{2.34}$$

For plain stress, we have

$$G_I = \frac{K_I^2}{2\mu(1+\nu)} = \frac{K_I^2}{E}. \tag{2.35}$$

For Mode II and Mode III problems, if the crack is assumed to grow in its original direction of the main crack, we can obtain similar relations between G and K as follows:

$$G_{II} = \frac{\kappa + 1}{8\mu} K_{II}^2, \tag{2.36}$$

$$G_{III} = \frac{1}{2\mu} K_{III}^2. \tag{2.37}$$

2.5 Fatigue crack growth - Paris' law

Paris's law relates the stress intensity factor to sub-critical crack growth under a fatigue stress regime [51]. It is the most popular fatigue crack growth model used in fracture mechanics. The basic formula reads in Equation 2.38,

$$\frac{da}{dN} = C\left(\Delta K\right)^m \tag{2.38}$$

where a is half of the fatigue crack length; N is the number of load cycles. C and m is a variable related to material fatigue behaviour, of which C is a scaler of number of load cycles N_c and it is independent on crack length $2a$ and remote stress σ; ΔK is the stress intensity factor variation in a load cycle, as shown Equation 2.39.

$$\Delta K = K_{max} - K_{min} \tag{2.39}$$

At a certain crack tip, ΔK is a function of increase of global tensile stress σ and crack length a, expressed in Equation 2.40, and $\Delta\sigma$ is the range of cyclic stress amplitude, Y is dimensionless variable related to specimen geometry [49] which equals 1 for an infinite plane.

$$\Delta K = \Delta\sigma Y\sqrt{\pi a} \tag{2.40}$$

When we substitute 2.40 into Equation 2.38 and then integrate, the remaining number of cycles N_r for the crack propagation from a_0 to a_t is derived as Equation 2.41.

$$N_r = \int_0^{N_r} dN = \int_{a_0}^{a_t} \frac{da}{\Delta\sigma Y\sqrt{\pi}} = \frac{2\left(a_t^{\frac{2-m}{2}} - a_0^{\frac{2-m}{2}}\right)}{(2-m)\,C\left(\Delta\sigma Y\sqrt{\pi}\right)^m} \tag{2.41}$$

Paris' law can be used to quantify the residual life of a specimen with a given crack size. However, the damage of asphalt concrete is generally initialized with micro cracks, followed with coalescent macro cracks, thus demanding for a special consideration when it is utilized as local fatigue model.

2.6 Fracture process zone (FPZ)

Glucklich [52] examined the fracture of concrete using fracture mechanics approach and revealed that the strain energy is converted mainly to surface energy but the surface involved is much larger than the surface of the effective crack. Later, it was found that during load, a large size of damage zone exists ahead of the macro crack [53], which is later called fracture process zone (FPZ). The FPZ has a capability to still transfer the closing stress across the micro crack faces, which consumes energy during the crack propagation. The stress in FPZ decreases with increasing deformation.

Many different techniques have been adopted to measure the shape and size of the FPZ, including optical microscopy [54], scanning electron microscopy [55,56]. high-speed photography [57], laser speckle interferometry [58], compliance and multicutting techniques [59], ultrasonic measurement [60], and acoustic emission (AE) technique [61].

To study FPZ in concrete, splitting tests were conducted by Otsuka [62], and the micro cracks were inspected by X-rays and three-dimensional Acoustic Emission (AE) techniques. In his study, the micro crack zone is defined with 2 categories namely fracture core zone (FCZ) and fracture process zone (FPZ), corresponding to 70% and 95% of the total energy of all AE events as shown in schematic map of Figure 2.15. In FCZ, more densely distributed AE events are observed, which implies more micro cracks presence in this area.

For different materials, the size and shape of FPZ can be totally different. A fine-grained silicon oxide ceramic has FPZ size of $0.1\,mm$, while it is $3\,m$ for concrete dam with extra large aggregate. The materials are categorized based on the different FPZ properties (e.g. size and stress resistance). The difference in regard of the traction separation law is shown in Figure 2.16. When FPZ is large enough to significantly influence the fracture behaviour of material, LEFM fails to describe crack growth due to the large amount of energy released in this zone.

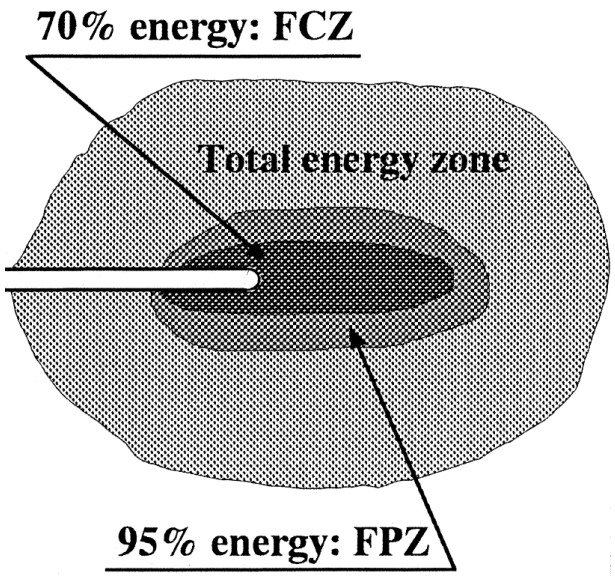

Figure 2.15: The shemetic map of FPZ by Otsuka (Modified from [62]).

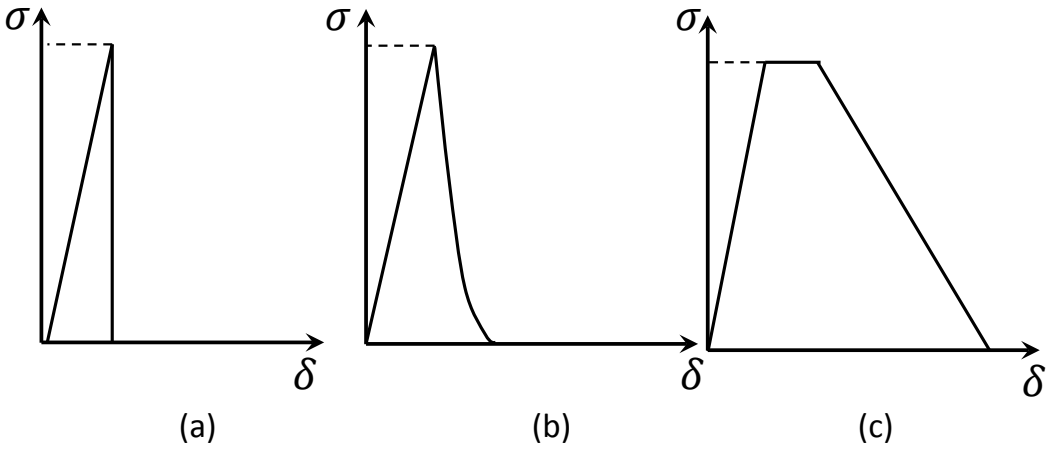

Figure 2.16: The schematic map of FPZ by Otsuka (a) brittle material, (b) quasi-brittle material, (c) ductile material (Modified from [62]).

2.7 Damage mechanics

2.7.1 Principles

Damage mechanics is concerned on the representation, or modelling, of material damage, which is intended for engineering predictions about the initiation, propagation of material fracture. The damage may be caused by any kind of load, such as thermodynamic load, mechanical load and ageing. The damage mechanics

should include both the damage initiation criterion and damage evolution model. In damage mechanics, a state factor is adopted to describe the effect of damage on the stiffness, strength or the remaining life of the material, and it possesses the similar formula:

$$A = (1 - D) \times A_o \tag{2.42}$$

where D is the damage factor, A_o is the initial stiffness or strength, A is the remaining of the corresponding variables.

For example, the stiffness of the concrete with damage is usually described as follows:

$$E = (1 - D) \times E_o \tag{2.43}$$

where E and E_o are respectively the current and original modulus of concrete.

2.7.2 Fatigue damage

Considering the duration of fatigue life, the fatigue can also be categorized into high-cycle fatigue (HCF) (also called stress fatigue) and low-cycle fatigue (LCF)(also called strain fatigue). For HCF, the load is larger than yield stress, so that the loading cycles are quite low (generally smaller than 10^4), while for LCF, the load is low, so that the strain is a control parameter to determine the fatigue level.

From the laboratory test on asphalt concrete specimen, a typical fatigue process is normally divided into 3 phases, as shown in Figure 2.4. In phase I, the stiffness undergoes a steep decline. The phase II exhibits a stable and slow decrease of the global stiffness (due to the effect of the reversible phenomena and the initiation of the fatigue damage in the form of micro cracks [35]), which takes up the longest time of fatigue life. In the phase III, sharp decline of stiffness occurs because of the damage accumulation and the propagation of the resultant macro cracks.

2.7.3 Asphalt concrete fatigue life

Fatigue in AC mixtures is defined as the phenomenon causing cracking (consisting of a crack initiation and propagation) due to the tensile strains generated in

pavements when subjected to load repetition, temperature variation, and inadequate construction practices collectively [63]. The fatigue models and fatigue life prediction are usually obtained from experiments.

Gul [64] conducted the indirect tensile fatigue test with asphalt concrete. The repeated load was applied with constant force amplitude. A non-linear model to relate fatigue life to initial strain was concluded from a series of test of different initial strain, taking into account the viscosity, the optimum bitumen content and the resilient modulus, expressed in Equation 2.44.

$$N_f = 1.367 \times 10^{-8} \times \varepsilon^{-2.556} \times \eta^{9.154} \times \nu_B^{9.154} \times E^{2.655} \tag{2.44}$$

where $N_f =$ is the number of cycles to the failure ; ε is initial strain; η is bitumen viscosity; ν_B is optimum bitumen content, percentage; E $(unit: MPa)$ is resilient modulus.

Other researches also attempted to discover the functions to relate the fatigue life to one or a set of parameters, which are presented in Table 2.1.

2.8 Numerical methods adapted to asphalt concrete modelling

2.8.1 Particularity of the asphalt concrete

Asphalt concrete is a multiphase granular material, which consists of aggregates and the asphalt binder, with a lot of micro cracks or defects in it. The AC structure induces heterogeneous stress and strain distribution in micro view meanwhile presents a globally isotropic elastic behaviour. The aggregates could interlock each other, meanwhile the asphalt binder provides strong cohesion. The failure of the asphalt concrete, no matter under monotonic or cyclic fatigue load, can always be initialized from the micro cracks and defects, followed with the coalescence of the micro cracks and result in the total breaking.

DEM is suitable for the simulation of non-continuous phenomena like the crack propagation, and the local strain softening, instead of continuum mechanics approach. It consists of particles, walls and contacts. The particle can be arranged artificially, while contacts describe interaction between particles and could be elastic or follow a defined constitutive model, and the contact can break locally with different criterion. All these features naturally promise a suitable numerical

Table 2.1: Evaluation of fatigue life in literature (Modified from [64].)

Research by	**Explanatory variables**	**Model function**
Lytton et al.	Bitumen content, stiffness, air voids, aggregate type, gradation and angularity	Linear
Harvey and Tsai	Initial stiffness and mix volumetric Intrinsically	linear
Kim et al.	Stress level	Power
Lee and Kim	Pseudo stiffness	Linear
Rodrigues	Traffic speed and the shape of the stress pulse	Quadratic
Hartman	Type of compaction	Linear
Kim et al.	Strain rates and damage growth	Linear
Kim et al.	Initial pseudo-stiffness, damage parameter fatigue failure, material parameter	Exponential
Zhou et al.	Initial stiffness	Power
Yeo et al.	Tensile strain	Power
Xiao et al.	Initial flexural strain, VFA, AV,initial dissipated energy, initial mix stiffness	Artificial neural network
Al-Rub et al.	Fundamental material properties	Finite element model
Salama and Chatti	Axle load and truck configuration	Power
Al-Khateeb and Ghuzlan	Temperature, stress, and loading frequency	Exponential
Ali et al.	Dynamic modulus and phase angle	No model was developed
Mannan et al.	Strain	Power
Underwood	Strain amplitude	Power
Luo and Qian [39]	epoxy asphalt contcrete, moisture condition	No model was developed

method for the simulation of AC, especially when the material failure is imperative. The DEM model allows up to look inside the material and understand

the fundamental interaction with the insight view underlying the complex, macro scale response, and develop a reliable, visual understanding of material behaviour with the improvements in our ability to predict the response in the asphalt concrete.

2.8.2 Cohesive zone model (CZM)

A series of numerical model describing non-linear fracture mechanics are proposed aiming at analysis of material fracture process, including the cohesive zone model (CZM) [65, 66] (also called fictitious crack model (FCM)), the crack band model (CBM) [67], two-parameter fracture model (TPFM) [68, 69], size-effect model (SEM) [70], effective crack model (ECM) [71], double-K fracture model (DKFM) [72], and double-G fracture model (DGFM) [73]. Of these numerical models, CZM, FCM and CBM have been applied for FEM, while the rest ones are modified LEFM for mathematical analysis.

CZM has become a popular tool to model fracture in quasi-brittle and plastic material. It is considered as a more realistic form of fracture mechanics to assume that the stress distribution after the crack tip instead of singular stress which results from LEFM. The cohesive zone is idealized as two cohesive surfaces after the nominal crack tip, where there is cohesive traction to hold the two cohesive surfaces together. The cohesive traction varies based on the distance between the 2 cohesive surfaces, which follows a cohesive law [62]. Hence, a physical crack extension (i.e. no load bearing capacity) occurs when the separation displacement at the tail of the cohesive zone (physical crack tip) reaches a critical value. CZM can control the rupture energy artificially, thus allowing to model a large span of materials.

2.8.2.1 Development of CZM

Cohesive zone model have been widely utilized to mitigate stress singularities in linear elastic fracture mechanics and to approximate nonlinear material separation phenomena [25, 74–78]. Towards this end, Elliott [79] introduced an interatomic attracting force per unit area to investigate fracture of a crystalline substance along a cleavage plane. Dugdale [66] and Barenblatt [65] firstly proposed cohesive models to investigate ductile and brittle material fracture behaviour, respectively.

In order to consider a relatively large nonlinear FPZ in quasi-brittle materials

such as concrete, rocks and fiber-reinforced concrete, the cohesive zone model has been employed [80–84]. The linear soften CZM was successfully extended by Hillerborg et al. [80] to study non-linear fracture processes in Portland cement concrete. Furthermore, cohesive zone models have recently been used to simulate the fracture process in a number of material systems under a variety of loading conditions.

2.8.2.2 Rupture energy control in CZM

There are many different types of cohesive laws due to different material or different research purposes. One of the key advantages offered by CZM is that it has an intrinsic fracture energy dissipation mechanism in contrast to the classical continuum based fracture mechanics for which such a mechanism is absent. Figure 2.17 depicts a cohesive zone ahead of a crack where σ is the cohesive traction and δ is the separation displacement between two cohesive surfaces.

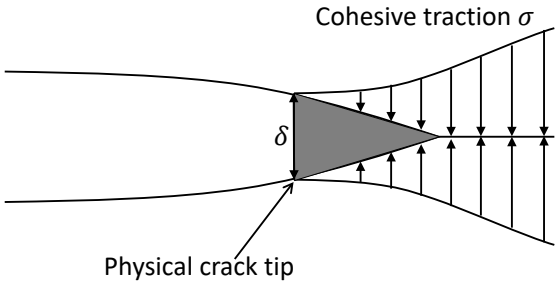

Figure 2.17: A cohesive zone ahead of crack tip (Modified from [49]).

Figure 2.18 shows a typical scheme of the bilinear cohesive law, which is characterized by linear elastic harden curve and linear soften curve. In this figure, σ_c is the peak cohesive traction, and δ_c is the characteristic displacement.

There are various traction separation laws carried out in previous researches, representing different failure mechanism operative either at the microscopic or macroscopic level, and they are used for different material mechanical behaviours at the crack tip. Generally, they share the common form of expression as shown in equation 2.45, in which σ_c is critical stress, δ_e is a characterization for the transition of the stress, and δ_c is critical strain or displacement. In some potential-based model [78], δ_e and δ_c are not given directly, and the traction is controlled by the potential instead.

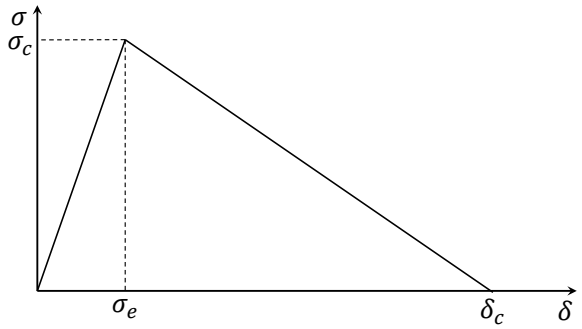

a)

Figure 2.18: A general traction separation laws for CZM.

$$\sigma = \sigma_c f(\delta, \delta_e, \delta_c) \tag{2.45}$$

Generally, the effective displacement and traction easily define various cohesive relations such as linear softening [85–87], bilinear softening [88,89], trapezoidal [90], smoothed trapezoidal [91], cubic polynomial [92], and exponential [93] functions, as shown in Figure 2.19.

2.8.2.3 CZM applied in DEM

To study the fracture behaviour of asphalt concrete, Kim and Buttlar [31–33, 94, 95] have successfully implemented CZM into discrete element method (DEM) framework. A bilinear CZM (i.e. linear elasticity, linear softening) was adopted. The specimen size dependency of asphalt concrete was captured by the developed experimental fracture test and the multiphase DEM model with CZM was able to accurately predict the size-dependent fracture behaviour when considering viscoelasticity and heterogeneity. The traction separation law is illustrated as shown in Figure 2.20. The contact strength F_{max} is calculated from two strength components (normal force F_C^n and shear force F_C^s) as well as the contact angle α,

$$F_{max} = (1 - \frac{2\alpha}{\pi}) \times F_C^n + \frac{2\alpha}{\pi} \times F_C^s \tag{2.46}$$

where α is the angle between the direction of the contact force and the line segment connecting particle centre.

The contact force between two particles is calculated by Eq. 2.47.

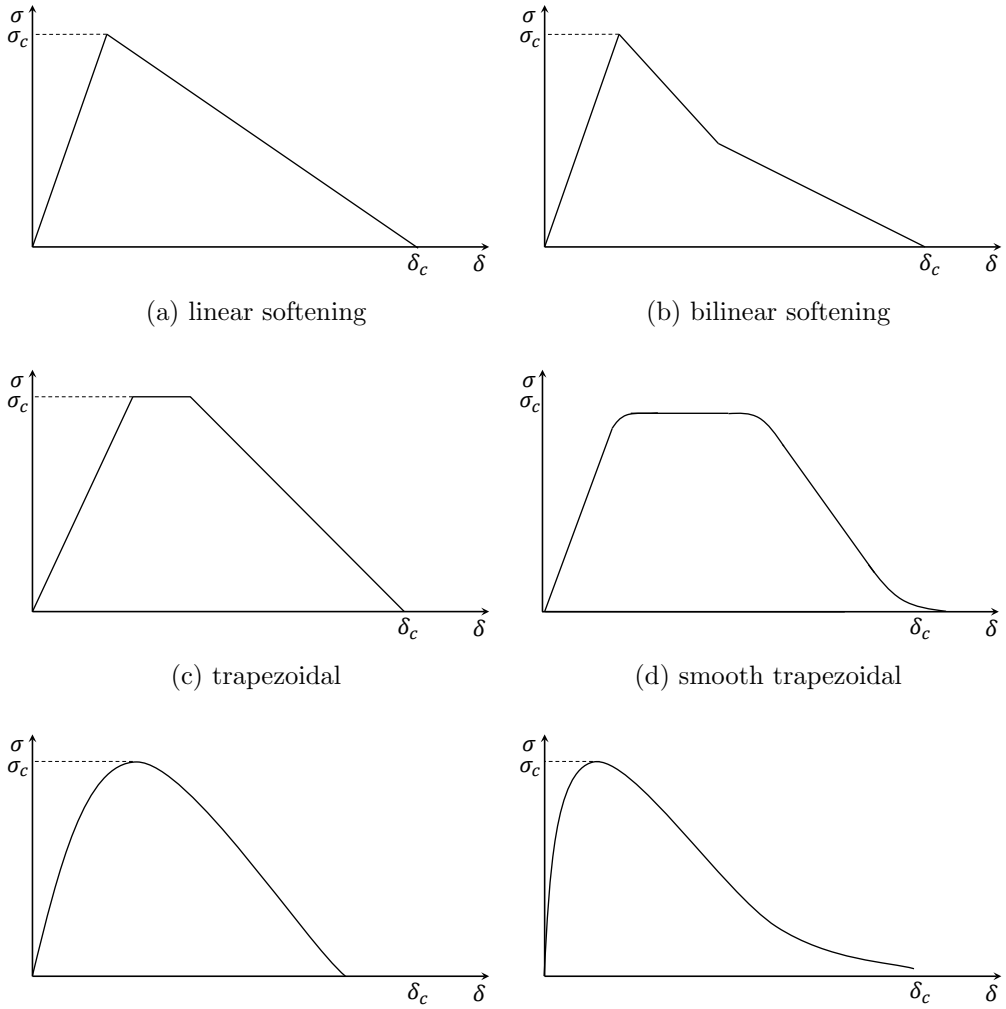

(a) linear softening

(b) bilinear softening

(c) trapezoidal

(d) smooth trapezoidal

(e) polynomial

(f) exponential

Figure 2.19: Various traction separation law. (Modified from [78])

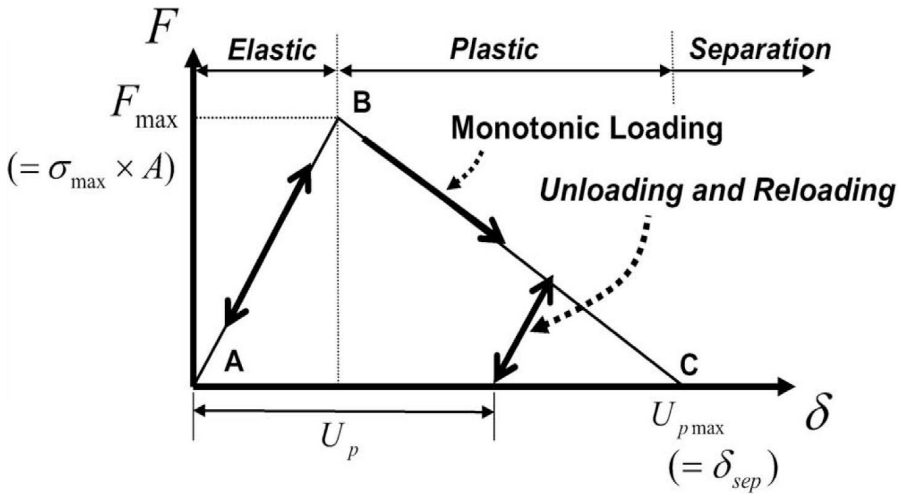

Figure 2.20: Bilinear traction separation law in DEM adopted by Kim [95].

$$F = \sqrt{(F^n)^2 + (F^s)^2} \tag{2.47}$$

When the contact force exceeds the contact strength, the contact will begin to yield or soften as shown in Figure 2.20.

$$\Delta U^k = \Delta U_e^k + \Delta U_p^k \tag{2.48}$$

The force increment ΔF^k is a function of the increment of the elastic displacement as follows:

$$\Delta F^k = K_k \Delta U_e^k \tag{2.49}$$

where

$$\Delta U_e^k = \Delta U^k - \Delta U_p^k \tag{2.50}$$

The elastic (or plastic) displacement can be determined using the consistency condition (i.e.$F - F_{max} = 0$). The contact strength is a function of the accumulated plastic deformation, as described by

$$F_C^k(U_P/U_{Pmax}) = F_C^k \left(1 - \frac{U_P}{U_{Pmax}}\right), \tag{2.51}$$

where $U_P = \Sigma(\Delta U_P)$.

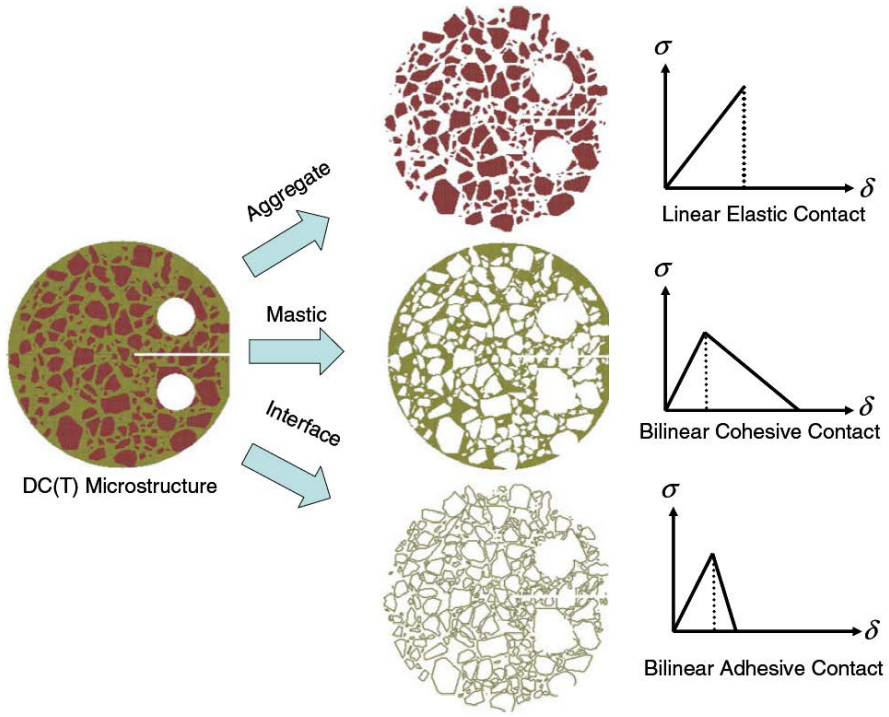

Figure 2.21: The multi-phase AC material and the constitutive models [32].

With the proposed CZM model, Kim built the multiphase DEM geometries to simulate the AC material (See Figure 2.21). The aggregate, asphalt binder, interface between aggregate and asphalt were represented differently, and a good agreement was obtained in Figure 2.22 after the parameter calibration. The existence of micro cracks demonstrated that CZM in DEM can naturally develop FPZ.

2.8.3 Fatigue damage modelling

In general, fatigue damage model is obtained using two approaches: the strain (or stress)- based models [96], and the dissipated energy method which is defined as a damage indicator of a material [64].

At the microstructural scale, fatigue damage in cemented materials is considered as a progressive process of microstructural changes with increasing the number of load cycles [42, 97, 98]. The fatigue damage model requires the appropriate characterisations of different stages of crack growth (i.e. stable crack growth and unstable crack growth) [99].

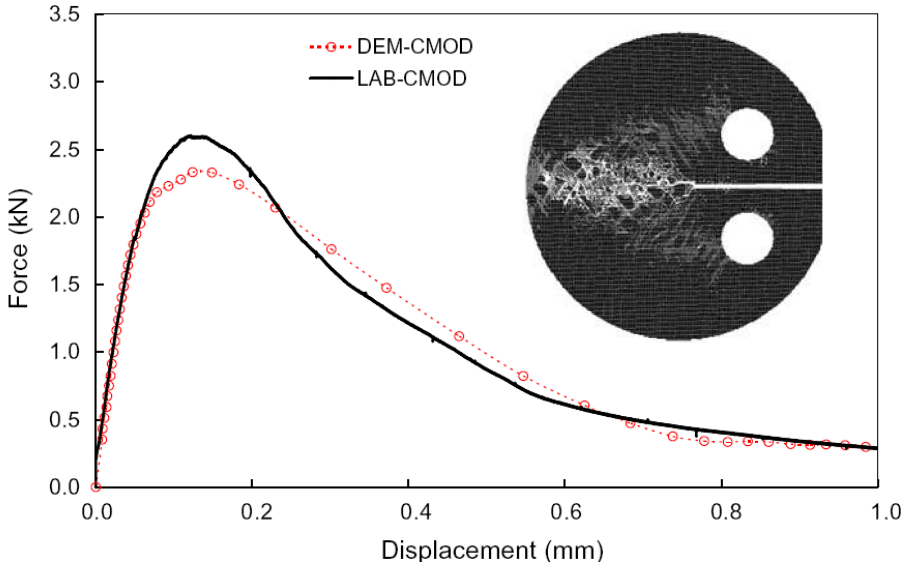

Figure 2.22: The curve of force versus displacement and FPZ (Modified from [32]).

Bodin [100] proposed a fatigue damage model for asphalt concrete based on experimental evidences for strain controlled tests which is discussed in the next sections.

2.8.3.1 Bodin's model

The damage model proposed by Bodin, describes the stiffness decrease of the material due to cyclic loading. The mathematical model utilized to describe the mechanical damage is shown in Equation 2.52, in which $G(\varepsilon, D)$ is a function of positive strain level ε and number of loading cycles N_C.

$$\Delta D = G(\varepsilon, D)\,\Delta N \tag{2.52}$$

In case of cyclic load, Equation 2.53 can well represent the rate of damage increment with the condition of the cumulation of damage evolution and the function of positive strain,

$$\dot{D} = f(D)\,\varepsilon^{\beta}\langle\,\dot{\varepsilon}\rangle \tag{2.53}$$

where $f(D)$ is function of damage and the exponent β is a material parameter related to the slope of S-N curve in the log-log diagram.

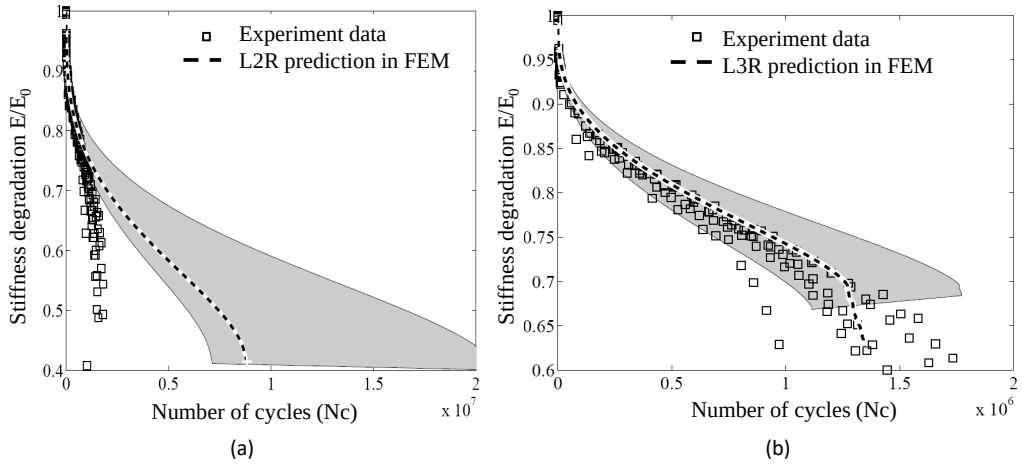

Figure 2.23: Experiment result of cantilever fatigue test and (a) fit by 'L2R', (b) fit by 'L3R' [100].

Law with 2 Regimes (L2R)

The function of damage $f(D)$ given by Paas [101] can reproduce the first two regimes in finite element method [102] shown in Figure 2.4. Bodin conducted some simulations in FEM. In Figure 2.23 (a), the prediction of numerical result didn't cover the transition from phase II to phase III.

$$f(D) = CD^{\alpha} \tag{2.54}$$

Law with 3 Regimes (L3R)

In homogeneous conditions, continuum mechanics in FEM cannot describe any loss of homogeneity of the sample, even very close to rupture. In order to reproduce the damage evolution for all the three phases, the formulation in Equation 2.55 is proposed by Bodin,

$$f(D) = \frac{\alpha_2}{\alpha_1 \alpha_3} \{\frac{D}{\alpha_2}\}^{1-\alpha_3} exp\{\frac{D}{\alpha_2}\}^{\alpha_3}, \tag{2.55}$$

with 2 additional parameters.

Figure 2.23 (b) presents the numerical prediction by 'L3R', which verified the availability in the representation of three phases of fatigue life.

Arsenie [16, 17] simulated 4PB fatigue tests of asphalt concrete beams with and without fiber glass grid reinforcement. The finite element analysis was performed

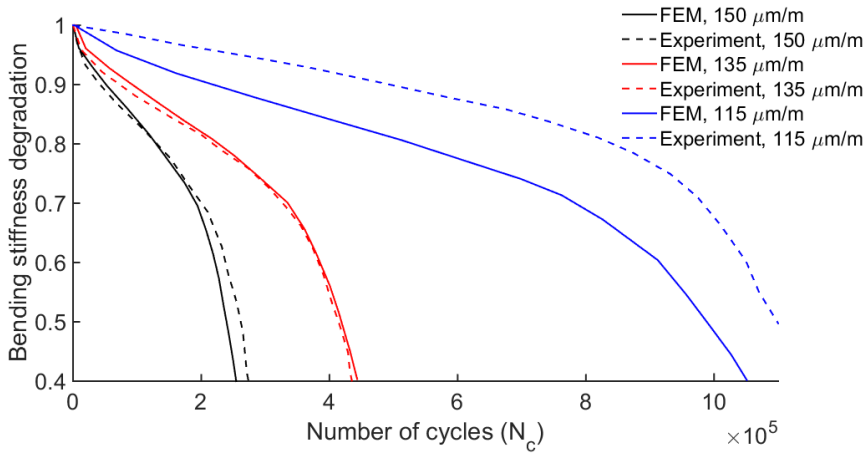

Figure 2.24: 4PB test results and fit by 'L3R' in FEM [1].

with the software CAST3M for three different strain levels (defined at the bottom and the top of the central section of the beam) $\varepsilon = 115\,\mu m$, $135\,\mu m$ and $150\,\mu m$. The stiffness degradation was well described by L3R model as shown in Figure 2.23b and 2.24, specially for the two higher values of ε.

A single set of parameters for the asphalt concrete, associated to elastic reinforcements was not directly able to fit experimental results. Then, a different strategy was adopted and the beams were divided in 2 parts: the middle layer is the composite of the AC and fiber glass grid inter-layers; the edge layers are top and bottom AC layers. The parameters of each part were attributed differently. Finally, with proper calibrations, the experimental results could be well described.

Originally based on continuum mechanics, the effect of concentration of strain and stress inducing unrealistic cumulation of damage was reduced with the addition of a non-local definition of strain. Hence a length scale was introduced, where an average of strain was calculated eliminating mesh dependence. However, this procedure made it very difficult for the realistic analysis of the effect of localized imperfections or even a reinforcement, like shown in Figure 2.25 (b). In this figure, a unrealistic discontinuity of the damage is produced by a non adapted averaging calculation near the grid reinforcement. Furthermore, the extension of the strongly damaged areas (red zones with $D = 1$) differs from the real rupture patterns, where the macro cracks result from localized degradation.

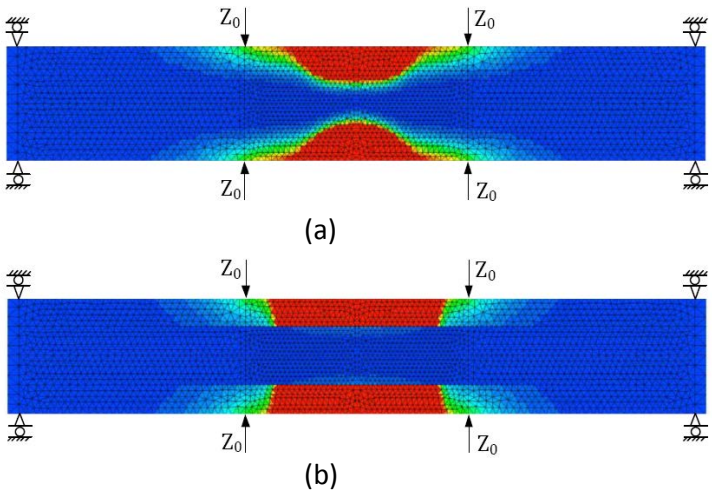

Figure 2.25: Modelling results of damage map at failure for (a) non-reinforced and (b) reinforced speicimens [1, 16, 17].

2.8.3.2 Fatigue damage modelling in DEM

Gao [45] has adapted the damage model based on Bodin's model in DEM for regular hexagonal particle structure (see Figure 2.26 (a)). The results are presented in Figure 2.27. Initial results of an exclusively local analysis (contact level) of 4PB test simulations have shown a good description of the fatigue results but were strongly affected by the sudden propagation of the crack (see Figure 2.26 and 2.27).

In order to correct the crack propagation (fatigue phase III), the damage model was coupled to a fatigue crack growth model (based on Paris law, presented in Section 2.5). The proposed solution was verified by tension/compression tests for a plate with initial central pre-cracks (Figure 2.28 (a)) and was finally consistent to theoretical solutions (Figure 2.28 (b)).

2.9 Summary of the chapter

In this literature review, the sections are organized from the material physical behaviour to the theoretical model, and finally the numerical method. The material physical behaviour is about the AC material and the fiber glass grid as well as its reinforcement effect, where the wedge-splitting test and the 4-point bending test are highlighted since they are the main tests in this thesis. It is stated that the interface between the fiber glass grid and the AC material is of great importance

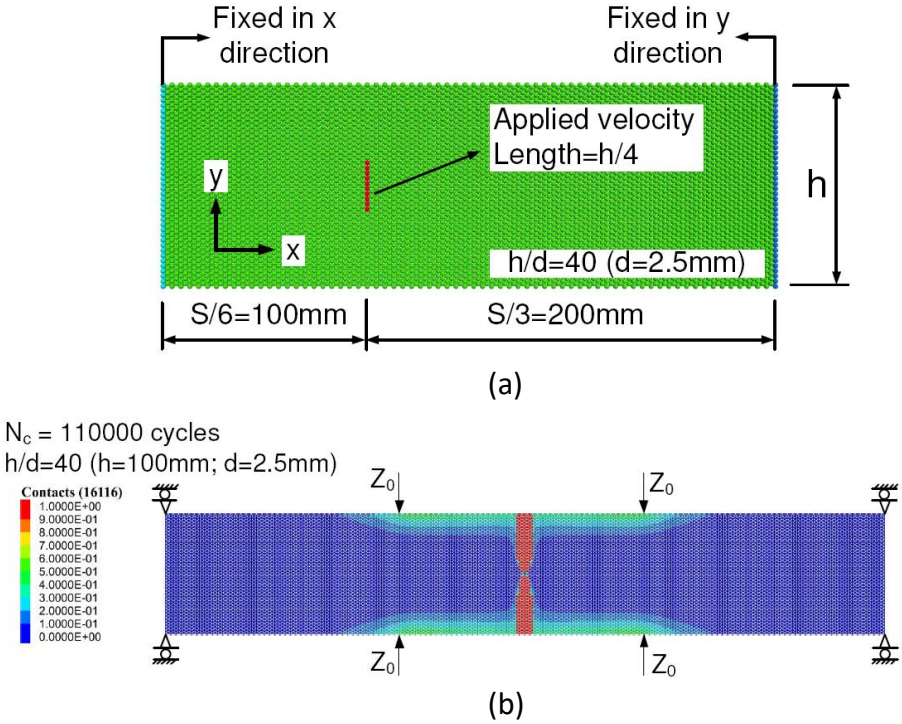

Figure 2.26: The setup of regular packing assembly in DEM and the damage map. [45]

for the effect of reinforcement, which should be paid great attention to.

Concerning the fatigue modelling, Bodin's model 'L2R' was conceived to describe only phases I and II, while 'L3R' has been proposed to describe all three phases. Instead of adopting the more complex model 'L3R', it will be demonstrated that a combination of 'L2R' as a contact law in discrete element simulations is adapted to capture the whole fatigue behaviour.

The review of the numerical method consists of the cohesive zone model, which has turned out to reproduce FPZ. The Bodin's model 'L2R' failed to describe the transition from the phase II to phase III, while the 'L3R' has been demonstrated to be available for the reproduction of three phases in material fatigue life. The reproduction of the 3 phases of the fatigue life will be attempted by the combination of 'L2R' and DEM.

It should be noted the basic knowledge on DEM will be introduced in next chapter, considering that it is intensively related to the study of the material behaviour in DEM in Chapter 3.

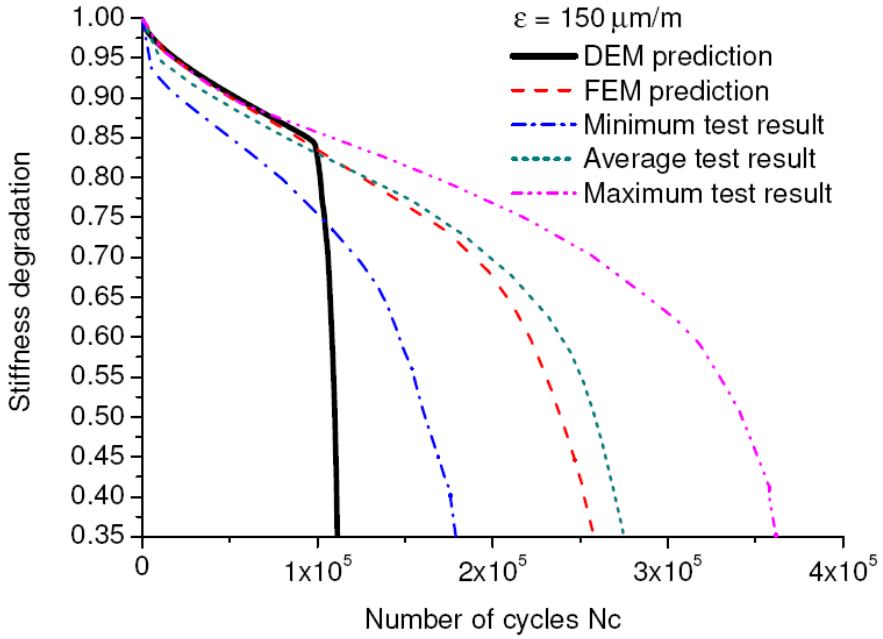

Figure 2.27: Fatigue damage curve for simulation by Gao [45], experiments FEM simulation by Arsenie [1, 16, 17].

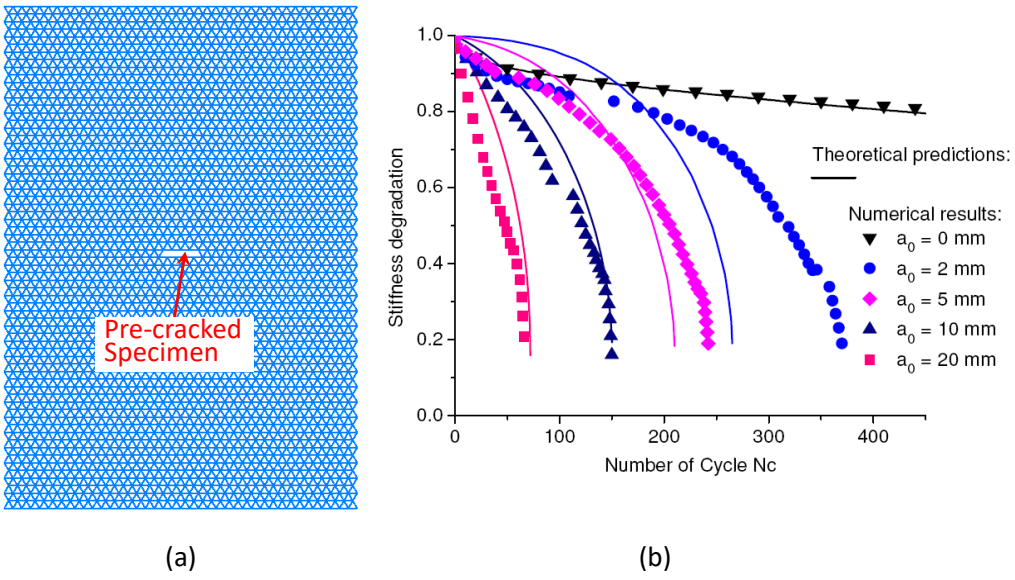

Figure 2.28: Fatigue damage curve for tensile simulation with coupled model by Gao [45].

Chapter 3

Discrete element method for 2D linear elasticity and fracture modelling

Contents

3.1 Introduction

As discussed in Chapter 2, discrete element method (DEM) presents a more realistic physical description of rupture process. In this thesis, the method proposed by Cundall [103] giving rise to the commercial software PFC (Particle Flow Code) is adopted. The materials are composed by ensembles of cemented particles interacting by direct contacts. More detailed introduction about the numerical scheme is available in Appendix A.

A brief introduction on the force displacement law and contact failure criterion in DEM is carried out in Section 3.2. The random packing assembly is utilized to model the homogeneous material, since there are some drawbacks in terms of isotropy for the regular packing model such as square and regular triangular packing assembly. In FEM, the material mechanical properties such as Young's modulus E and Poisson's ratio ν can be input directly as the properties of the mesh. However, in DEM, the micro parameters such as contact stiffness and contact strength are applied for all the contacts, so the calibration procedure is necessary to obtain the relation between contact parameters and material mechanical properties before its further application in simulating realistic materials, which is done in Section 3.4. The micro parameters of elasticity, including contact stiffness (k_n, k_s) and contact stiffness ratio k_{ratio} ($k_{ratio} = k_n/k_s$), are related to material macro mechanical properties including the Young's modulus and Poisson's ratio.

It has been revealed that the fracture toughness can be reproduced and it can be influenced by the particle size and contact strength based on LEFM as presented in Section 3.5.1. A further step is taken in this thesis by identifying the fracture toughness with the random packing assembly and the bonded-particle model (BPM), which is a built-in contact model in PFC and used for the modelling of brittle and quasi-brittle materials.

3.2 Force displacement law in DEM

In DEM, materials are regarded as assemblies of particles interacted by contacts, as shown in Figure 3.1a. The basic contact law adopted in this work is presented in Figure 3.1b. The relative motion between the particles induces the contact displacement which may be decomposed in normal and tangential components, respectively δ_n and δ_s in Figure 3.1c (with time derivatives $\dot{\delta_n}$ and $\dot{\delta_s}$). Based on the normal displacement δ_n, the normal component of the contact force is defined at each time t as

$$\vec{f_n}(t) = k_n\vec{\delta_n}(t) + c_n\dot{\vec{\delta_n}}(t), \tag{3.1}$$

where k_n is the normal stiffness and c_n is the normal viscous damping coefficient. $\vec{x}$ is the variable x in vector form.

Based on the tangential displacement δ_s, the tangential component of the contact force is defined at each time t as:

$$\begin{cases} \vec{f_s}(t) = \vec{f_s^e}(t) + c_s\dot{\vec{\delta}}_s(t), \\ \vec{f_s}^e(t) = \vec{f_s^e}(t - \Delta t) + \Delta\vec{f}_s^e(t), \\ \Delta\vec{f}_s^e(t) = k_s\Delta\vec{\delta_s}(t). \end{cases} \tag{3.2}$$

where k_s is the tangential stiffness and c_s is the tangential viscous damping coefficient. The critical damping ratio β (see Appendix A) adopted quite a small value (0.3%) due to the quasi-brittle loading pattern in this thesis. The force on each particle is the resultant force of all the contact of this particle and an extra particle damping force ($\vec{f_d}$) (see Appendix A), expressed as follows,

$$\vec{f_p} = \sum_1^n \vec{f}_{n,i} + \sum_1^n \vec{f}_{s,i} + \vec{f_d}, \tag{3.3}$$

where n is the number of active contacts around the particle and i is from 1 to n.

The particle motion is determined by $\vec{f_p}$ as follows,

$$\dot{\vec{\delta}}(t) = \dot{\vec{\delta}}(t - \Delta t) + \ddot{\vec{\delta}}\Delta t = \dot{\vec{\delta}}(t - \Delta t) + \frac{\vec{f_p}}{m}\Delta t, \tag{3.4}$$

where Δt is the magnitude of timestep (see Appendix A), m is the mass of the particle.

The global damping and viscous damping are determined from the loading condition and material physical properties (see Appendix A).

In Equation 3.1, the normal force is computed in a cumulative pattern, while the shear force is computed in an incremental pattern in Equation 3.2. In this first phase of the study, the built-in bonded contact model (BPM) is adopted for the calculations. A contact is physically represented as a *bond* associated to a bar on the normal direction which connects the center of two particles i and j (see Figure 3.1d). Its cross section is defined by the thickness of the system t and the minimum value between the radius of two particles R_i and R_j. The length $l_{ij} = R_i + R_j$ corresponds to the initial distance between the centres of the two particles i and j.

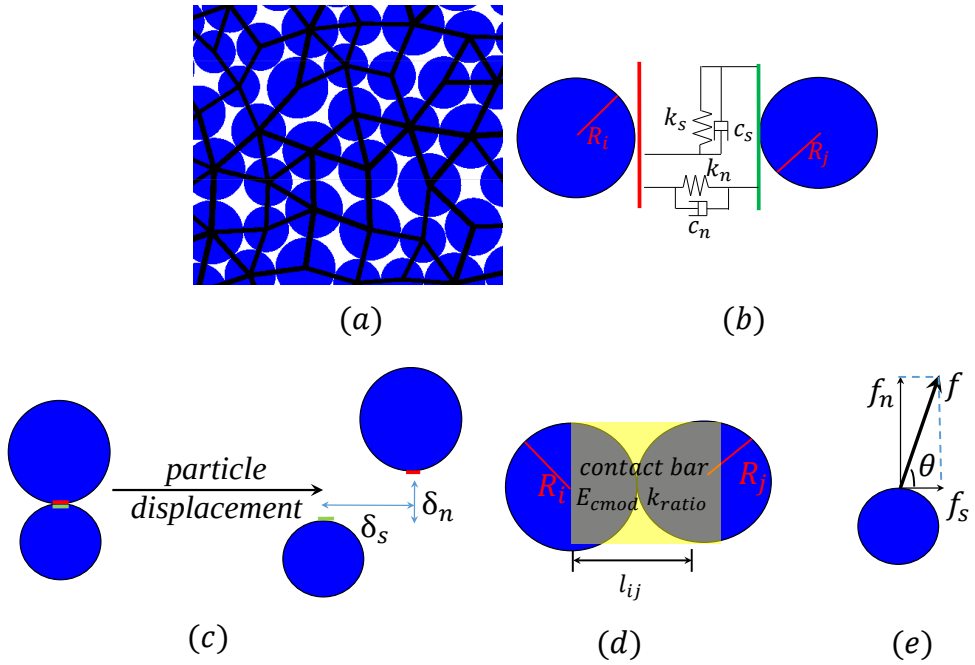

Figure 3.1: (a) Material description in DEM, (b) the contact model, (c) particle displacements, (d) its physical description and (e) corresponding forces.

The contact stiffnesses k_n and k_s are directly related to the contact elastic modulus E_{cmod} by the expressions associated to the behaviour of a bar:

$$\begin{cases} k_n = \dfrac{E_{cmod} \times t \times 2min(R_i, R_j)}{l_{ij}} = \dfrac{E_{cmod} \times t \times 2min(R_i, R_j)}{(R_i + R_j)}, \\ \\ k_s = k_n / k_{ratio}, \end{cases} \tag{3.5}$$

where k_{ratio} is the ratio between the normal and shear stiffness.

The rupture of a contact occurs when the normal or the shear force reaches its limit in tension, respectively defined as f_n^{max} and f_s^{max} as shown in Figure 3.2. For the contact strengths with unit of stress they are expressed as $\sigma_n = f_n^{max}/(2min(R_i,\ R_j))$ and $\sigma_s = f_s^{max}/(2min(R_i,\ R_j))$. After broken, the contact forces are automatically set to zero, only the elasticity in compression remains to work and the normal and shear stiffness are inherited from their values before broken.

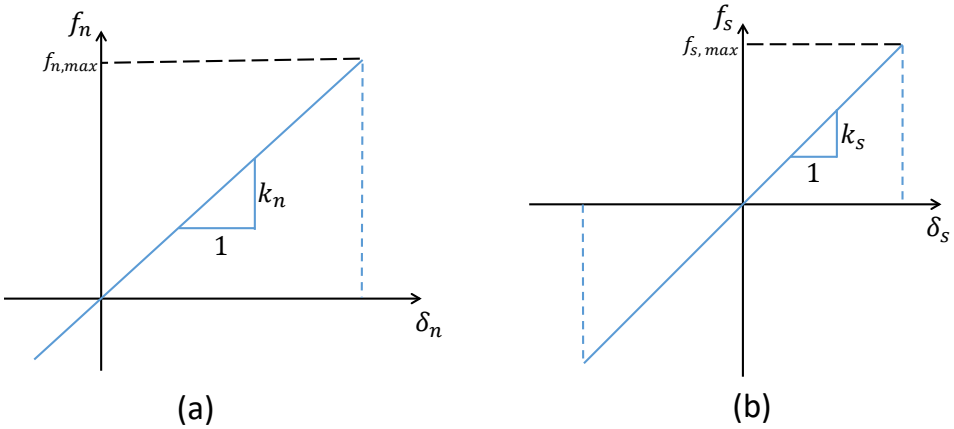

Figure 3.2: (a) Normal and (b) tangential contact forces. Definition of the tension rupture of the contact.

Finally, the micro parameters are :

- particle distribution (granularity R_i and spatial arrangement),
- model thickness t (unit $t = 1\ m$ is taken in all examples)
- contact elasticity (E_{cmod} and k_{ratio}),
- contact strength (f_n^{max} and f_s^{max}).

The definition of the particle distribution is presented in Section 3.3, the elastic behaviour is discussed in Section 3.4 and the quasi-brittle rupture is analysed in Section 3.5.

3.3 Model generation

There are many methods to generate the random packing assembly in DEM, which can be categorized into dynamic methods (e.g., boundary compaction method, particle drop method, particle size scaling method) and constructive method [104, 105]. In this chapter, the dynamic generation of model is based on the procedure adopted by Potyondy [106], which is mainly the size scaling method. The assembly is generated with three procedures, namely particle generation, internal stress control and floater elimination. During all the model generation, the particles are frictionless ($f_s = 0$, see Equation 3.2), which avoids any internal shear contact force.

3.3.1 Particle generation and internal stress control

In the first phase, a highly compacted assembly is generated within the domain of rectangular walls with relatively big overlaps between the particles [106]. Normally, when the contact model is applied, the tremendous lock-in force exists among the assembly. Addressing to this issue, a stress control procedure is imposed to reduce the stress of the initial assembly by shrinking all the particle sizes with the same factor step by step. In Potyondy's study [106], a specified isotropic stress is set as the target stress, whose value is 1% of the initial stress. The target stress is naturally dependent on the initial particle distribution and should be adapted to the contact stiffness. In order to avoid any misunderstanding, the internal stress level is expressed by the overlap ratio h_r relative to the mean particle radius $\overline{R}$,

$$h_r = \frac{\overline{\delta}_n}{\overline{R}}, \tag{3.6}$$

where $\overline{\delta}_n$ is the average overlap of all contacts of the assembly.

A scale factor for the particle shrinking X_R is then defined based on the existing overlap ratio h_r and its target h_r^T,

$$X_R = \eta \times (h_r^T - h_r) + 1, \tag{3.7}$$

where η is a hysteresis factor working on the numerical stability of the procedure. Its value is set as $\eta = 0.1$ in this work, which promises the gradual decrease of

the particle radius. If h_r is bigger than its target value h_r^T all particles may be decreased by the scale factor $X_R < 1$, otherwise, their radius may increase. The tolerance of the stress control procedure is defined as:

$$(h_r - h_r^T)/h_r^T) < 0.2. \tag{3.8}$$

After the rescaling, the system is no longer in balance. A particle natural rearrangement occurs during a stabilization phase (described in Appendix A).

3.3.2 Floater elimination procedure

Floaters are defined as the particles with less than 3 contacts. These particles are not in stable state because only normal forces exist for all contacts, and thus forming unintended voids inside the material. To eliminate these potential voids, the radius of all particles identified as floaters, are firstly enlarged until they are in contact with more than 2 particles around. Then their radius are decreased step by step until the average overlap of each floater reaches the average overlap of the assembly. During this process, the rest of the particles do not move.

3.3.3 Interactive procedure and adopted parameters

In practice, after the generation of the particles, a loop containing the Equations 3.6 and 3.7, followed by the rescaling of radius by the X_R factor is calculated until the relative error between the overlap and the target overlap becomes smaller than 20% as expressed in Equation 3.8.

In the following, all numerical samples are generated with a uniform distribution of radius between the minimum to maximum particle radius (respectively R_{min} and R_{max}). If R_{max}/R_{min} is close to 1, the assembly will be seriously crystalline arrangement [106], while if R_{max}/R_{min} is too big, the demanded number of particles forming the assembly is too large to have acceptable computational time. The size ratio is set as $R_{max}/R_{min} = 1.6$, which is in the range of the size ratio adopted by other researchers [104, 106, 107], and is available to produce isotropic macro properties.

An example of generation of a square sample with dimension $L = 40\ mm$ is presented in Figure 3.3. The difference after model generation is presented in Figure 3.3b, where a significant reduction of the contact overlap ratio has been obtained, and there is no floater in the assembly. The system presents 429 particles with

an average radius $\overline{R} = 1\,mm$ and $L = 40\overline{R}$. A target overlap ratio $h_r^T = 10^{-9}$ is adopted. One may observe the relatively homogeneous overlap distribution at the end of the process, associated to a neglectful internal stress state obtained with the generation procedure.

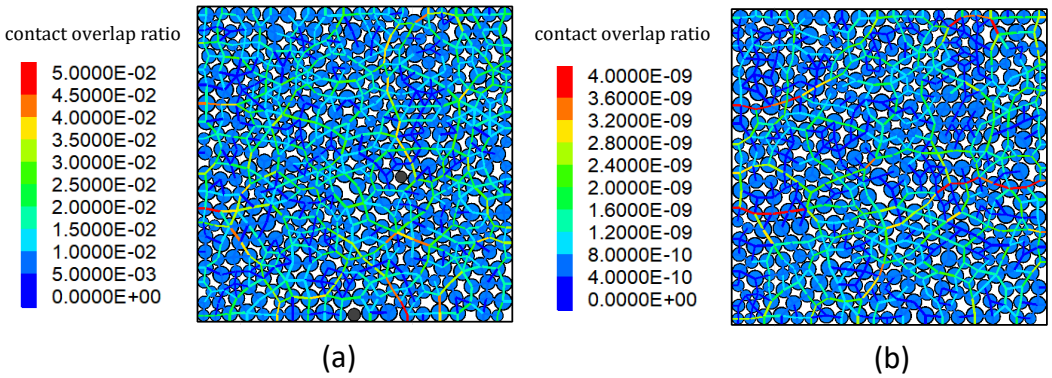

Figure 3.3: Square sample generation. (a) Initial particle distribution, $h_r \approx 1.37 \times 10^{-2}$, and 2 floater particles are indicated in black. (b) At the end of the generation process, $h_r \approx 1.04 \times 10^{-9}$, and no floaters are observed.

3.4 Elastic behaviour

In DEM, the elastic properties of the material are directly related to the geometrical properties of the particle assembly and physical properties.

As geometric properties: the particle distribution, average radius $\overline{R}$, size ratio R_{max}/R_{min} and the assembly resolution are considered here. The resolution is quantified as the ratio of a characteristic length of the specimen L to average particle diameter $2\overline{R}$ namely $\varphi = L/(2\overline{R})$ [105, 108, 109].

As shown by different authors [105–107, 109], the contact modulus E_{cmod} is directly related to the Young's Modulus of the material E, whilst the ratio between normal to tangential stiffness $k_{ratio} = k_n/k_s$ is related to the Poisson's ratio ν.

A consistent calibration is necessary for further simulations. The trends presented in the following sections are obtained by averaging 5 different samples with identical properties and different generator random seeds (see Appendix A).

3.4.1 Identification of material properties

On the following calibrations, the constrained tensile test (CTT) simulations are performed, and the geometry is presented in Figure 3.4a. Neglecteful boundary effects were observed by [105] for a resolution $\varphi = L/(2\overline{R}) > 80$ on the same conditions.

For a homogeneous and isotropic medium under uniform stress as presented in Figure 3.4b, the strains ε_{xx} and ε_{yy} and stresses σ_{xx} and σ_{yy} are related by the expressions:

$$\begin{cases} \varepsilon_{xx} = \dfrac{\sigma_{xx}}{E^*} - \dfrac{\sigma_{yy}\nu^*}{E^*}, \\ \\ \varepsilon_{yy} = \dfrac{\sigma_{yy}}{E^*} - \dfrac{\sigma_{xx}\nu^*}{E^*}, \end{cases} \tag{3.9}$$

where $E^* = E$ and $\nu^* = \nu$ in plane stress, or $E^* = E/(1-\nu^2)$ and $\nu^* = \nu/(1-\nu^2)$ in plane strain.

The lateral boundary condition (see Figure 3.4a) imposes $\varepsilon_{xx} = 0$. Hence, from Equation 3.9, the Young's Modulus E and the Poisson's ratio ν can be obtained:

$$\begin{cases} \nu^* = \dfrac{\sigma_{xx}}{\sigma_{yy}}, \\ \\ E^* = \dfrac{\sigma_{yy}}{\varepsilon_{yy}}(1-\nu^{*2}). \end{cases} \tag{3.10}$$

The value of E and ν can be easily identified from the simulation results. The vertical stress σ_{yy} is imposed, while the horizontal stress σ_{xx} is obtained by the summation of the horizontal forces at one of the lateral boundaries divided by the length L. The vertical strain is calculated based on the elongation of the sample $\varepsilon_{yy} = \Delta L/L$.

3.4.2 Effect of normal stiffness

The normal stiffness of the contacts is driven by the contact modulus E_{cmod}. In order to avoid boundary effects a resolution $\varphi = L/(2\bar{R}) = 80$ is adopted. Five square samples with a dimension $L = 320\ mm$, 6964 particles by average and presenting maximum and minimum radius, respectively, $R_{max} = 2.46\ mm$ and $R_{min} = 1.54\ mm$ are tested.

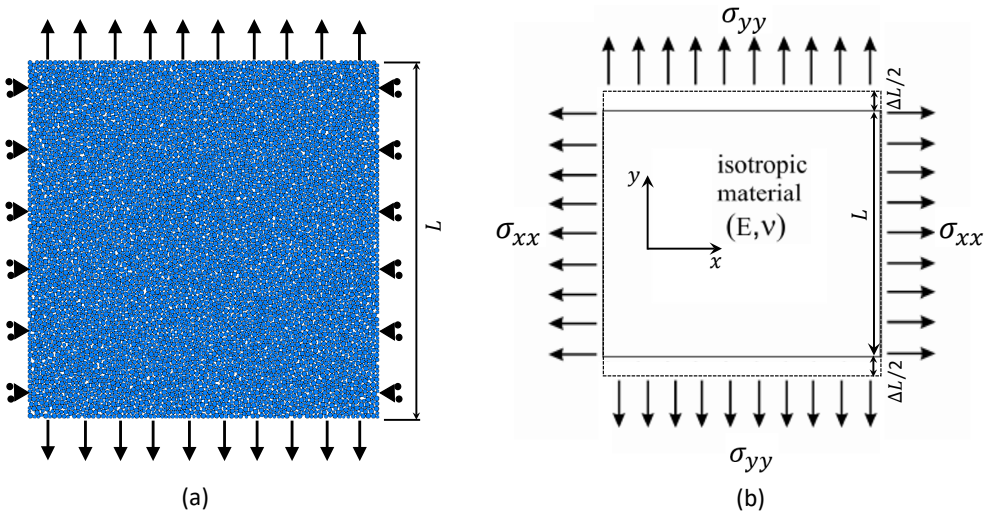

Figure 3.4: (a) Applied stress and displacement boundary conditions applied to the numerical sample. (b) Stresses in a continuum medium.

Figure 3.5 presents a linear relation between the Young's modulus of the material E and the granular contact modulus E_{cmod} (for a given $k_n/k_s = 1$). A low standard deviation of approximately 0.5% of the average results of E are observed.

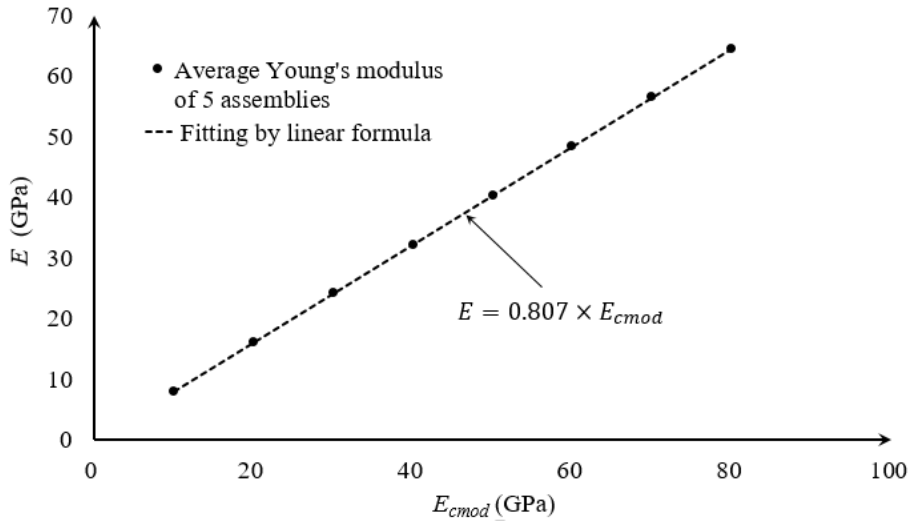

Figure 3.5: Material Young's modulus E versus contact modulus E_{cmod} for $k_n/k_s = 1$.

No effect of the contact modulus E_{cmod} is observed on the Poisson's ratio of the material ν, which is consistent with the results of other authors [105, 107].

3.4.3 Effect of stiffness ratio (k_{ratio})

The effects of k_{ratio} on the Young's modulus E and Poisson's ratio ν of the material are studied by varying the value of k_n/k_s from 1.5 to 4.5. The average of the results of the five samples are presented in Figure 3.6, where the relation between the Young's modulus E and the stiffness ratio (k_n/k_s) seems to take a logarithmic shape as presented in Figure 3.6. A low standard deviation of approximately 0.5% of the average results of E are observed.

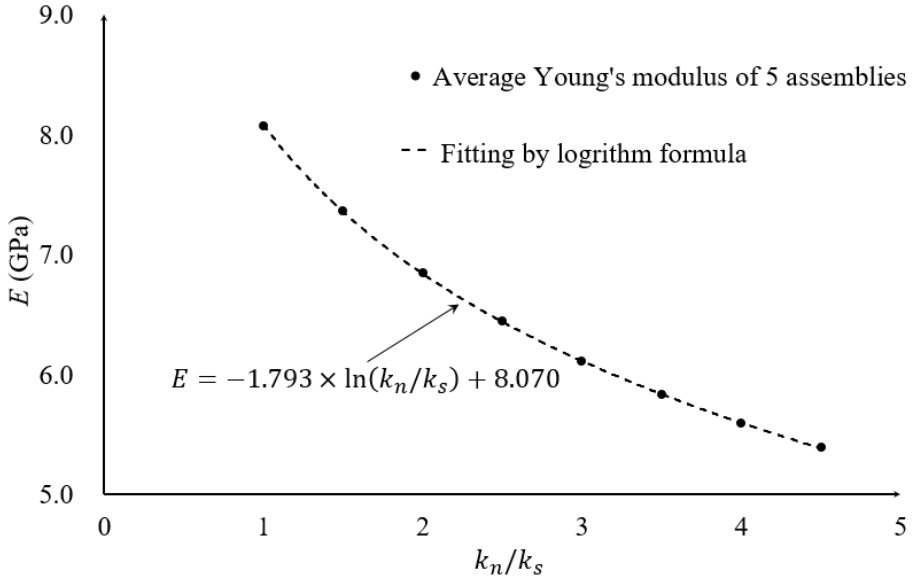

Figure 3.6: Material Young's modulus E versus contact stiffness ratio k_n/k_s for $E_{cmod} = 10\ GPa$.

In Figure 3.7, the relation between Poisson's ratio ν and stiffness ratio (k_n/k_s) can also be well fitted by the logarithm function. A low standard deviation of approximately 1% of the average results of ν are observed.

3.4.4 Calibration of elastic parameters

For a given size distribution of particles, the effects of the particle size (scale effect) are neglectable on the elastic parameters E and ν [105, 107].

Considering the results of Figure 3.7, the Poisson's ratio ν can be related to the ratio of stiffness $k_{ratio} = k_n/k_s$ by the empirical relation

$$\nu = 0.1645 \times ln\left(\frac{k_n}{k_s}\right) + 0.0913, \tag{3.11}$$

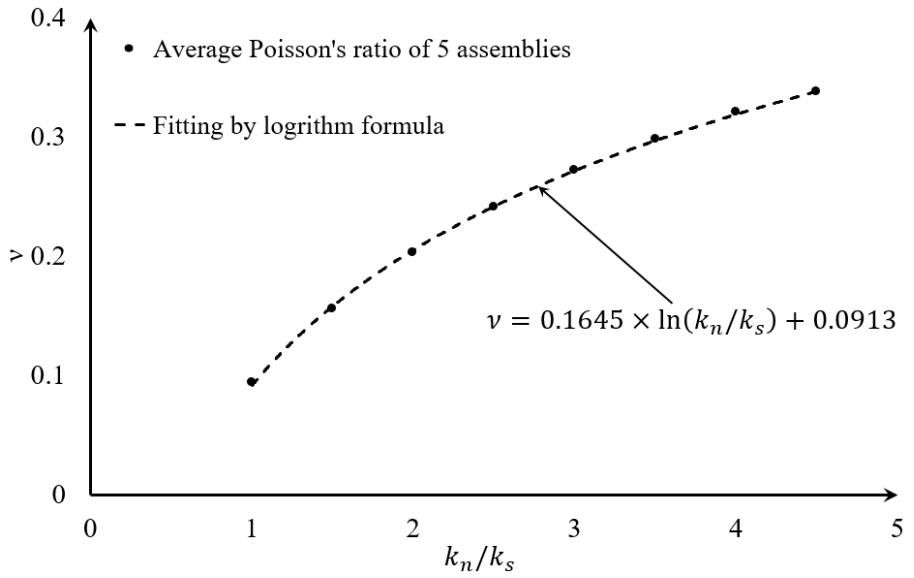

Figure 3.7: Material Poisson's ratio ν versus contact stiffness ratio k_n/k_s for $E_{cmod} = 10\ GPa$.

containing the usual range of asphalt concrete ($0.1 \leq \nu \leq 0.34$) [22].

The results of Figure 3.6 with respect to the effect of k_{ratio} on the Young's modulus of the material E for the given contact modulus $E_{cmod} = 10\ GPa$ can be generalized based on the linear dependence between E and E_{cmod} as shown in Figure 3.5. For any value of E_{cmod} and $k_{ratio} = k_n/k_s$, one can have for the Young's modulus:

$$E = \left(-0.1793 \times ln\left(\frac{k_n}{k_s}\right) + 0.807\right) E_{cmod}, \tag{3.12}$$

containing the usual range of asphalt concrete ($0.5\ GPa \leq E \leq 65\ GPa$) [1].

3.5 Quasi-brittle rupture

In linear elastic fracture mechanics (LEFM), the rupture of the material is strictly due to crack propagation. A structure without cracks may present an infinity resistence. This inconsistency is one of the limits of this theoretical approach, where the strength of the material is not taken into account. The limited strength of a material can be interprated as the effect of micro *defects* (cracks, interfaces, voids, etc.) under loading. A cracked structure composed by a real material may

naturally present different scale lengths: one is the relative size of the crack with respect to the structure dimension and, the other one, the relative size of the crack with respect to the inner defects of the material. These different length scales lead to well known scale effects in quasi-brittle rupture [110, 111].

In the following sections, these scale effects are discussed from the point of view of discrete element simulations. Some general relations are derived from the theoretical analysis of a structured assembly of particle and their consequences on the calibration of model parameters are presented.

3.5.1 Strength and toughness in structured granular packing

The rupture of a square packing in PFC was studied by [106]. A square packing assembly of particles is partly presented in Figure 3.8, where the contacts, the remote stress and the crack tip stress distribution of continuum mechanics are schematically shown.

Let us suppose the effect of a far field vertical stress Σ over this assembly of particles. In absence or distant enough of any crack, the distribution of the stress is uniform, the maximum contact force are vertically oriented and may present a value

$$f_n^{intact} = 2\Sigma R t, \tag{3.13}$$

where R is the particle radius.

Let us suppose a very big plate with a crack (of length $2a$) in the middle. Near a crack tip the theoretical prediction of the vertical stress can be obtained from Equation 2.3 with $\theta = 0$:

$$\sigma_{yy}(r) = \frac{K_I}{\sqrt{2\pi r}}, \tag{3.14}$$

where r is the distance from the crack tip and $K_I = \Sigma\sqrt{\pi a}$ is the stress intensity for this geometry [49].

The maximum contact force, at the closest contact from the crack tip, can be obtained by the integration of the stress field (Equation 3.14) over a distance of particle diameter $2R$ ($0 \leq r \leq 2R$):

$$f_n^{crack} = t\int_0^{2R} \frac{K_I}{\sqrt{2\pi r}} dr = 2K_I t\sqrt{\frac{R}{\pi}} = 2\Sigma t\sqrt{aR}, \tag{3.15}$$

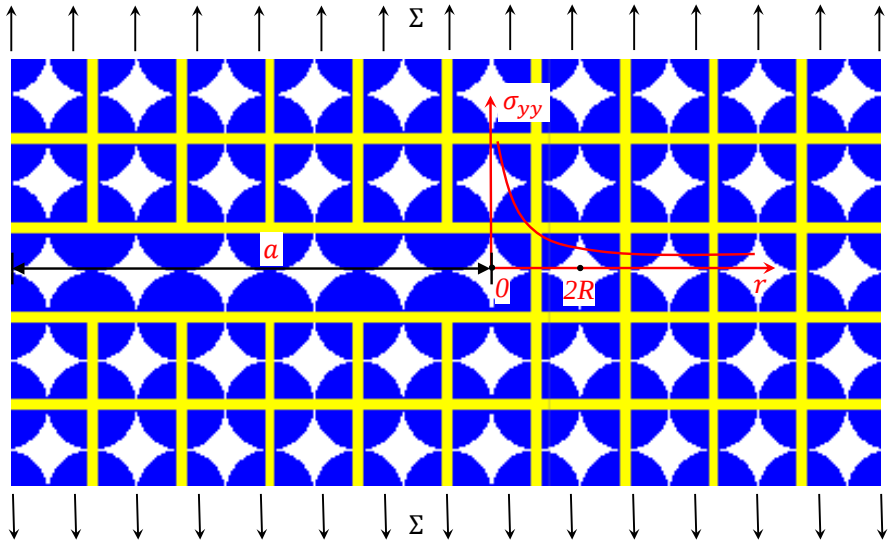

Figure 3.8: The square packing particles and the stress distribution near a crack based on continuum fracture mechanics.

where K_I is the stress intensity factor, σ_n is tensile strength for the first contact before the crack tip, and R is the particle radius. It is indicated that the fracture toughness is dependent on the particle size, so that particle size should be carefully determined in terms of the reproduction of fracture behaviour. The study also stated that, as long as the first contact reaches its strength and thus breaks immediately, the required remote stress for the next contact is smaller than that for the previous broken contact, while the actual tensile force acting on the next contact is larger based on Equation 3.15. Consequently, under the same remote stress, crack will propagate unstably.

3.5.1.1 Tensile strength in a square packing

The relation between the tensile strength of the material Σ^t and the contact strength f_n^{max} can be simply obtained from Equation 3.13. The contact force $f_n^{contact}$ for an assembly without cracks must be limited by f_n^{max}, while it automatically limits the maximum far field stress Σ by Σ^t:

$$\Sigma^t = \frac{f_n^{max}}{2Rt}. \tag{3.16}$$

3.5.1.2 Fracture toughness in a square packing

The relation between the toughness of the material K_{IC} and the contact strength f_n^{max} can be obtained from Equation 3.15. The contact force f_n^{crack} for an assembly with a crack must be limited by f_n^{max}, while it automatically limits the maximum stress intensity factor K_I by K_{IC}:

$$K_{IC} = \frac{f_n^{max}}{2t}\sqrt{\frac{\pi}{R}}. \tag{3.17}$$

3.5.2 Strength and toughness in a random packing structure

In more complex particle structures, the relations between the material properties (strength Σ^t and toughness K_{IC}) and the contact properties (normal strength f_n^{max} and tangential strength f_s^{max}) are similar to the relations presented in the previous section for a square structure [106].

For a given ratio between normal to tangential strength $S_r = f_n^{max}/f_s^{max}$, the strength of the material can be expressed by

$$\Sigma^t = \frac{f_n^{max}}{\overline{R}t} \times \alpha, \tag{3.18}$$

where α is a positive value which depends on the particle structure (i.e. $\alpha = 1/2$ and the average radius $\overline{R} = R$ for a square structure, as shown in Equation 3.16).

The toughness can be assessed by

$$K_{IC} = \frac{f_n^{max}}{t\sqrt{\overline{R}}} \times \beta, \tag{3.19}$$

where β is a positive value which depend on the particle structure (i.e. $\beta = \sqrt{\pi}/2$ for a square structure, as shown in Equation 3.17) [106].

3.5.3 Calibration of the rupture parameters

The tensile strength Σ^t and the toughness K_{IC} of the material are proportional to the contact strength f_n^{max} (for a given $S_r = f_n^{max}/f_s^{max}$), as shown by Equations 3.18 and 3.19. However, the particle dimension $\overline{R}$ affects strength Σ^t and toughness K_{IC} in a non proportional way ($K_{IC}/\Sigma^t \propto \sqrt{\overline{R}}$). It means that the

calibration of the rupture parameters of the material depends not only on rupture parameters of the contacts but also on particle average dimension.

Let us suppose the effect of a size scaling of a granular assembly (of a factor λ) where the contact strength (f_n^{max} and f_s^{max}) is kept constant (see Figure 3.9).

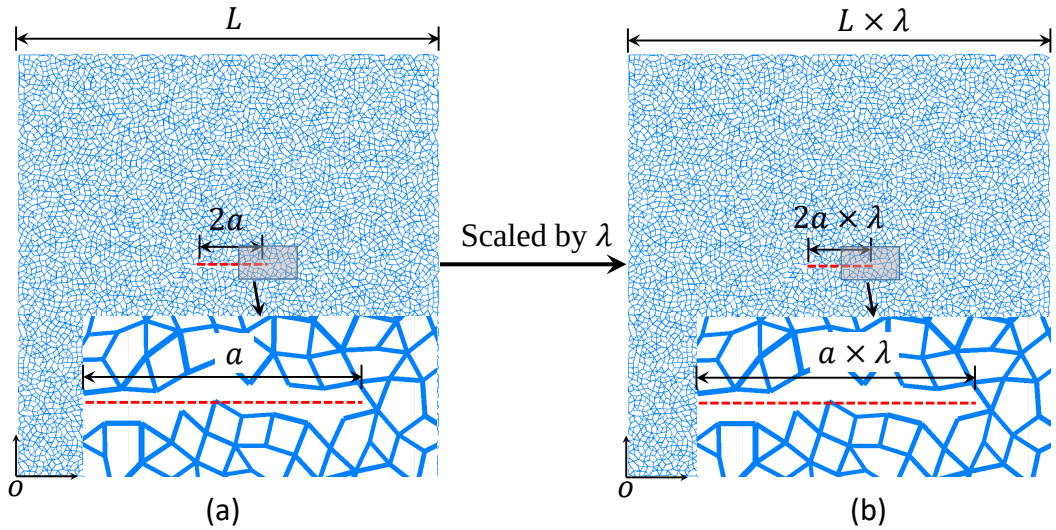

Figure 3.9: Contact forces of (a) particle assembly and (b) the same assembly scaled by a factor λ.

Taking into account the difference on the particle radius on the result of Equation 3.18, the ratio between the tensile strength of the initial assembly Σ_1^t and the scaled one Σ_2^t is $\Sigma_1^t/\Sigma_2^t = \lambda$. The same procedure applied to Equation 3.19 conducts to the ratio between the toughness of the initial assembly $K_{IC,\,1}$ and the scaled one $K_{IC,\,2}$, $K_{IC,\,1}/K_{IC,\,2} = \sqrt{\lambda}$.

Hence, technically, any different set of value of tensile strength Σ^t and toughness K_{IC} can be obtained (for a given particle distribution) with adapted values of contact strength f_n^{max} (and f_s^{max}) and particle mean radius $\overline{R}$.

3.5.3.1 Simulation of the rupture of a cracked plate

The consistency of DEM on the characterization of the quasi-brittle rupture is verified by the analysis of the behaviour of the cracked plates in tension. Tensile tests leading to sample failure in open mode (mode I) allow the identification of the parameters of the material (tensile strength Σ^t and toughness K_{IC}) associated to the contact parameters of the discrete model. A tension stress Σ is applied on the plates of width $2b = 96\ mm$ and height three times longer $3 \times 2b = 288\ mm$ (in

order to avoid boundary effects [112, 113]) with a central crack (see Figures B.1a and B.1b.). Twelve different crack lengths $0\ mm \leq 2a \leq 77\ mm$ are adopted (in detail, in Figure B.1c crack shape following the granular structure.) Five different discrete samples are used to identify the mean trends with a total of $5 \times 12 = 60$ simulations.

Bi-dimensional random packing assemblies of particles with average radius $\overline{R} = 0.6\ mm$, ratio of maximum to minimum diameter $R_{max}/R_{min} = 1.6$, which results in samples with 20800 particles in average. As contact properties: modulus $E_{cmod} = 20\ GPa$, stiffness ratio $k_{ratio} = 3.5$, and contact strength $f_n^{max} = f_s^{max} = 7.2 \times 10^3\ N$ are adopted.

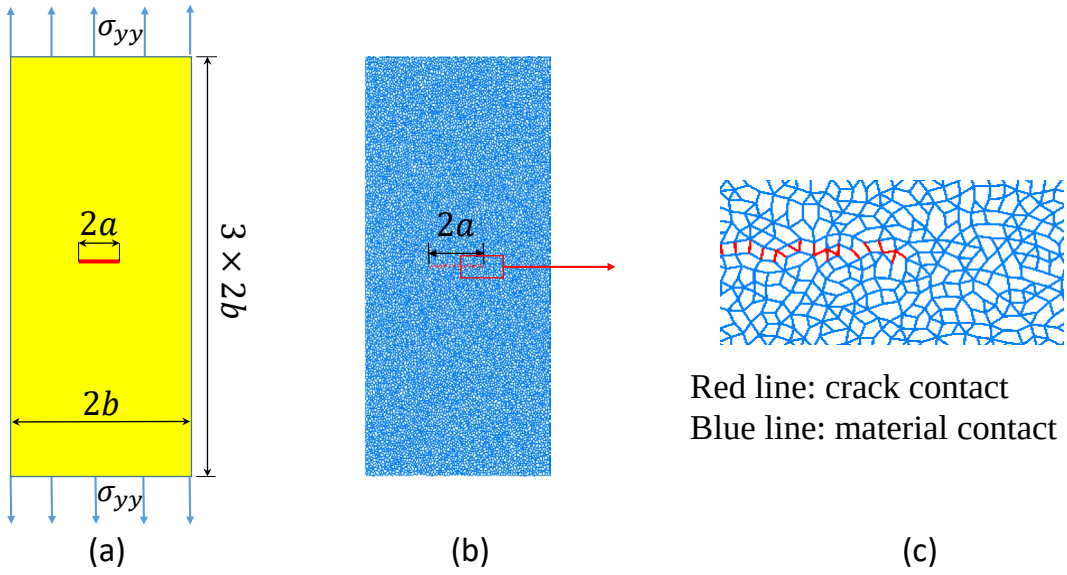

Figure 3.10: (a) Geometry of the cracked plates,(b) DEM specimen and (c) zoom on the crack tip.

The samples without cracks confirm the results of Equations 3.9, a Young's Modulus $E = 11.6\ GPa$ and a Poisson's ratio $\nu = 0.3$. The maximum value of the tensile stress Σ (before the rupture caused by the propagation of the central crack) defines as the nominal strength of the plate Σ_{max} for each simulation. The obtained values of the maximum nominal stress Σ_{max} as a function of the crack length a are presented in Figure 3.11. The individual effects of Σ^t and K_{IC} (through the prediction of LEFM) are also indicated by dashed lines on the figure. Thus, two clear mechanisms can be identified. For small cracks the nominal strength depends only on the tensile strength, identified in Figure 3.11, as $\Sigma^t = 2.4\ MPa$. The second mechanism is predicted for long cracks by lin-

ear elastic fracture mechanics (LEFM) by limiting the maximum stress intensity ($K_{I,max} = \Sigma_{max}\sqrt{\pi a}F(a/b)$), with F(a/b) given by Tada [114]) by the toughness value K_{IC}. It implies that $\Sigma_{max} = K_{IC}/\left(\sqrt{\pi a}F(a/b)\right)$ and associating the results of Figure 3.11 KIC is identified as equal to 0.4 $MPa \cdot m^{0.5}$. The intersection of the two predictions (dashed lines in Figure 3.11) is defined as the transition crack length [111] $a_t = \dfrac{K_{IC}^2}{(1.12 \times \Sigma^t)^2\pi} = 7\ mm$. The transition between these two mechanisms is shown to be well described by the energetic model proposed in [45, 111] (rapidly presented in Appendix B). A good fit is obtained for the mentioned values of Σ^t and K_{IC}, and the dimensionless parameter $r = 2.5$,(see Appendix B for more information about this parameter). The smooth transition between the two rupture mechanisms following the energetic model predictions is an indication of the consistency of the DEM approach for quasi-brittle materials.

Then the dimensionless parameters $\alpha = 0.20$ and $\beta = 1.36$ are identified scaling Equations 3.18 and 3.19 with $\Sigma^t = 2.4\ MPa$ and $K_{IC} = 0.4\ MPa \cdot m^{0.5}$ respectively. This same equations can now be employed to predict the effect of the contact strength and particle radius $\bar{R}$ over the strength and toughness of the material for identical micro structure and properties like stiffness ratio $k_{ratio} = 3.5$ and strength ratio $S_r = 1$.

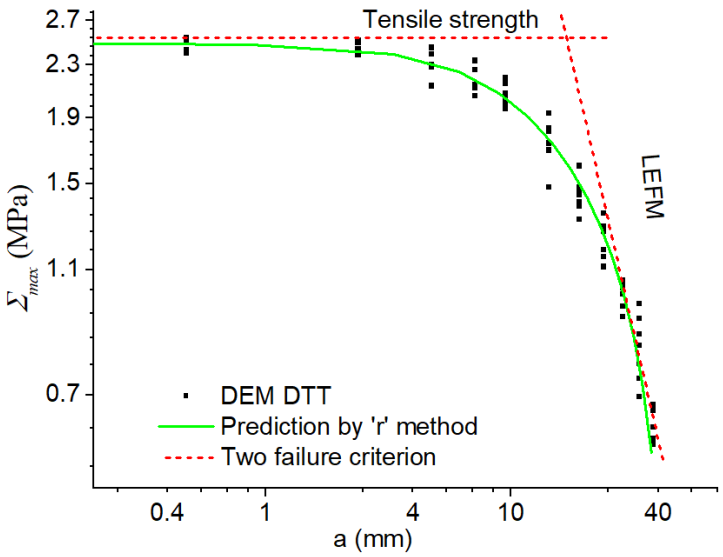

Figure 3.11: Nominal strength Σ_{max} as a function of the initial crack size a. The continuous line is the prediction given by the energetic formulation of [45] for tensile strength $\Sigma^t = 2.4\ MPa$, toughness $K_{IC} = 0.4\ MPa \cdot m^{-0.5}$ and the parameter $r = 2.5$.

3.6 Wedge-splitting test of the brittle material

In this section, the brittle analysis of wedge-splitting tests are presented, in order to further verify the fracture toughness with the bonded-particle model (BPM) in DEM. First, the geometry and the model calibration for the brittle material are described. Finally, the results are compared to the prediction of linear elastic fracture mechanics (LEFM).

3.6.1 Model preparation and material calibration

The DEM specimens are built according to the ASTM (American Society for Testing Material) standard for wedge-splitting test (WST) (see Figure 3.12). The loading is conducted by two circle walls. The loading rate $v_h = 1 \times 10^{-4}\ m/s$ promises a quasi-static system (see Appendix A). 5 samples are generated in DEM with different generator random seeds (see Appendix A), and applied with the same initial crack length a. The average radius of the particles $\overline{R}$ is $1.5\,mm$, with $R_{max} = 1.85\ mm$ and $R_{min} = 1.15\ mm$. The average particle number is 6603, and the average contact number is 13025. The micro parameters for the DEM specimens are $E_{cmod} = 20\ GPa$, $k_{ratio} = 3.5$, $f_{n,max} = 6000\ N$ and $S_r = 1$, which produces the material Young's modulus $E = 11.6\ GPa$ and Poisson's ratio $\nu = 0.3$ due to the calibration in Section 3.4. The fracture toughness is $K_{IC} = 2.0\ MPa \cdot m^{-0.5}$ theoretically by Equation 3.19 with $\beta = 1.29$.

3.6.2 Simulation results and verification by LEFM

The average result of WST for 5 specimens is the response curve: horizontal force as function of the opening displacements $F_h \times \delta_h$. As shown in Figure 3.13, for increasing δ_h, one may observe an initial elastic increase of F_h followed by a transition phase and a force decrease after a peak. The post-peak decrease may be associated to the clear propagation of the initial pre-crack (mode I - opening). A prediction from linear elastic fracture mechanics (LEFM) of this behaviour can be obtained by relating the material stress intensity factor $K_I(a)$ and the horizontal force $F_{h,\,theo}$ as follows [115],

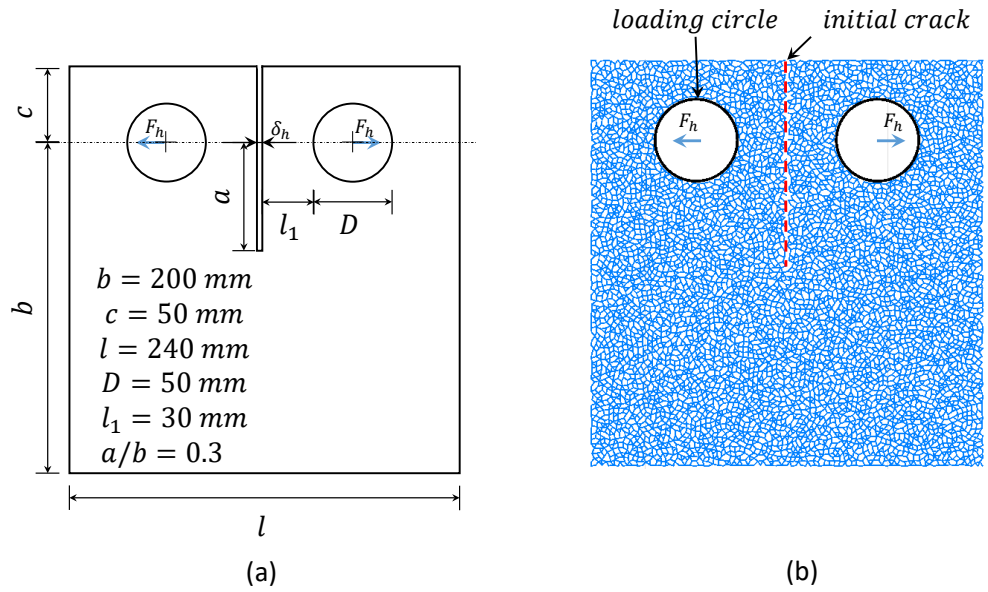

Figure 3.12: (a) The geometry of ASTM standard WST, (b) DEM simulation of WST in contact view.

$$\begin{cases} K_I = \dfrac{F_{h,\,theo}}{b}\sqrt{a}f(a/b), \\ f(a/b) = \dfrac{2(2+a/b)}{(1-a/b)^{3/2}}\dfrac{1}{\sqrt{a/b}}(0.443 + 2.32(a/b) - 6.66(a/b)^2 + 7.36(a/b)^3 - \\ \qquad 2.8(a/b)^4), \end{cases} \tag{3.20}$$

where $f(a/b)$ is the geometry correction factor, which has 0.5% accuracy for $a/b > 0.2$ [115].

The crack opening displacement δ_h along the load line is expressed as follows,

$$\begin{cases} \delta_{h,\,theo} = \dfrac{F_{h,\,theo}}{E'}V(a/b), \\ V(a/b) = (\dfrac{1+a/b}{1-a/b})^2(2.1630 + 12.129(a/b) - 20.065(a/b)^2 - 0.9925(a/b)^3 + \\ \qquad 20.609(a/b)^4 - 9.9314(a/b)^5), \end{cases} \tag{3.21}$$

which has 0.5% accuracy for $0.2 < a/b < 0.95$ [115].

With fracture toughness $K_{IC} = 2.1\ MPa{\cdot}m^{0.5}$ obtained by Equation 3.19 and the crack length ratio a/b ranging from 0.3 to 0.8, the theoretical maximum horizontal load $F_{h,\,theo}$ and crack opening displacement $\delta_{h,\,theo}$ are computed by Equation 3.20 and 3.21. In Figure 3.13, the comparison between the simulations and the prediction from LEFM with deviation of $\pm 20\%$ presents an acceptable agreement, which indicates that the strength of the contacts are directly correlated to the toughness of the material K_{IC} which governs the peak value of the force F_h^{max} and the dissipated energy during the rupture process (area under the curve $F_h(\delta_h)$.

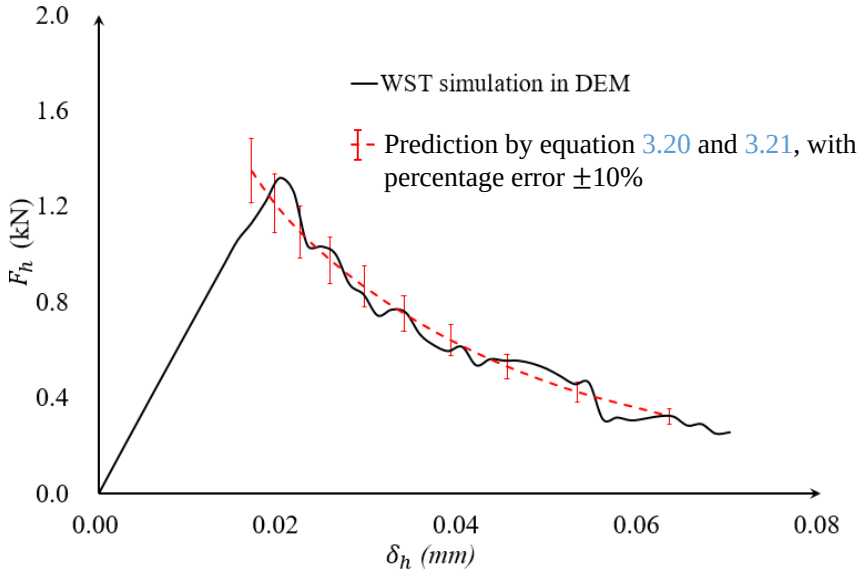

Figure 3.13: The results of simulation and theoretical prediction of WST.

3.7 Summary of this chapter

In this chapter, the basic elements of the discrete element approach used in the following chapters were presented. The sample generation allowing very low inner stresses is an example. The connection between the material properties and the model parameters was also discussed in elasticity and in rupture (for quasi-brittle materials). The parameter calibration also gives better understanding on the parameter determination for the following chapters.

Concerning the quasi-brittle rupture, the contact strength and the particle average radius (associated to the texture of the material) were directly related to the strength and toughness of the assembly, following a realistic prediction of an energetic model for size effects in cracked structures.

In the last part, an application of the DEM approach for wedge-splitting tests showed very consistent results according to linear elastic fracture mechanics LEFM. The limitations of LEFM on asphalt concrete modelling will be discussed in the next chapter.

Chapter 4

Wedge-splitting tests of asphalt concrete interfaces

Contents

4.1 Introduction

The fiber glass grids are usually placed between two layers of asphalt concrete (AC). The opening behaviour of this interface is studied by wedge-splitting tests (WST) in *SolDuGri* project. The aim of this chapter is to analyse the interface behaviour under monotonic transversal loading and propose a simple model which identifies the main parameters involved in its rupture process.

The first element to be discussed is the limitation of brittle assumption to characterize asphalt concrete like materials. Thus, a cohesive model implemented in a discrete element environment is proposed to characterize more realistically the sample materials. Based on physical evidences from experiments and simulations, an interfacial mechanism is identified and adopted in a simplified model. Finally, after the comparison of the different models, experimental results of WST [34] are analysed and the consistency of the theoretical approaches is verified.

4.2 Limitations of a brittle analysis of asphalt concrete

As observed in Chapter 3, the material toughness defines the peak force and the dissipated energy during WST with long initial crack. Discrete element simulation of brittle material has shown a very good agreement with linear elastic fracture mechanics (LEFM) [49]. A comparison between the prediction of LEFM and an experiment with asphalt concrete may clarify some characteristics of this type of materials.

The geometry of wedge-splitting specimens of Kim's experiments [94] is presented on Figure 4.1a. On Figure 4.1b, the opening force F_h as a function of the opening displacement δ_h is shown. The value of toughness $K_{IC} = 0.82\, MPa \cdot m^{0.5}$ can be identified from the peak force $F_h^{max} = 2.8\ kN$ due to the Equation as follows,

$$\begin{cases} K_I = \dfrac{F_h}{t\sqrt{b}} f(a/b), \\ \\ f(a/b) = \dfrac{2 + a/b}{(1 - a/b)^{3/2}}(0.76 + 4.8(a/b) - 11.58(a/b)^2 + 11.43(a/b)^3 - 4.08(a/b)^4), \end{cases} \tag{4.1}$$

where $b = 110\, mm$ and t $(= 50\, mm)$ is the specimen thickness.

If this value of toughness is adopted to define the energy release rate $G_I = K_I^2/E$ (Equation 2.35) and to predict the diagram $F_h \times \delta_h$ an unrealistic displacement level is obtained, where δ_h is obtained from the energy method as expressed by Equation 2.28.

If a higher value of energy release rate (instead of the usual relation from LEFM) may be allowed for the same toughness K_{IC}, a much better trend may be obtained for

$$G_I = \Gamma \frac{K_I^2}{E}, \tag{4.2}$$

where Γ is a scalar factor. On Figure 4.1b, $\Gamma = 6$ indicates a higher dissipation of energy during the rupture than one may get from a brittle material. This may offer a qualitative explain on the fracture behaviour of the asphalt concrete.

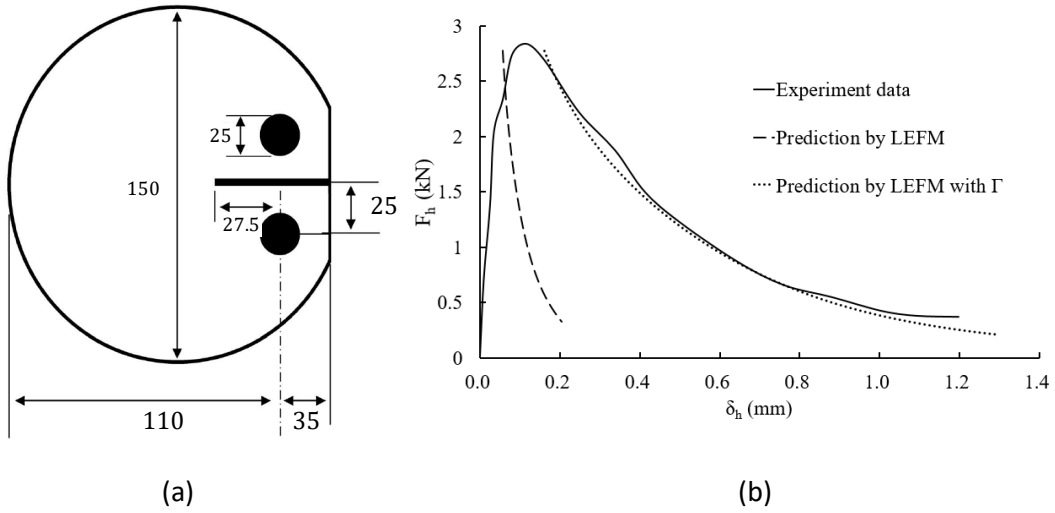

Figure 4.1: (a) Dimension (unit: mm) of wedge-splitting geometry of the tests performed by [95]. (b) Opening force F_h as a function of the displacement δ_h.

4.2.1 Energy dissipated by a fracture process zone (FPZ)

In LEFM, the crack tip is supposed perfectly defined in one single point. However, for heterogeneous materials, the crack tip presents usually a multi-cracked zone. This fracture process zone (FPZ) propagates with the crack tip (see Figure 2.15). One may represent schematically the crack tip with a FPZ by a series of parallel micro cracks of length l and width w (Figure 4.2a).

Considering the dimensions of Figure 4.2b, the stress intensity factor at each (micro) tip is $K_{Ii} = \overline{\sigma}\sqrt{h}$ [114], which represents an energy release rate (in plane stress)

$$G_{Ii} = \frac{\overline{\sigma}^2 h}{E}. \tag{4.3}$$

The average stress $\overline{\sigma}$ can be determined by an average of the expression given in Equation 2.2 in mode I over the distance l:

$$\overline{\sigma} = \frac{1}{l}\int_0^l \sigma(r)dr = \frac{1}{l}\int_0^l \frac{K_I}{\sqrt{2\pi r}}dr = K_I\sqrt{\frac{2}{\pi l}}. \tag{4.4}$$

The total energy release G_I, would be the summation of the contribution of $n = w/(2h)$ micro cracks by Equation:

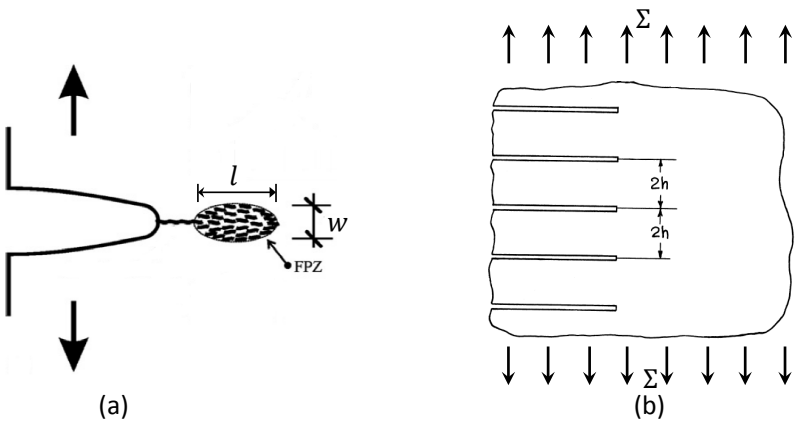

Figure 4.2: (a) Schematic view of a crack presenting a fracture process zone (FPZ) and the approximative tensile stress field associated. (b) Zoom at the crack tip [114].

$$G_I = nG_{Ii} = \left(\frac{w}{\pi l}\right)\frac{K_I^2}{E}, \tag{4.5}$$

where the definition of $\Gamma = w/(\pi l)$ emerges to complete the proposition in Equation 4.2.

In terms of discrete element modelling, a value of $\Gamma > 1$ indicates that the rupture process must be controlled beyond the contact strength, that is to say, to manage directly the energy release of a contact.

4.3 Cohesive model in DEM

The simplest way of controlling strength and energy release of a contact is by a cohesive contact model. The generally required characteristics for cohesive constitutive relationships are summarized as follows [78]:

- The traction separation relationship is independent of any superposed rigid body motion.
- The work to create a new surface is finite, and its value (i.e. area under a traction separation curve) corresponds to the fracture energy.
- The mode I fracture energy is usually different from the mode II fracture energy.
- A finite characteristic length scale exists, which leads to a complete failure condition, i. e. no load-bearing capacity.
- The cohesive traction across the fracture surface generally decreases to zero

while the separation increases under the softening condition.
• A potential for the cohesive constitutive relationship may exist, and thus the energy dissipation associated with unloading/ reloading is independent of a potential.

4.3.1 Traction separation law

A bilinear (linear elasticity and linear softening) traction separation law is used on the following to describe the fracture behaviour, which has been employed for different materials [85–87].

4.3.1.1 Force and displacement

The relation between force and displacement takes the same shape of the contact law presented in Chapter 3. Normal and tangential components of the forces and displacements are defined in Figure 4.3. Thus, normal and tangential forces, respectively, f_n and f_s are defined as

$$\begin{cases} f_n = k_n(1-D)\delta_n, \\ \\ f_s = k_s(1-D)\delta_s, \end{cases} \tag{4.6}$$

where k_n and k_s represent the normal and shear stiffness, δ_n and δ_s represent normal and shear displacement. A damage state variable D is associated to describe and to control the contact rupture behaviour. A contact completely intact is denoted by $D = 0$, whilst a contact completely damaged is described by $D = 1$ (otherwise $0 \leq D \leq 1$).

The same damage quantity is associated to both components of the force, since they represent a single resultant force

$$f = \sqrt{f_n^2 + f_s^2}. \tag{4.7}$$

The displacement associated to the direction of f is

$$\delta = \delta_n sin\theta + \delta_s cos\theta, \tag{4.8}$$

where $\theta = arctan(f_n/f_s)$.

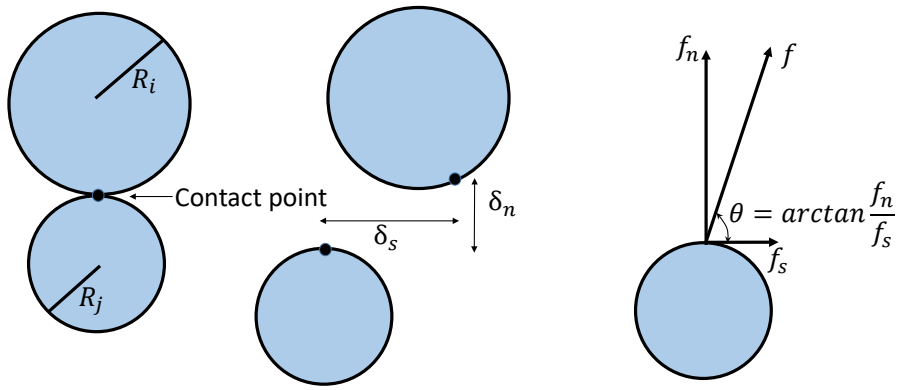

Figure 4.3: Contact displacements and forces.

4.3.1.2 Effective stiffness and strength

The stiffness of the contact depends on the direction, if $k_n \neq k_s$. The effective stiffness k_e is defined to relate f and δ, that is to say, following the direction described by the angle θ. The combination of Equations 4.7 and 4.8 leads to

$$k_e = f/\delta = \frac{\sqrt{f_n^2 + f_s^2}}{\delta_n sin\theta + \delta_s cos\theta} = \frac{k_n k_s}{k_n cos^2\theta + k_s sin^2\theta}. \tag{4.9}$$

In the same way, the strength of the contact may depend on the direction. Keeping for simplicity a similar shape as Equation 4.9, the peak force f^{max} is defined as

$$f^{max} = \frac{f_n^{max} f_s^{max}}{f_n^{max} cos^2\theta + f_s^{max} sin^2\theta} \tag{4.10}$$

where f_n^{max} and f_s^{max} are respectively the normal and shear peak forces of the contact.

The contact normal and tangential strengths can be simply defined as

$$\begin{aligned} \sigma_n &= \frac{f_n^{max}}{2t \times min(R_i, R_j)}, \\ \sigma_s &= \frac{f_s^{max}}{2t \times min(R_i, R_j)}, \end{aligned} \tag{4.11}$$

respectively. R_i and R_j are the radius of the two particles in contact.

4.3.1.3 Fracture energy and energy release rate

The energy released during the contact rupture, the fracture energy U_c, is the area under the $f \times \delta$ curve (see Figure 4.4)

$$U_c = \frac{f^{max}\delta^{max}}{2}, \tag{4.12}$$

where δ^{max} is the maximum value of the displacement δ.

The energy release rate is the energy per unity of propagated area and can be defined for a contact as

$$G_c = \frac{U_c}{t \times min(R_i, R_j)}, \tag{4.13}$$

where R_i and R_j are the radius of the two particles in contact.

4.3.1.4 Damage law

In Figure 4.4, the variable of damage D can be expressed through the displacement δ as

$$D = \frac{\delta^{max}}{\delta}\frac{\delta_e - \delta}{\delta_e - \delta^{max}}, \tag{4.14}$$

where $\delta_e = f^{max}/k_e$ is the elastic limit. The damage theory allows a very simple description of unloading and reloading paths, imposing that damage value cannot decrease. If the calculated value of D (through Equation 4.14) is eventually lower than the present value of D, its value keeps unaltered. It means that unloading/reloading paths follow a slope $(1 - D)k_e$ until damage value increases and softening behaviour is then observed again.

The total rupture of the contact is obtained for $\delta = \delta^{max}$ (which corresponds to $D = 1$). At this point, the contact forces f_n and f_s are set to zero. Only the elasticity in compression remains to work and the normal and shear stiffness are inherited from k_n and k_s.

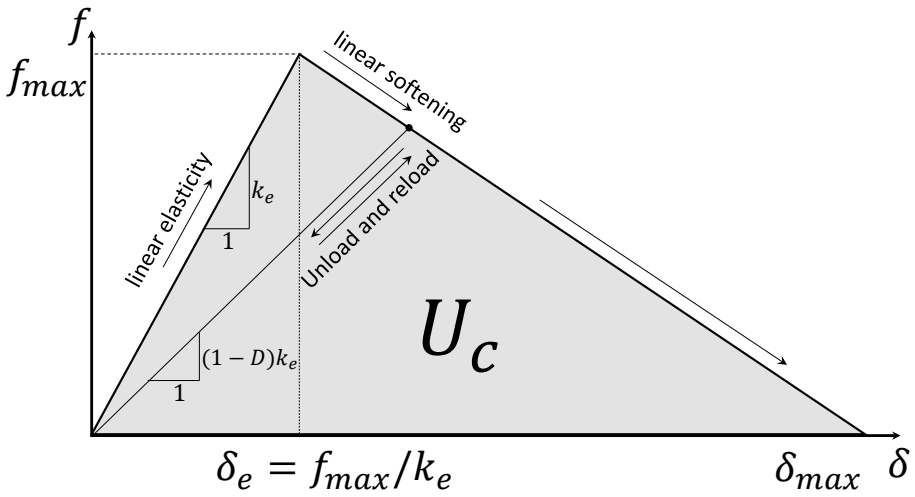

Figure 4.4: Bilinear traction separation law for cohesive contact model.

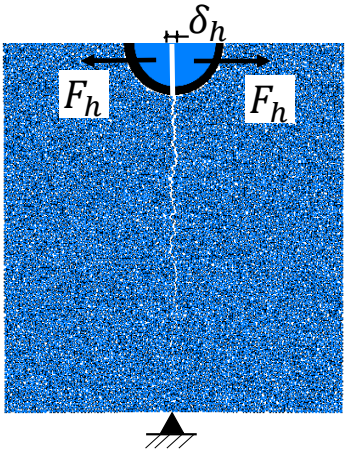

Figure 4.5: The geometry of numerical sample for initial verifications.

4.3.2 WST simulations with cohesive contact model - preliminary tests

Initial verifications related to the model (particle size and loading rate effects) are first discussed. The geometry of numerical sample is presented in Figure 4.5.

Each sample has the same shape and dimensions ($200\,mm \times 200\,mm$). The traction separation law presented in the previous section 4.3.1 is adopted. The elasticity parameters are $E_{cmod} = 10\,GPa$, $k_{ratio} = 4.5$ (see the definition in Section 3.2), which correspond the material properties in [22]: Young's modulus $E = 5.4\,GPa$ and Poisson's ratio $\nu = 0.34$. The strength of the contact $\sigma_n = \sigma_s = 5 \times 10^4\,Pa$,

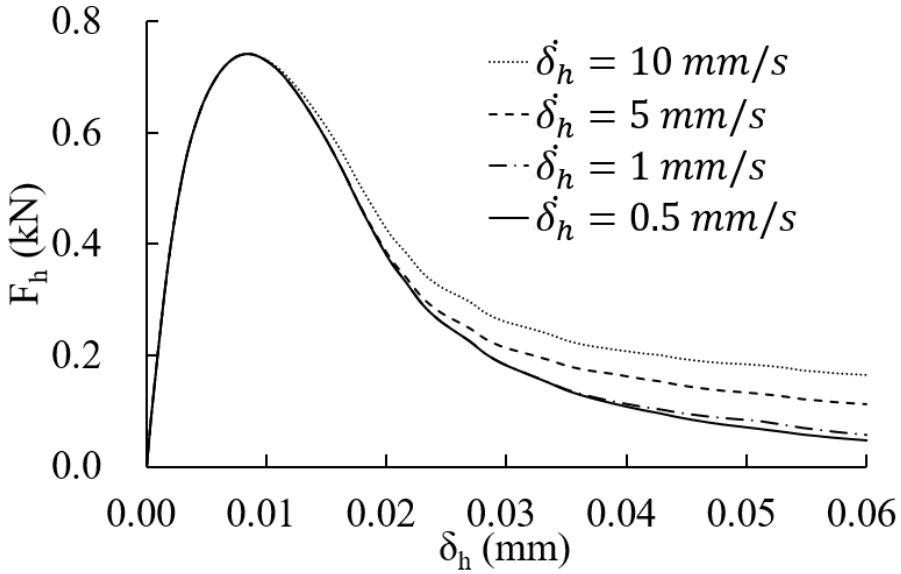

Figure 4.6: Force F_h as function of the displacement δ_h for different loading rate $\dot{\delta}_h$ in DEM simulations.

and the energy release rate of the contact is $G_c = 0.3\,N/m$.

4.3.2.1 Loading rate effect

Loading rate calibration is conducted to obtain quasi-static condition. The horizontal rate of loading plates should be low enough to avoid dynamic effects, and it should be high enough for an acceptable computational time.

In this chapter, specimens under different conditions are required, thus loading rate calibrations are carried out a certain number of times. Herein, one set of calibration is presented as an example.

WSTs of a specimen with average radius $\overline{R} = 1\,mm$ are repeated under different loading rates $\dot{\delta}_h = 10\,mm/s$, $5\,mm/s$, $1\,mm/s$ and $0.5\,mm/s$. The force response F_h as a function of the imposed displacements δ_h are presented in Figure 4.6 for each loading rate.

Only the post-peak behaviour is affected by the loading rate $\dot{\delta}_h$. Before any contact rupture, the relative velocities between particles in contact are very small which may induce neglectful viscous forces. During rupture, the propagation of the crack is associated to the displacement of the tip. It causes a growth of the relative (opening) velocity between the particles near this point. An increase on the loading rate $\dot{\delta}_h$ is naturally reflected over the the viscous contact forces

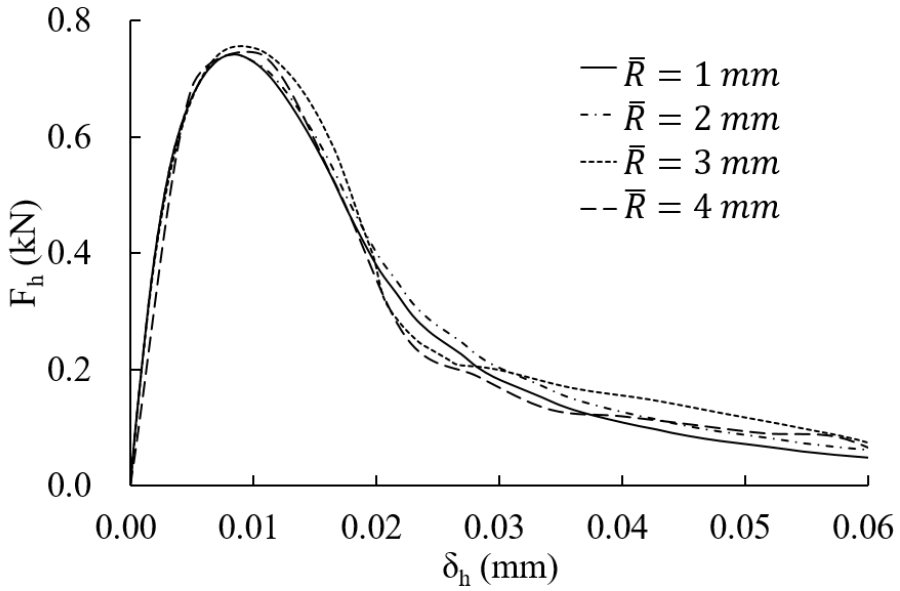

Figure 4.7: Force F_h as function of the displacement δ_h for different particle radius.

which may also increase. On the example which is analysed on Figure 4.6, for $\dot{\delta}_h \leq 0.5\,mm/s$ this effect becomes neglectful, with curves of an almost identical shape.

4.3.2.2 Particle size effect

The effect of average particle size $\overline{R}$ in DEM on the material rupture has been proved as $K_{IC}/\Sigma^t \propto \sqrt{\overline{R}}$ in Chapter 3. In this chapter, the effect of particle size on the material rupture is studied by WST with specimens of different $\overline{R}$.

A total of 12 tests are considered: four different particle radius $\overline{R} = 1\ mm$, $2\ mm$, $3\ mm$ and $4\ mm$ (with 3 specimens per radius). Rupture results are roughly related to elastic behaviour, strength and energy release. Discrete element simulations of WST are performed to verify if any size effect related to the particle radius $\overline{R}$ may be observed. The average force response F_h as a function of the imposed displacements δ_h are presented on Figure 4.7 for each particle size.

The results are, as expected, independent on the particle size. The force F_h increases following an elastic path, which is shown in Section 3.4.1 to be independent on particle size. An identical energy release (surface under the curve $F_h \times \delta_h$) indicates that the energy release rate of the contact G_c effectively defines the energy release rate of the material G_{IC}.

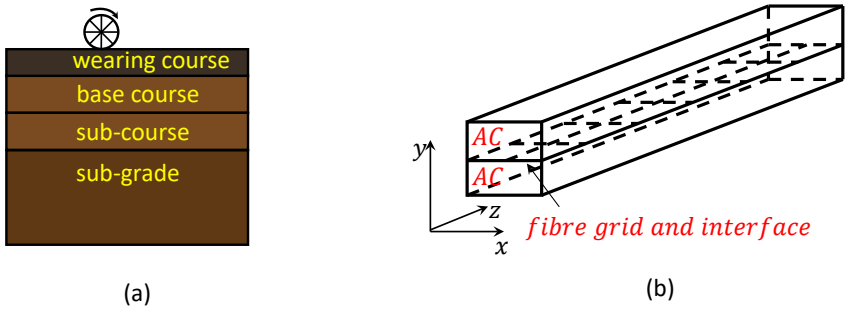

(a) (b)

Figure 4.8: (a) Pavement cross section. (b) Zoom in the top layer of pavement and the grid between asphalt concrete (AC) layers.

4.4 Modelling wedge-splitting tests (WST) with interface

In this section, the experimental behaviour is associated to simulations and, considering some physical evidences, a theoretical mechanism for the interface behaviour is proposed. A parametric study comparing the parameters defined by the interface mechanism and DEM parameters is then conducted. The proposed mechanism is then adopted on the analysis of WST performed by [34]. Finally, some perspectives on the identification of interface parameters are addressed.

4.4.1 Context and description of the geometry

The fiber glass grids are usually placed between two asphalt concrete layers. The grid contributes as a reinforcement in the direction inside the plane xy (see Figure 4.8). However, in z direction, the grid and the resin used to stick it to the asphalt layers, form an interface.

In *SolDuGri* project, the opening behaviour of the interface in monotonic loading was performed by wedge-splitting tests (WST) during the thesis work of Gharbi [22]. The different samples were obtained from a section of pavement specially constructed for the project. The samples (Figure 4.9a) were sawed following the dimensions $H \times 200mm \times 150mm$ indicated in Figure 4.9b.

Some samples present fiberglass grids inside the interfacial layer and other samples have only emulsion. A semi-circular groove with a diameter of 56 mm (instead of the usual rectangular one) is made by coring to simplify the preparation of the sample. A pre-crack of 30 mm of length and 5 mm of width is created by sawing the bottom of the semicircular groove.

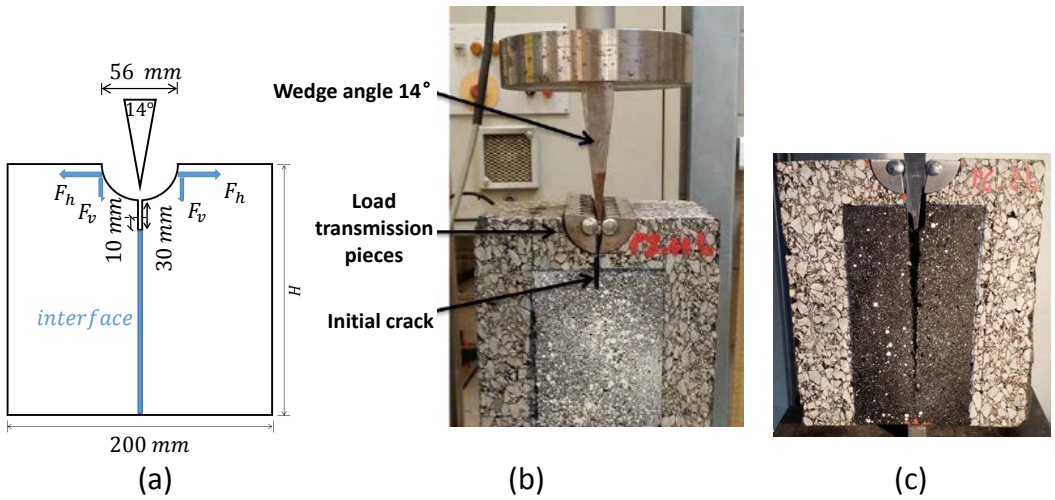

Figure 4.9: (a) Sample used in the WST and (b) detailed geometry of the tests performed by [22] and (c) sample and the crack after test.

The vertical motion of the triangular wedge (with an angle of 14^o) leads to the resultant force acting on the AC samples which can be decomposed into horizontal and vertical components (F_h and F_v), which induces a rupture by crack propagation. A vertical support is placed at the bottom of the sample, in the middle position to block the vertical motion. During loading, the vertical force on the wedge $2F_v$, the opening displacement in position A and the position of the crack tip are measured.

4.4.2 Physical evidences of the interface rupture - experimental and simulation results

4.4.2.1 Simulation setup

The interface is treated as a single material representing the homogenized behaviour of the multilayer composite composed by resin and fiber grid. Thus, the model presents two different regions, with distinct mechanical properties: asphalt concrete (AC) and interface as shown in Figure 4.10.

On the first simulation of a WST interface, the average radius of the particles $\overline{R} = 1\ mm$ is adopted, the interface presents a thickness of $4\ mm$ ($4 \times \overline{R}$). The traction separation law presented in Section 4.3.1 is adopted. The DEM parameters of the asphalt concrete are: contact modulus $E_{cmod} = 20\,GPa$, stiffness ratio $k_{ratio} = k_n/k_s = 4.5$, and contact strength $\sigma_n = \sigma_s = 4 \times 10^6\,Pa$,

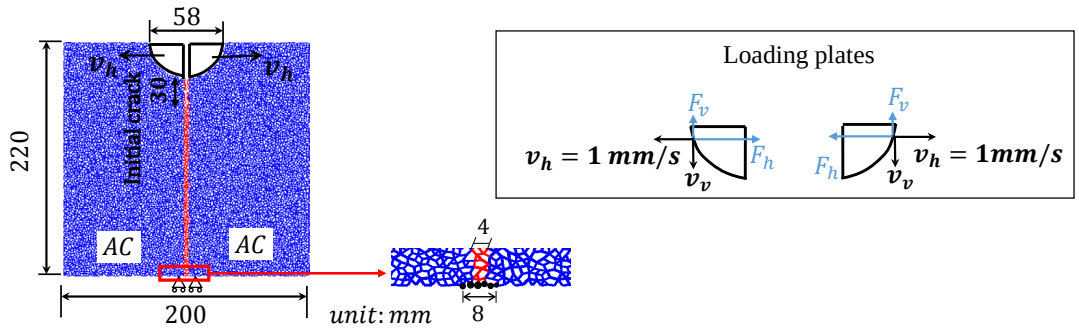

Figure 4.10: Characterization of the interface geometry on discrete element simulations.

$G_c = 100\,N/m$, corresponding to the following material properties: Young's modulus $E = 11\,GPa$, Poisson's ratio $\nu = 0.34$, tensile strength $\Sigma^t = 2 \times 10^6\,Pa$ and energy release rate $G_{IC} = 120\,N/m$ due to the calibration. Due to the calibration based on the experimental results within a percentage error of $\pm 15\%$, for the interface, the contact parameters are: $E_{cmod} = 5 \times 10^6\,Pa$, $k_{ratio} = 1$, $\sigma_n = \sigma_s = 1.4 \times 10^4\,Pa$, $G_c = 15\,N/m$.

The parameters of AC correspond to the material of the samples in [34].

4.4.2.2 Boundary conditions

The loading is entirely controlled by imposed velocities in WST simulations. The particles ranging in 8 mm in the bottom center of the sample are set only movable horizontally acting as vertical support, blocking the vertical displacement (see Figure 4.11). On the top, the opening motion of the two loading plates (horizontal velocity $v_h = 1\,mm/s$ and vertical velocity v_v) mimic the effect of the vertical quasi-static displacement of a triangular wedge. The acting forces F_h and F_v are measured on the plates. To get the same force ratio ($F_v/F_h = \tan(14°/2)$) as experiments, the vertical velocity v_v is imposed as follows,

$$v_v(t) = \eta \frac{F_v - F_h \times tan\frac{14°}{2}}{k_n \Delta t}, \tag{4.15}$$

where Δt is the time step, k_n is the stiffness between the loading plates and the AC particles, η is a damping parameter used to control the acceleration of the plate. A value of $\eta = 0.5$ has been used on the simulations.

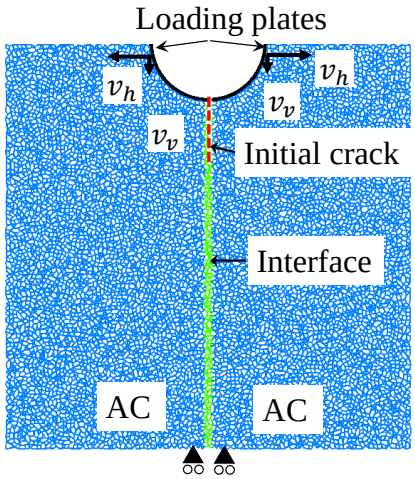

Figure 4.11: Wedge-splitting geometry and boundary conditions.

The effect of controlling F_h/F_v is presented in Figure 4.12. F_h/F_v has been successfully restrained ranging from 0.11 to 0.13.

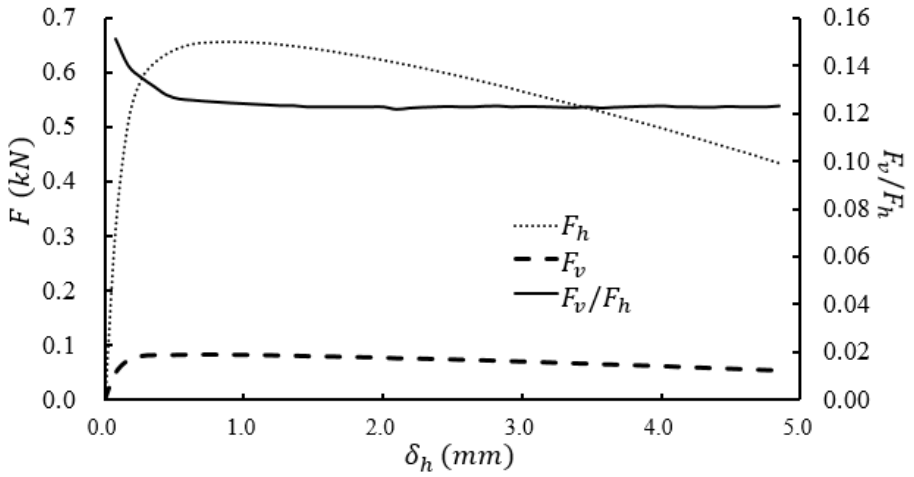

Figure 4.12: Characterization of the interface geometry on discrete element simulations.

4.4.2.3 Results analysis

The characterisation of the heterogeneous interface is more complex. The homogenized properties are obtained by approximation of the experimental curve opening force F_h versus displacement δ_h (see Figure 4.13. The initial part of the curve allows a precise identification of the average elastic properties. The post-

peak behaviour enables the identification of strength and energy parameters.

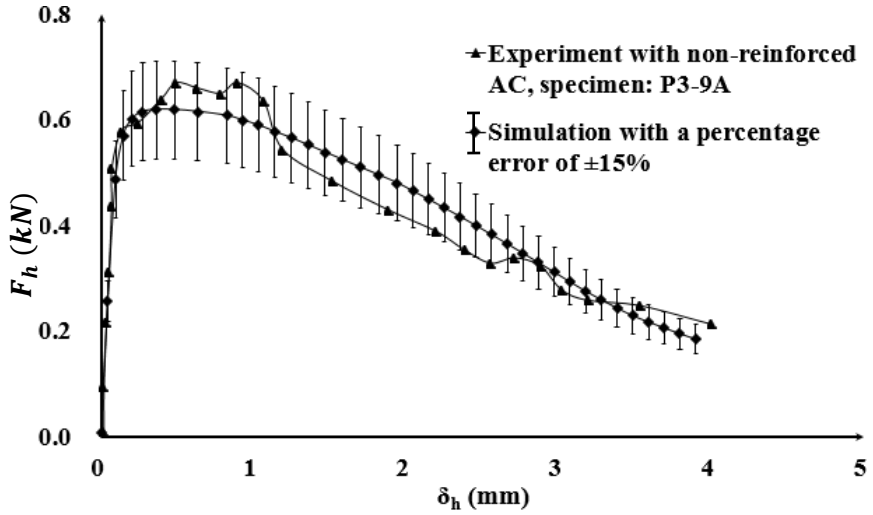

Figure 4.13: Force F_h as a function of the displacement δ_h. Comparison between simulations and experiments [34].

The shape of the curve is globally well reproduced by DEM results. A single experimental sample is compared to an average of 3 DEM simulations. The results indicate a much smaller stiffness of the interface compared to the asphalt concrete. Experimentally, one may observe that the rupture occurs always on the interface. The induced crack never invades the asphalt concrete regions as visible on the example on Figure 4.14a. Numerically, the same type of rupture is reproduced (see Figure 4.14b) due to the difference between the strengths of the asphalt concrete and the interface.

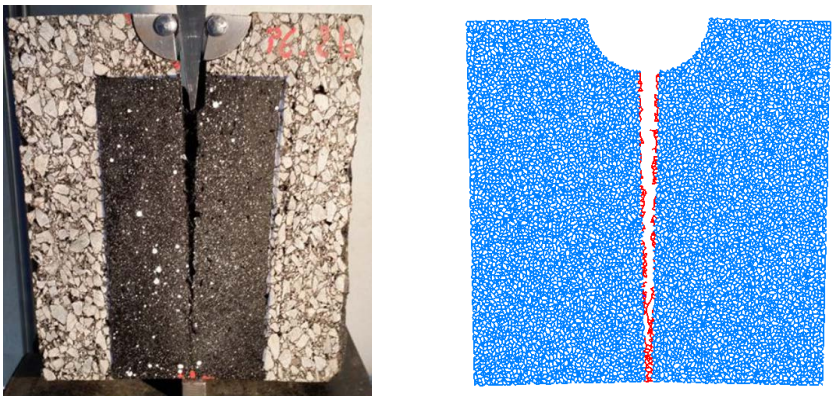

(a) (b)

Figure 4.14: (a) Experimental [34] and (b) numerical samples after WST.

4.4.3 Interface model (IM)

Based on the physical elements presented in Section 4.4.2, a model which focuses on the interface response is presented. The small thickness of the interface, associated to much stiffer asphalt concrete strongly suggests that this layer is fundamentally subjected to tension stresses during WST.

Considering only half of the wedge-splitting sample Figure 4.15a, a scheme of the interface layer with width $2 \times w_i$ where i is the subscript for interface, length equal to the sample height minus the initial crack length $b = H - a$, and thickness identical to the sample thickness t, is shown on Figure 4.15b. One may suppose the height of the interface divided into n equal parts. It allows to define a basic unit j of interface with a width w_i, length $b_i = (H - a)/n$ and thickness t, which may behave in tension as a simple spring, as shown on Figure 4.15c. Then the system of WST interface can be simplified to spring-rigid system as presented in Figure 4.16.

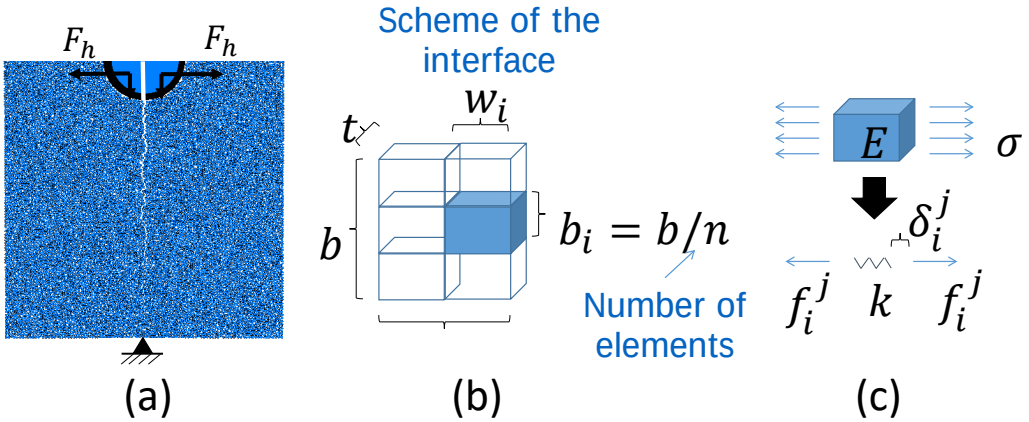

Figure 4.15: (a) Wedge-splitting sample, (b) interface dimensions, (c) interface unit part and equivalent spring under tension.

4.4.3.1 Elastic behaviour of the interface

The stress σ_i^j and the strain ε_i^j acting on an interface unit j may be simply related to the spring force f_i^j and elongation δ_i^j by the expressions:

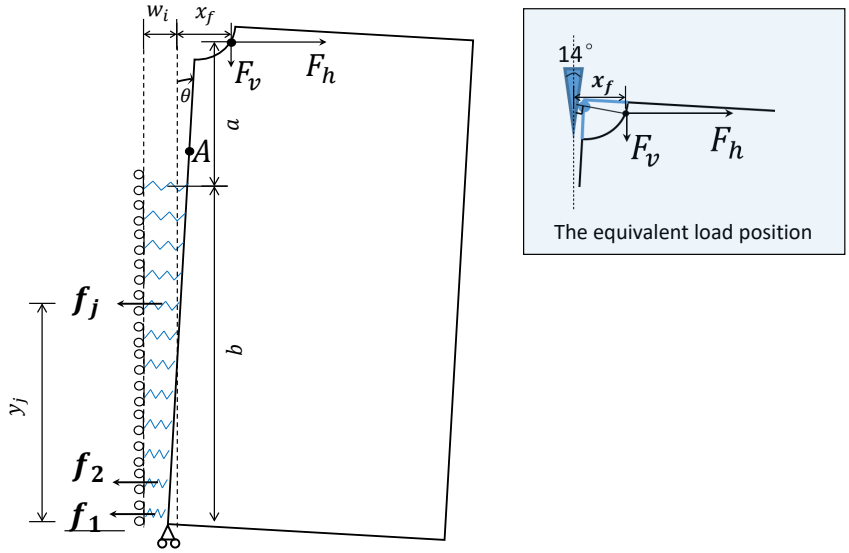

Figure 4.16: Elongation of the springs imposed by the rigid motion of the asphalt concrete element. Resulting forces and application points.

$$\begin{aligned} \sigma_i^j &= \frac{f_i^j}{b_i \times t}, \\ \varepsilon_i^j &= \frac{\delta_i^j}{w_i}. \end{aligned} \tag{4.16}$$

Isolating the force f_i^j from Equation 4.16, the elastic behaviour of the spring can be expressed by

$$\begin{cases} f_i^j = k_i \delta_i^j, \\ k_i = \left(\dfrac{E_i}{w_i}\right) b_i t = \left(\dfrac{E_i}{w_i}\right) \dfrac{(H-a)}{n} t, \end{cases} \tag{4.17}$$

where E_i is the homogenized Young's modulus of the interface.

4.4.3.2 Strength and energy release rate of the interface

Considering the good results of the discrete element model, the springs are supposed to have the same bi-linear force-displacement law.

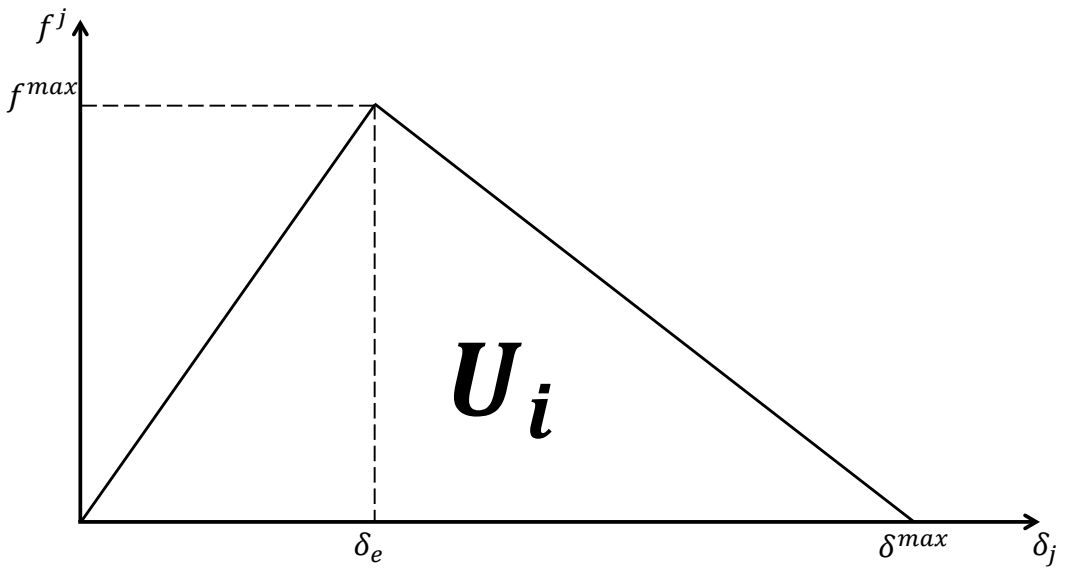

Figure 4.17: Force-displacement behaviour of the equivalent springs.

The peak force f^{max} can be related to the strength of the homogenized material of the interface Σ_i^t by the simple relation

$$f^{max} = \Sigma_i^t \times (b_i \times t) = \Sigma_i^t \frac{(H-a)t}{n}. \tag{4.18}$$

Similarly to the discrete element contact model (see Equations 4.12 and 4.13, the energy release rate of the interface can be written as

$$G_i = \frac{U_i}{t \times b_i} = \frac{f^{max}\delta^{max}n}{2t(H-a)}, \tag{4.19}$$

where U_i is the fracture energy of the interface unit j and δ^{max} is the maximum value of the elongation δ_j.

Figure 4.17 summarizes the force-displacement behaviour of the equivalent springs characterizing the interface local response. If $\delta_j > \delta^{max}$, the force f_j is automatically set to zero, which characterizes the rupture of the spring.

4.4.3.3 Force and moment balance

Since all the deformation is assumed to take place in the interface, the springs are attached to a rigid body which represents the asphalt concrete layer. As

shown in Figure 4.15, all elongations can be determined based on the imposed displacement δ_h and the interface opening angle θ by the expression:

$$\delta^j = \delta_h - (H - y^j)\tan\theta, \tag{4.20}$$

where y^j is the position of each spring j. The value of each force f^j is determined by the bi-linear diagram of force-displacement (see Figure 4.17) according to δ^j value.

By a balance of horizontal forces, the total force F_h is determined by the summation of the forces of all springs:

$$F_h = \sum_{j=1}^{n} f^j, \tag{4.21}$$

where n is the number of springs. The vertical force is directly calculated by $F_v = F_h \tan(7^o)$.

By a moment balance, the total force F_h can also be determined as

$$F_h = \frac{1}{y_f}\left(\sum_{j=1}^{n} f^j y^j - F_v x_f\right), \tag{4.22}$$

where x_f and y_f are respectively the horizontal and vertical positions of the measured forces F_h (and F_v), equivalent to the positions of experiments and simulations.

The displacement increases monotonically and the corresponding F_h is calculated based on the force and moment balance. The corresponding crack opening displacement is obtained by the calculation of the similar triangles.

4.4.3.4 Model parameters

The interface is defined by its geometry, and material properties like elasticity, strength, fracture energy and the resolution of the model.

Geometry: height H, width w_i and initial crack size a.

Stiffness: defined by the ratio between the Young's modulus and the interface thickness E_i/w_i.

Strength: homogenized tensile strength of the interface Σ_i^t.

Energy: energy release rate of the interface G_i.

Resolution: number of springs n.

4.4.3.5 Solution of the system and convergence

The value of the opening angle θ evolves at each given δ_h. These values are non linearly related due to the non-linearity induced by the force-displacement law of the springs. In practice, the value of θ is obtained by minimization of the difference between the results of Equations 4.21 and 4.22. The solution of the interface model allows the identification of the force F_h for each given δ_h.

An adequate resolution level, depending on the number of springs n of the system, is obtained for relatively low n as shown in Figure 4.18. The dimensions of interface model are height $H = 200\,mm$, $2 \times w_i = 4\,mm$, $a = 56\,mm$. The mechanical parameters are $E_i = 2 \times 10^6\,Pa$, $\Sigma_i^t = 14000\,Pa$, $G_i = 15\,N/m$. The results are substantially the same for n equal to 10 to 25 springs. An convergent result is obtained for more than 20 springs.

4.4.4 Parametric study - Discrete element and interface model results

The two models adopted on the analysis of the interface wedge-splitting test discussed in this chapter, discrete element and interface models present a comparable set of parameters. A parallel parametric study is presented in this section concerning the interface material properties (stiffness, strength and energy) and the thickness of the interface.

Wedge-splitting tests with dimensions width $W = 200\,mm$, height $H = 220\,mm$, thickness $t = 1000\,mm$ and initial crack size $a = 56\,mm$ and an approximative interface thickness $2 \times w_i = 4\,mm$ are adopted in the following examples. In discrete element model (DEM), the simulations are performed with an average radius $\overline{R} = 1\,mm$, size ratio $R_{max}/R_{min} = 1.6$. An average of 3 samples is presented. For the interface model (IM), a number of springs $n = 72$ is adopted.

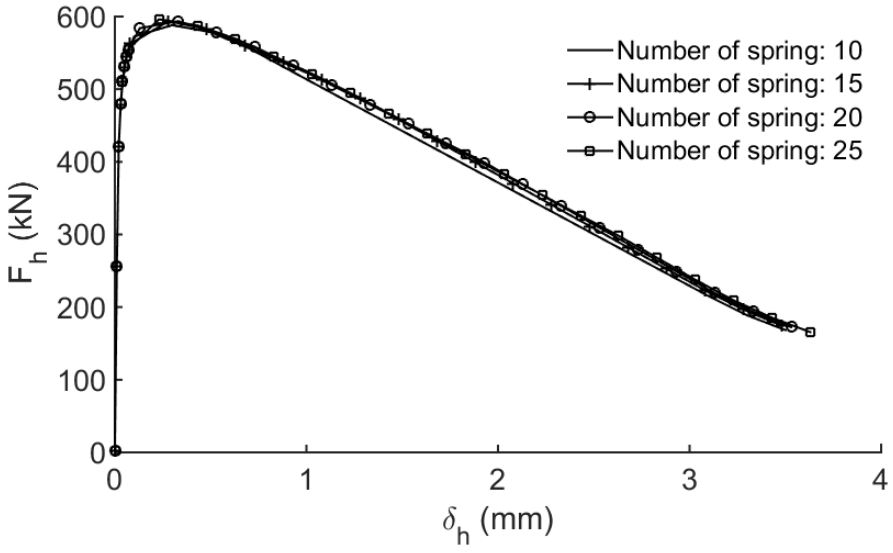

Figure 4.18: Force F_h as function of the displacement δ_h. Effect of the number of springs n over the interface model results.

Concerning the material parameters, when it is not indicated, the following parameters are taken into account in DEM: for the asphalt concrete a Young's modulus $E_{ac} = 11\,GPa$, Poisson's ratio $\nu_{ac} = 0.34$, tensile strength $\Sigma^t_{ac} = 2 \times 10^6\,Pa$, contact energy release rate $G_{IC,\,ac} = 120\,N/m$; for the contact of interface $E_{int} = 8 \times 10^5\,Pa$, $\Sigma_{int} = 14000\,Pa$ and contact energy release rate $G_{int} = 5.5\,N/m$.

4.4.4.1 Stiffness

The effect of stiffness is obtained for different sets of Young's modulus in DEM $8 \times 10^5 Pa \leq E_{int} \leq 8 \times 10^7 Pa$. In Table 4.1, we present the the parameters of the IM parameters fitting the curves force F_h versus displacements δ_h in Figure 4.19a. In Figure 4.19b, one may observe the perfect linearity between DEM and IM elastic parameters, respectively E_{int} and E_i. The main effect of the stiffness is observed on the elastic increase of the force before the peak force. However, the peak force is also affected by the elasticity, where higher stiffness tends to induce higher peak forces F_h.

4.4.4.2 Strength

The effect of the strength is obtained for a different set of interface tensile strength in DEM $0.6 \times 10^4\,Pa \leq \Sigma^t_{int} \leq 2.2 \times 10^4\,Pa$. In Table 4.2, we present the parameters of the IM parameters fitting the curves force F_h versus displacements δ_h

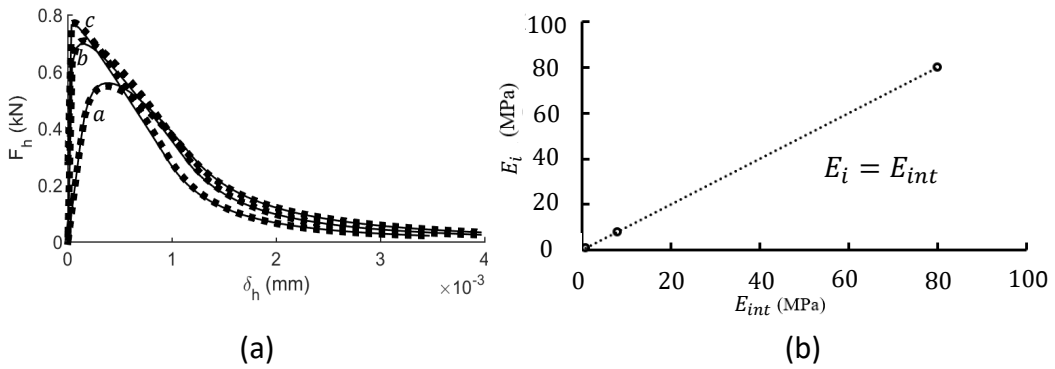

Figure 4.19: (a)Force F_h as a function of the displacement δ_h and (b) relation between the elastic parameters E_{int} and E_i.

Table 4.1: Different modulus used in DEM simulations and the associated IM parameters.

	DEM			**IM**		
	$E_{int}\,(Pa)$	$\Sigma_{int}((Pa))$	G_{int}	$E_i\,(Pa)$	$\Sigma_i(Pa)$	$G_i(N/m)$
a	8×10^5	1.4×10^4	5.5	8×10^5	1.16×10^4	6.6
b	8×10^6	1.4×10^4	5.5	8×10^6	1.16×10^4	6.6
c	8×10^7	1.4×10^4	5.5	8×10^7	1.16×10^4	6.6

on Figure 4.20a. On Figure 4.20b, one may observe the perfect linearity between DEM and IM strength parameters, respectively Σ^t_{int} and Σ^t_i. The main effect of the strength is observed on peak value of the force F_h, roughly proportionally. Since the fracture energy is kept constant, the area under the curve $F_h \times \delta_h$ tends naturally to be always the same.

Table 4.2: Different strength used in DEM simulations and the associated IM parameters.

	DEM			**IM**		
	$E_{int}\,(Pa)$	$\Sigma_{int}((Pa))$	G_{int}	$E_i\,(Pa)$	$\Sigma_i(Pa)$	$G_i(N/m)$
a	8×10^5	0.6×10^4	5.5	8×10^5	0.70×10^4	6.6
b	8×10^5	1.0×10^4	5.5	8×10^5	1.16×10^4	6.6
c	8×10^5	1.4×10^4	5.5	8×10^5	1.62×10^4	6.6
d	8×10^5	1.8×10^4	5.5	8×10^5	2.10×10^4	6.6
e	8×10^5	2.2×10^4	5.5	8×10^5	2.56×10^4	6.6

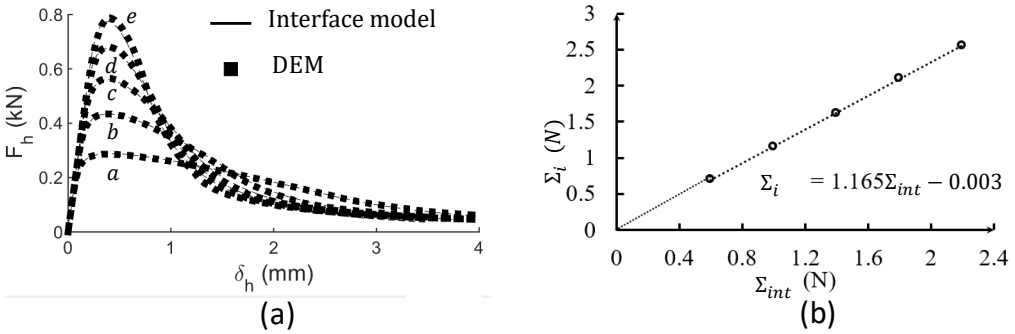

Figure 4.20: (a) Force F_h as a function of the displacement δ_h for different interface strength $0.6 \times 10^4\, Pa \leq \Sigma_{int}^t \leq 2.2 \times 10^4\, Pa$. (b) Relation between the strength parameters Σ_{int}^t and Σ_i^t.

4.4.4.3 Energy release rate

The effect of the energy release rate is obtained for a different sets of interface parameters in DEM $1\, N/m \leq G_{int} \leq 20\, N/m$. In Table 4.3 the parameters of the IM parameters fitting the curves force F_h versus displacements δ_h in Figure 4.21a. In Figure 4.21b, one may observe the perfect linearity between DEM and IM energy parameters, respectively G_{int} and G_i. The main effect of the energy release rate is observed on the area under the curve $F_h \times \delta_h$ which grows proportionally with $G_{IC,\,int}$ (the area is equal to $G_{IC,\,int} \times (H - a)t$). The shape or the whole curve depends on this parameter since it also affects the peak value of F_h.

Table 4.3: Different energy release rate used in DEM simulations and the associated IM parameters.

	DEM			**IM**		
	$E_{int}\,(Pa)$	$\Sigma_{int}((Pa))$	G_{int}	$E_i\,(Pa)$	$\Sigma_i(Pa)$	$G_i(N/m)$
a	8×10^5	1.4×10^4	1	8×10^5	1.62×10^4	1.5
b	8×10^5	1.4×10^4	5	8×10^5	1.62×10^4	6.0
c	8×10^5	1.4×10^4	10	8×10^5	1.62×10^4	11.8
d	8×10^5	1.4×10^4	15	8×10^5	1.62×10^4	17.5
e	8×10^5	1.4×10^4	20	8×10^5	1.62×10^4	23.0

4.4.4.4 Effect of the thickness of the interface

The exact definition of the thickness of the interface w_i is, in practice, quite complicated, considering the granular nature of the asphalt concrete. The frontier

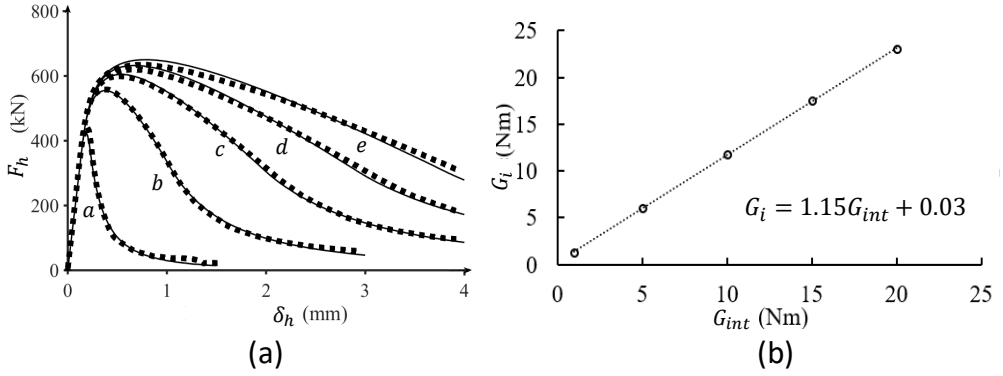

Figure 4.21: Force F_h as a function of the displacement δ_h for different energy release rates of the interface $1\,N/m \leq G_{int} \leq 20\,N/m$. (b) Relation between the energy parameters G_{int} and G_{ic}.

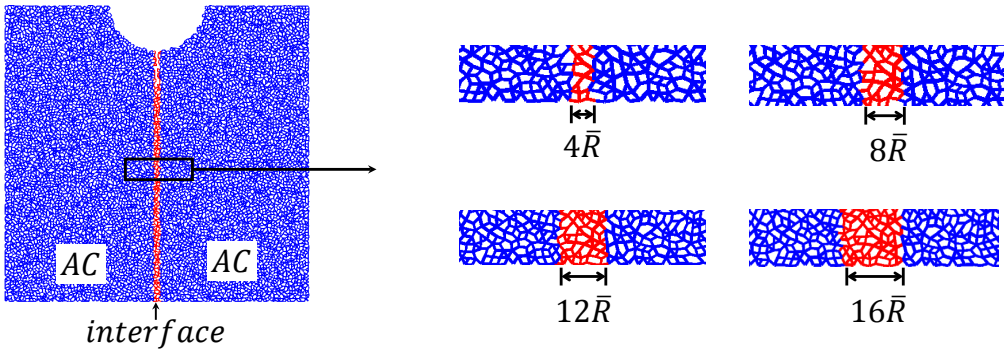

Figure 4.22: Definition of interface thickness in discrete element modelling.

between each component of the interface is not well defined as shown in [22]. In DEM, this dificulty is also present as shown in Figure 4.22 for 4 different approximative thicknesses w_i: $4\overline{R}$, $8\overline{R}$, $12\overline{R}$ and $16\overline{R}$. For an average particle radius $\overline{R} = 1\ mm$, one may get $4\ mm \leq 2 \times w_i \leq 12\ mm$.

By combination of Table 4.4 and Figure 4.23 and considering the effect of elasticity, one may observe that an increase on the thickness causes an inversely proportional decrease on the stiffness of the interface (see Section 4.4.3.1). The shape of the whole curve depends on this parameter since the energy release rate is kept constant (visible through an approximately constant area under the curve $F_h \times \delta_h$).

From Table 4.4, it can be seen that the energy release rate in IM decrease by 14% as the interface thickness increases from 2 layers to 8 layers, this also reflect

Table 4.4: IM Parameters to fit WST in DEM for different thickness.

	fitted items	$E_{int}\,(Pa)$	$\sigma_{int}((Pa))$	G_{int}	$E_i\,(Pa)$	$\Sigma_i(Pa)$	$G_i(N/m)$
a	$1 \times T$	5.5	1.4×10^4	1×10^6	1×10^6	6.5	1.62×10^4
b	$2 \times T$	5.5	1.4×10^4	1×10^6	0.5×10^6	6.5	1.55×10^4
c	$3 \times T$	5.5	1.4×10^4	1×10^6	0.33×10^6	6.5	1.47×10^4
d	$4 \times T$	5.5	1.4×10^4	1×10^6	0.25×10^6	6.5	1.42×10^4

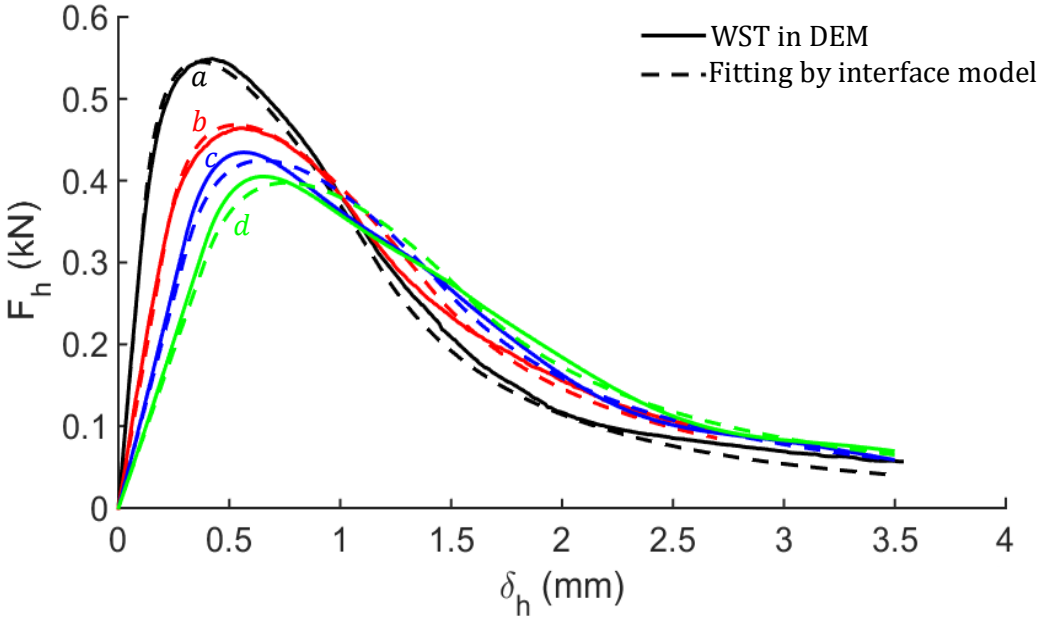

Figure 4.23: Force F_h as a function of the displacement δ_h for different interface thickness: a, $4\bar{R} = 4\,mm$; b, $8\bar{R} = 8\,mm$; a, $12\bar{R} = 12\,mm$; a, $16\bar{R} = 16\,mm$.

the limitation of IM to identify the mechanical properties due to the increase of interface thickness.

4.5 Interface behaviour under homogeneous conditions

The results of Section 4.4 suggest that the behaviour of relatively thin and flexible interfaces are governed by only 3 parameters: stiffness E_i/w_i, tensile strength Σ_i^t and energy release rate G_i. These parameters allows an interpretation of the interface at material scale, which may go beyond the wedge-splitting geometry.

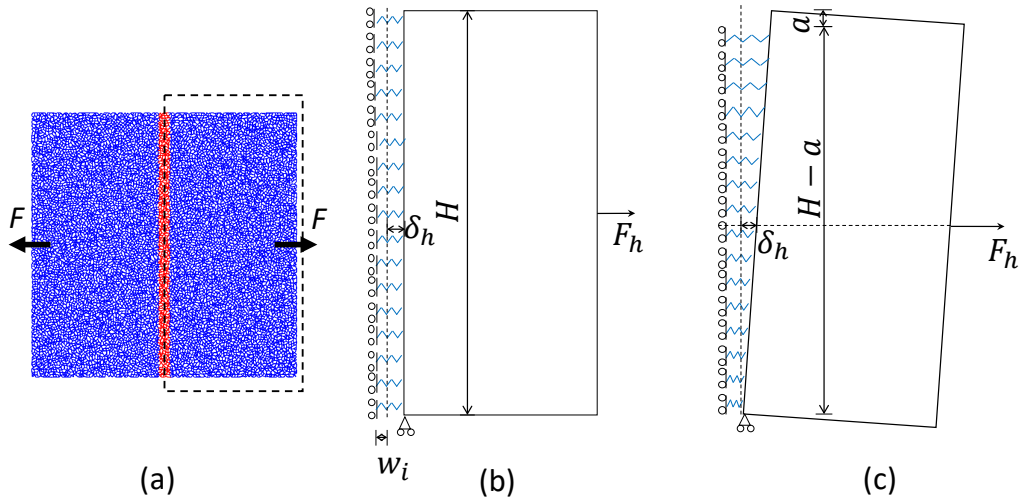

Figure 4.24: (a) Scheme of a direct interfacial tensile test. Kinematic of rupture (b) without and (c) with an initial crack.

Theoretically, interface wedge-splitting tests (WST) may be related to more simple direct tension test (DTT). In DDT, the geometry may present a similar geometry, but the application of the displacement δ_h and force F_h is modified and placed in the middle of the sample illustrated in Figure 4.24. Two possible kinematic for rupture are analysed: with and without an initial crack. Without a crack, the whole interface is loaded uniformly, which may induce in terms of modelling, the rupture of all springs in the same time. On the other hand, the existence of an initial crack a may induce an asymmetry on the distribution of efforts, which may be associated by the propagation of the crack during rupture.

DEM is able to reproduce a realistic kinematic of the rupture [97]. A test with 3 samples presenting identical properties and dimensions of the samples in Section 4.4.4 is adopted : $H = 220\,mm$, $a = 0\,mm$, $2 \times w_i = 4\overline{R} = 4\,mm$, $\overline{R} = 1\,mm$, $E_{ac} = 11\,GPa$, $E_{int} = 1 \times 10^6\,Pa$, $\Sigma^t_{ac} = 2 \times 10^6\,Pa$, $\Sigma^t_{int} = 14000\,Pa$, $G_{IC,ac} = 120\,N/m$, $G_{int} = 5\,N/m$. The tensile stress F_h/H as a function of the imposed displacement δ_h is presented on Figure 4.25.

Parallelly, the expected result for a perfectly homogeneous situation (no initial crack), where all the interface behaves uniformly, follows exactly the triangular shape of the spring force-displacement law as shown in Figure 4.25. One may observe that such interpretation overestimates the tensile strength and induces an unrealistic sharp rupture shape.

The material rupture under tension is usually triggered by the propagation of

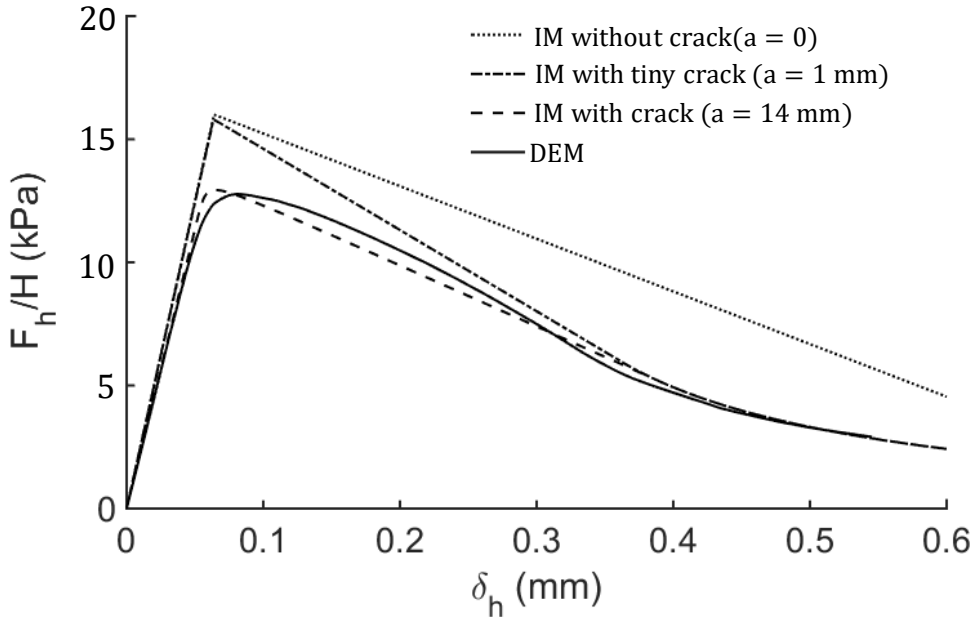

Figure 4.25: Tensile stress F_h/H as a funtion of the displacement δ_h. Effect of the initial crack a.

cracks at the boundaries of the geometry. The DTT with an infinitely small initial crack $a \to 0$ produces a more realistic rupture shape, less sharp, but keep overestimating the tensile strength Σ^t. An ideal fit is observed with an initial crack $a = 14\,mm$, which is about 7 times of the particle dimension $2 \times \overline{R} = 2\,mm$.

4.6 Application of the interface model on wedge-splitting experiments

In Section 4.4, the interface model (IM) is shown to be able to capture the main elements of the interfacial rupture behaviour identified from discrete element simulations. The next step is to apply the formulation of IM and analyse the experiments performed by M. Gharbi during her Ph.D. thesis [34].

4.6.1 Interface characteristics

The geometry of Gharbi's experiments are presented in Section 4.4.1. In her experiments, there are 3 sets of $6-10$ specimens: $P6$, $P7$, $P8$, corresponding to 3 different conditions. In all cases, the asphalt concrete and the fiber glass grids

are glued with a type of classical, cationic rapid-setting bitumen emulsion. Two types of fiber glass grids are used $100SB$ and $R100$, which are different in the production method and coating resin. The average results were taken from [34]. Table 4.5 summarizes the characteristics of the analysed results: height H, width W, initial crack size a, thickness t and grid type.

Table 4.5: Parameters of the wedge-splitting samples of Gharbi's experiments.

Samples	grid type	$H\,(mm)$	$a\,(mm)$	$W\,(mm)$	$t\,(mm)$
P6	100SB	242	54.6	198	151
P7	R100	233	54.6	186	151
P8	no grid	232	54.6	186	125

4.6.2 Analysis of the experiments

In Table 4.6, the parameters of the interface model (IM): stiffness E_i/w_i, strength Σ_i^t and Energy release rate G_i, identified from the fit of experiment curves of force F_h as a function of the displacement δ_h shown in Figure 4.26. The grid used in P7 is less stiff, has a lower strength with asphalt materials than P6. The grid of P6 presents a larger strength and energy release rate, which provides a guide on the construction with fiber grid. The fiber grid globally decreases the opening model strength and energy release rate, thus the glue material and glue method should be well considered in further application.

Table 4.6: Mechanical parameters of the interface model (IM) identified from Gharbi's experiments.

	$E_i/w_i\,(Pa/m)$	$\Sigma^t\,(Pa)$	$G_i\,(N/m)$
P6	0.75×10^9	0.85×10^5	155
P7	1.5×10^9	0.70×10^5	105
P8	0.75×10^9	1.20×10^5	220

4.7 Summary of the chapter

The mechanical properties of the interface between two asphalt concrete layers is studied by wedge-splitting tests (WST), in order to characterize the interface effect of the fiber glass and resin.

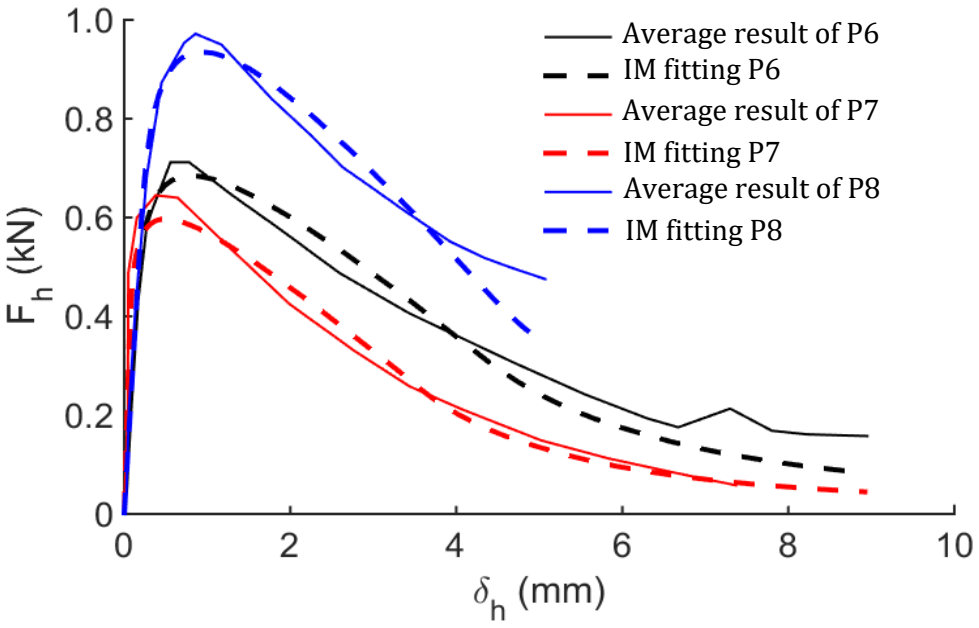

Figure 4.26: results of Experiments [34] and IM fitting.

A cohesive discrete element model is proposed to simulate materials with high energy release rate, like asphalt concrete, where monotonic rupture is associated to relatively large displacements. The fiberglass grid and the resin are assumed to act together mechanically which allowed interfacial WST to be simulated with a bi-material model.

Considering the lower stiffness and strength of the interface, the strain and the rupture appeared to be restricted to the interlayer interface as suggested by the experimental results. These elements were integrated in a simplified model where only 3 parameters of the interface were taken into account: stiffness, tensile strength and energy release rate. The interface model has shown to be totally compatible with the discrete element approach for ruptures caused by crack propagation. A comparison in direct tensile test between discrete element simulations and the interface model suggests that a length scale depending on the energy release rate, elasticity and strength must be considered to describe crack initiation.

A verification of the robustness of the interface model is presented in Appendix D where experimental WST of samples without any interface are analysed. The good agreement on the sample response and the corroboration of material parameters previously identified show the capacity of the approach on describing

localized crack propagation.

The confrontation of the models to experimental WST results has shown a very good agreement on the shape of the force response as function of imposed displacements. It allows a very simple quantitative analysis of the interface response. It has shown, for example, how much the strength and the fracture energy of the interface are weakened by the fiber glass grid. These values may be related furtherly to a design procedure for this type of reinforcement.

Chapter 5

Fatigue tests of asphalt concrete

Contents

5.1 Introduction

Traffic induces fatigue sollicitation of the pavement structure. Accurate prediction of the effect of a very large number of loading cycles ($10^5 - 10^6$) over the components of the pavements is a major requirement for the optimization of transport infrastructures. At laboratory scale, cyclic bending tests are intended to quantify deflection effects.

The main focus of this chapter is the analysis of the 4-point bending 4PB experiments performed by Arsenie during her PhD thesis [1], which are prequel of the ANR project. She was interested in quantifying the contribution of fibre glass grids to the fatigue life of asphalt concrete samples (described in Section 5.2). A damage model based on the PhD work of Didier Bodin [100] is implemented at the contact scale in a discrete element environment in Section 5.3.1. The first discrete simulations concern tension-compression tests and identify important features of the model (Section 5.4). In Section 5.5, the simulations of 4PB

tests are entirely described (geometry, boundary conditions, material behaviour and numerical strategy). A parametric study of the main elements of the numerical model is presented in Section 5.6, which is the basis for the calibration of the material parameters (Section 5.7). The effects of the glass fibre grids are introduced in Section 5.8, where two fundamental mechanisms are discussed: as reinforcements and as interfaces. After the investigation of the individual contributions of each of these two aspects, the combination of them is explored to analyze the experimental results. Finally, in Section 5.9, the conclusions of the chapter are summarized.

5.2 Experimental setup

During her thesis, Arsenie [1] performed 4-point bending (4PB) fatigue tests intending to quantify the contribution of the fiber glass grids on the fatigue life of asphalt concrete samples. This study was a prequel of the ANR project.

The geometry of the specimen is presented in Figure 5.1. The standard beam dimensions have been adapted in order to have three warp yarns in the width of the beam. Therefore, the standard beam dimensions have been increased in width, length and thickness. Each beam has a length $L = 630\,mm$, and a square cross section with height $h = 100\ mm$ and width $w = 100\ mm$. The beam is composed of 3 different layers by construction. The heights of the bottom, middle and upper layers are respectively $h/4$, $h/2$ and $h/4$. The layers are bonded with a bitumen emulsion. The specimens of experiments are separated into two categories: reinforced asphalt concrete and non-reinforced asphalt concrete. The fiber grids lay between the AC layers in the reinforced beams.

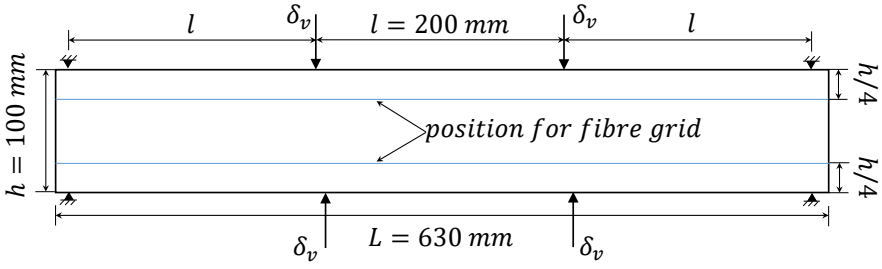

Figure 5.1: Geometry of specimen for 4PB test performed by Arsenie.

During the test, the specimens (Figure 5.2a) are placed inside the bending test machine shown in Figure 5.2b.

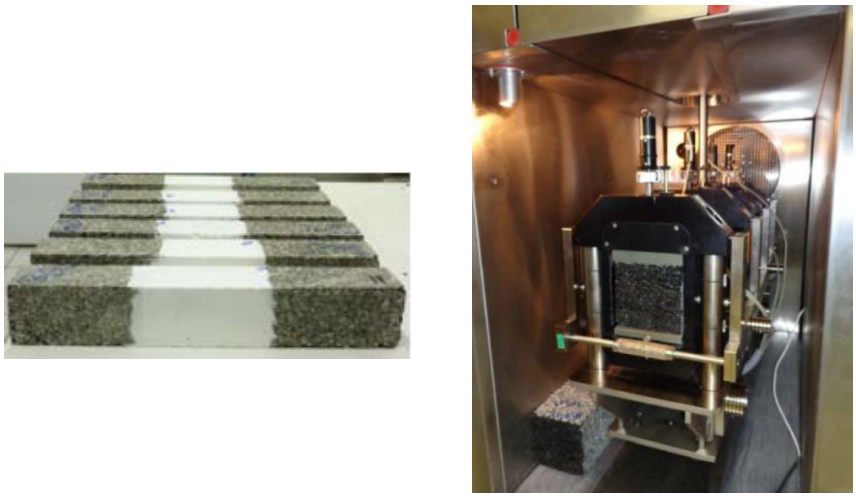

(a) (b)

Figure 5.2: (a) 4-point bending (4PB) samples and (b) loading equipment [1].

A controlled strain condition is applied by the sinusoidal motion of the central supports as described in Figure 5.3, which is the typical loading setup in fatigue of asphalt concrete [116,117]. The reaction force on the supports F_v also presents a sinusoidal response. The decrease of the amplitude of F_v as a function of the number of cycles N_C is the main information of a fatigue test.

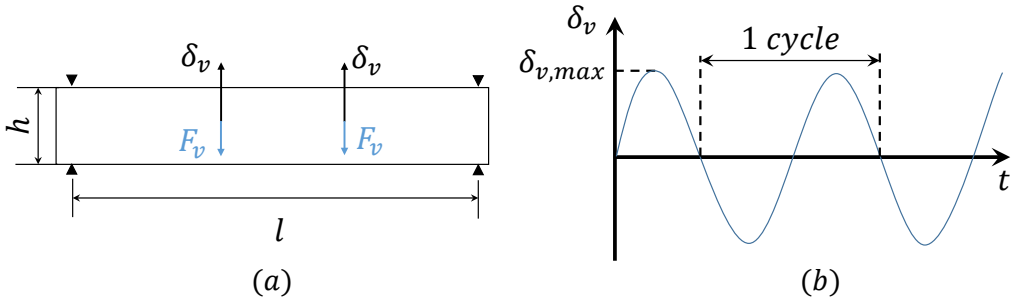

Figure 5.3: Loading setup of the 4-point bending (4PB) tests performed by Arsenie [1].

5.3 Fatigue model and discrete element implementation

As discussed in Section 2.7.2, the fatigue of asphalt concrete presents usually 3 phases. In the first cycles, a relatively fast and intense decrease on the macroscopic stiffness of the sample characterizes the phase I. A stable decrease is associated to phase II. In the last phase, a loss of the homogeneity of the strain in tension/compression fatigue test is observed in Bodin's thesis [100] followed by a very intense decrease of stiffness again.

In his thesis, Bodin [100, 118] proposed many damage laws, one of them is L3R with 4 parameters capable of capturing the whole trend of the stiffness evolution. Finite element damage calculations are usually sensitive to stress/strain concentration and are mesh dependent [119]. Bodin implemented a non-local version with finite element method to avoid these effects. Despite the satisfactory sample response obtained by his formulation, at the local level, excessively wide damaged regions are obtained.

In order to improve the local description of the damage phenomenon, and simplify the number of free parameters of the model, a law describing only the first two phases of the damage behaviour, called L2R [102, 118] (based on the Paas law [101]) is then adapted to a discrete element environment. The physical advantages of this approach are further discussed.

5.3.1 Local fatigue model - L2R

As defined in Section 2.7 and applied in Section 4.3.1, the damage D is a state variable which characterizes the material mechanical condition. Its value ranges from 0 to 1 ($D = 0$ indicates an intact material, whilst $D = 1$ defines its complete failure).

5.3.1.1 Equivalent strain $\widetilde{\varepsilon}$

In fatigue, the evolution of damage is originally controlled by the strain state of the material by a scalar equivalent strain $\widetilde{\varepsilon}$

$$\widetilde{\varepsilon} = \sqrt{\sum_{i=1}^{3} \left(\frac{\langle \sigma_i \rangle_+}{(1-D)E} \right)^2}, \tag{5.1}$$

where $\langle \sigma_i \rangle_+$ is the positive principle stress, and E is the Young's modulus of the material. In Equation 5.1, only tensile stress is considered to damage the material.

5.3.1.2 Rate of damage growth $\dot{D}$

The rate of damage growth $\dot{D}$ is defined as

$$\dot{D} = f(D)\widetilde{\varepsilon}^{\beta}\langle\dot{\widetilde{\varepsilon}}\rangle_+, \tag{5.2}$$

where $\langle\dot{\widetilde{\varepsilon}}\rangle_+$ is the positive value of the rate of increment of the local strain $\widetilde{\varepsilon}$ and β is a variable related to the fatigue slope $(-1-\beta)$ in log-log scale. $f(D)$ is a function of the damage factor, which was proposed by Paas [101] as

$$f(D) = CD^{\alpha}, \tag{5.3}$$

where α is a scalar parameter. According to Equation 5.2, only a positive increment of strain may induce damage.

5.3.1.3 Increment of damage δD per cycle

According to Equations 5.1 and 5.2, the damage is considered to be incremented only in tension and for positive strain rates. For a cyclic loading centred at zero, it represents the segments in Figure 5.4 for $N_C \times T \leq t \leq N_C \times T + T/4$, where N_C is the number of cycles and T is the period of the loading cycles.

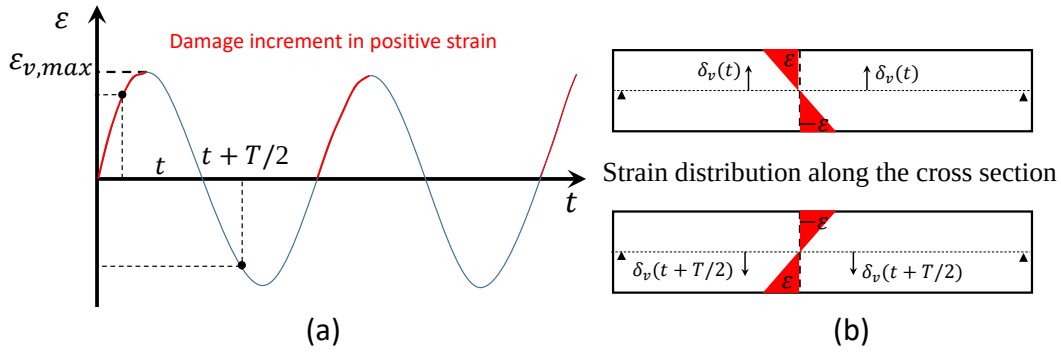

Figure 5.4: Loading cycle contribution on damage increment.

Equation 5.2 associated to Equation 5.3 can be rewritten as

$$\frac{\dot{D}}{D^{\alpha}} = C\widetilde{\varepsilon}^{\beta}\langle\dot{\widetilde{\varepsilon}}\rangle_{+}. \tag{5.4}$$

The evolution of the damage as a function of the number of cycles N_C can be obtained by integration of Equation 5.4 over the range of time $0 \leq t \leq N_C \times T$. The local strain $\widetilde{\varepsilon}$ induces damage increment only on the first quarter of the cycle. For constant strain cycles, the contribution of the strain integral is constant per cycle which allows the following simplification:

$$\int_0^{N_C\times T} \frac{\dot{D}}{D^{\alpha}}dt = \int_0^{N_C\times T} C\widetilde{\varepsilon}^{\beta}\langle\dot{\widetilde{\varepsilon}}\rangle_{+}dt = N_C\int_0^{T/4} C\widetilde{\varepsilon}^{\beta}\dot{\widetilde{\varepsilon}}dt, \tag{5.5}$$

where $\langle\dot{\widetilde{\varepsilon}}\rangle_{+} = \dot{\widetilde{\varepsilon}}$ for $0 \leq t \leq T/4$. The integration of Equation 5.5 leads to

$$\frac{D(N_C)^{1-\alpha}}{1-\alpha} = N_C\frac{C}{1+\beta}\widetilde{\varepsilon}(T/4)^{1+\beta} = N_C\frac{C}{1+\beta}\varepsilon_a^{1+\beta}, \tag{5.6}$$

where $D(N_C)$ is the damage at $t = N_C \times T$ and $\widetilde{\varepsilon}(T/4)$ corresponds to the amplitude ε_a of the local strain for a sinusoidal cycle.

For the particular case where the amplitude of the strain remains constant during all the number of cycles N_C, the damage value can be isolated from Equation 5.6

$$D(N_C) = \left(\frac{C\,(1-\alpha)}{1+\beta}\varepsilon_a^{1+\beta}N_C\right)^{\dfrac{1}{1-\alpha}}. \tag{5.7}$$

A more general incremental calculation of the damage can be obtained by derivation of Equation 5.6 with respect to the number of cycles N_C

$$\frac{\delta D}{\delta N_C} = D^{\alpha}\frac{C}{1+\beta}\varepsilon_a^{1+\beta} \tag{5.8}$$

The main advantage of Equation 5.8 is to take into account the evolution of the amplitude ε_a during the fatigue test automatically. However, the value of damage D must be initialized ($D \neq 0$). This initial value $D(1)$ can be easily obtained from Equation 5.7 for $N_C = 1$ in the first cycle.

$$D(1) = \left(\frac{C\,(1-\alpha)}{1+\beta}\varepsilon_a^{1+\beta}\right)^{\dfrac{1}{1-\alpha}}. \tag{5.9}$$

5.3.2 DEM implementation of the fatigue model

5.3.2.1 Local equivalent strain

The behaviour for one contact can be reduced to a unidimensional problem. As defined in Section 3.2, the displacements in the direction of the contact resultant force δ (Equation 4.8) may give rise to the definition of the strain ε if associated to the length separating two particles i and j in contact $R_i + R_j$:

$$\widetilde{\varepsilon} = \varepsilon = \frac{\delta_n sin\theta + \delta_s cos\theta}{R_i + R_j}. \tag{5.10}$$

where δ_n and δ_s are the normal and tangential relative displacements at the contact, as previously defined. The angle θ indicates the direction of the contact force with respect to the tangential direction. The strain defined for a contact in Equation 5.10 represents the local equivalent strain defined in Equation 5.1 for a continuum material.

The amplitude of the local strain is consequently the maximum value of the local strain under cyclic loading $\varepsilon_a = \max(\varepsilon)$.

5.3.2.2 Damage and force calculation

In the first cycle, the damage factor D is initialized, being calculated for each contact by Equation 5.9. At each new cycle, D is modified incrementaly, based on a first order solution of Equation 5.8 as

$$D(N_c + \Delta N_C) = D(N_c) + \Delta N_C \left(D^{\alpha} \frac{C}{1+\beta} \varepsilon_a^{1+\beta} \right), \tag{5.11}$$

where ΔN_C is the cycle increment parameter. Any value of $\Delta N_C > 1$ allows a gain of calculation time, but it must be carefully chosen not to induce cumulative errors.

After the damage identification, the forces can be updated following the same procedure of Chapter 4 (see Equation 4.6)

$$\begin{aligned} f_n &= k_n \left(1 - D\right) \delta_n \\ f_s &= k_s \left(1 - D\right) \delta_s, \end{aligned} \tag{5.12}$$

where k_n and k_s are the normal and tangential stiffness of the intact contacts, respectively.

5.3.2.3 Structures under centred loading - static loading hypothesis

The laboratory fatigue tests [1] are usually driven by imposed displacements, which helps to capture the last phase of fatigue when the sample stiffness tends to be very low. The displacements are sinusoidal like, with controlled amplitude and frequency. The samples are symmetric, which associated to the loading setup guarantees that strains (and stresses) are also sinusoidal centred at zero, avoiding creep contributions. In these conditions, positive and negative strain values with the same intensity are separated in time of half period T ($\varepsilon(t) = -\varepsilon(t + T/2)$) in the whole samples, as shown in Figure 5.5.

The damage induced by fatigue is defined by the amplitude of the local strain ε_a at each contact. Due to the symmetry of the loading it can be obtained equally for one cycle as

$$\varepsilon_a = max(\varepsilon(t)) = -min(\varepsilon(t)). \tag{5.13}$$

In the present formulation, the viscosity of the material is not being taken into account, which means that stress and strain are in phase. In other words, the extreme values of stress (or forces) coincide with extreme values of strain (or displacements). On these conditions, all necessary elements to calculate the increment of damage per cycle can be obtained with static boundary conditions, representing the maximum amplitude of the cyclic load. The intensity of the measured forces represents naturally the amplitude of the cyclic forces which may be obtained during cyclic global load.

Under static global loading, the amplitude of the local strain ε_a for each contact is calculated by the absolute value of the local strain ε

$$\varepsilon_a = |\varepsilon|. \tag{5.14}$$

In this way, even the contacts under compression, in case of bending tests, inform the value of ε_a which may damage the material under tension. The static loading hypothesis allows a considerable gain in time calculation without any loss of generality.

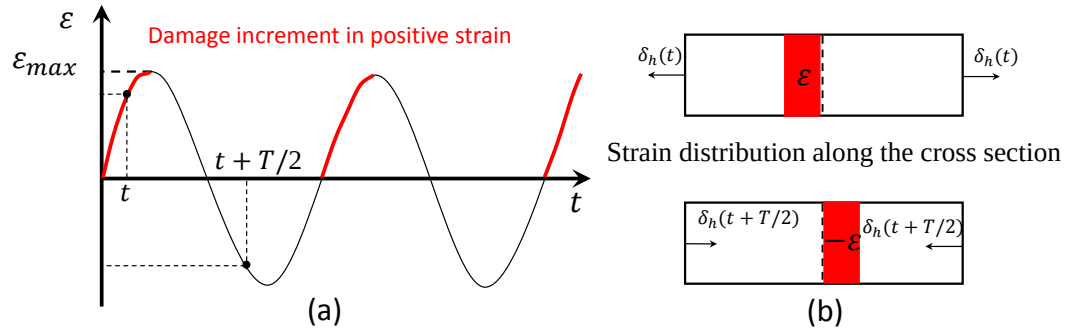

Figure 5.5: (a) Cycles of strain in tension/compression and bending tests, and (b) corresponding strain distribution.

5.3.2.4 Numerical scheme

The scheme of the contact law algorithm adopted in DEM simulations for each timestep is presented in Figure 5.6. The damage factor D is initially set as zero for all the contacts, which represents the intact state of the material. In the first cycle ($N_C = 1$), after the calculation of the local strain ε (Equation 5.10) for each contact, the value of D is initialized, being calculated by Equation 5.9. For all other cycles ($N_C > 1$), the damage is calculated by Equation 5.11.

An extra variable is added to each contact to *switch* (on or off) the damage calculation. If by any reason, the damage calculation should be deactivated, then $switch = 1$ and D remains unchanged. That is the case when the damage reaches its maximum value $D = 1$, for example. While $switch = 0$, the damage is incremented following the described procedure.

After the determination of D, the contact forces are simply calculated by Equation 5.12.

The fatigue model, as part of the contact constitutive model, is written and compiled in C++ language using 'visual studio 2010'. For more detailed description on the software refer to [120]. The generated file is then called by PFC as the *contact law* at each timestep during simulations.

5.4 Cyclic tension-compression simulations

The response of fatigue law *L2R* implemented as a contact law in discrete element simulations is verified under homogeneous boundary condition.

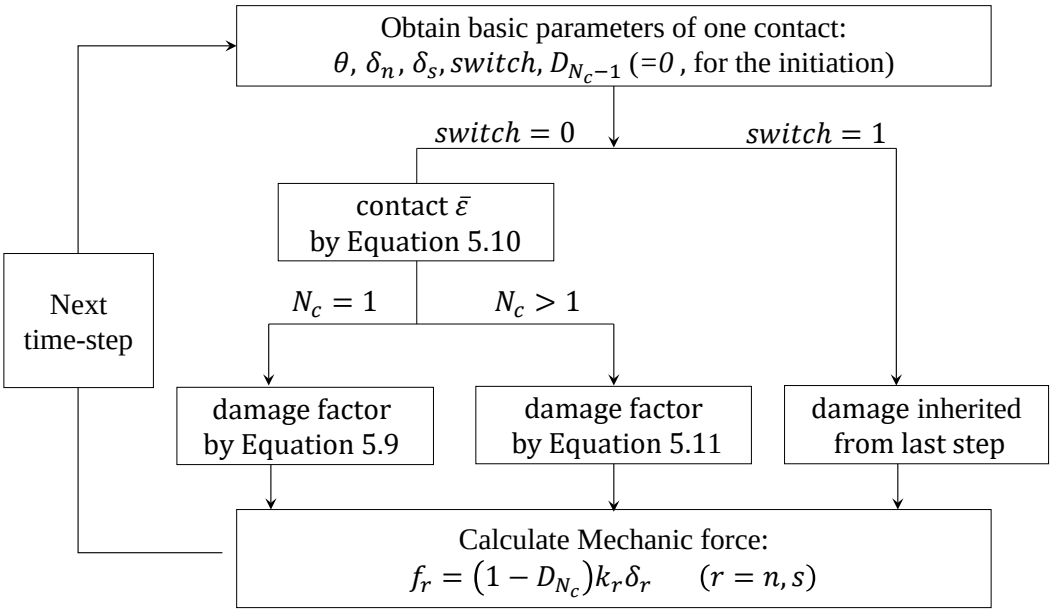

Figure 5.6: Algorithm for damage calculation in DEM.

Three rectangular samples are generated as shown in Figure 5.7a. The discrete element parameters for the 3 assembles are: average particle radius $\overline{R} = 2\,mm$, particle size ratio $R_{max}/R_{min} = 1.6$, contact modulus $E_{cmod} = 2.0 \times 10^{10}\,Pa$ and stiffness ratio $k_{ratio} = 4.5$. These choices correspond to the following material properties: Young's modulus $E = 11\,GPa$ and Poisson's ratio $\nu = 0.34$.

A uniform relative displacement $\delta_{h,\,max} = 0.048\ mm$ is applied at the boundaries in order to reproduce the effect of the cyclic loading $\delta_h(t)$ presented in Figure 5.7b. The imposed displacements induce a macroscopic strain with amplitude $\delta_{h\ max}/L = 150\,\mu m/m$, which corresponds to the maximum strain level in standards. The imposed displacements induce a total force $F_{h,\,max}$ which is measured at each new cycle.

The contact parameters adopted in the simulations are $\alpha = -2.0$, $\beta = 3.0$ and $C = 1 \times 10^9$. In Figure 5.8a, one may observe the stiffness factor of a contact submitted to a strain $\varepsilon_a = 150\,\mu m/m$, $F/F_0 = 1 - D$ associated to the contact law L2R (Equation 5.7). In parallel, the response F_h/F_{h0} of the 3 samples as functions of the number of cycles N_C is shown in Figure 5.8b. One may observe that $L2R$ is individually adapted to describe only 2 regimes (phases I and II from fatigue regime, see Section 2.8.3.1). However, the sample response, which depends on the contribution of multiple contacts, describe clearly the 3 phases.

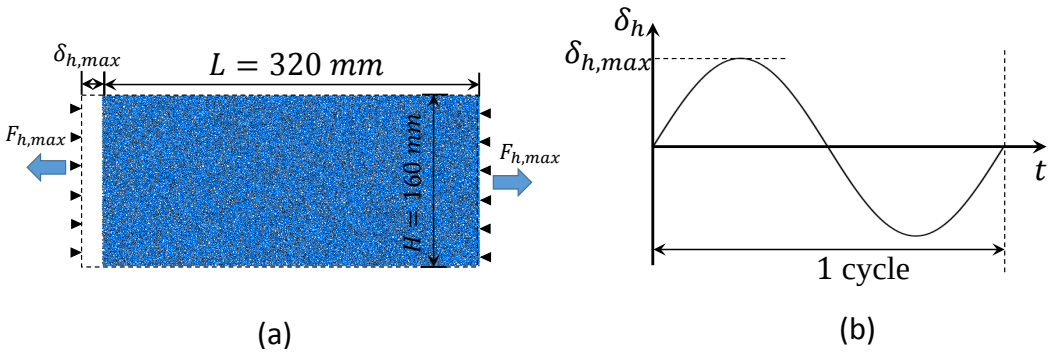

Figure 5.7: (a) Sample dimensions and imposed displacements. (b) Analysed cyclic loading.

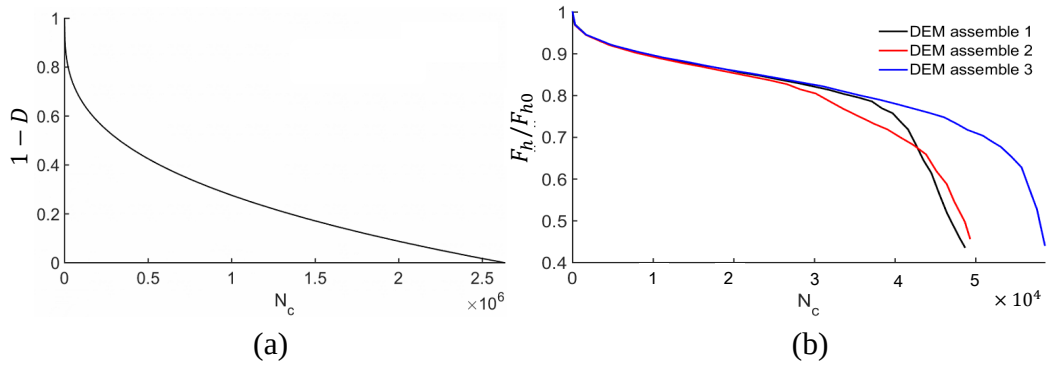

Figure 5.8: (a) Stiffness factor $(1-D)$ associated to contact law L2R. (b) Stiffness factor F_h/F_{h0} of the 3 samples in tension/compression.

The damage maps of sample 1 in multiples stages (Figure 5.9) give a better understanding of the rupture process in fatigue. The comparison of the intact initial stage (Figure 5.9a) and the approximated end of phase II at $N_C = 4.16 \times 10^4$ (Figure 5.9b) shows that a diffused damage dominates the loss of stiffness of the sample. The progression of localized damage zones seems to dominate phase III as shown in Figure 5.9c for $N_C = 4.90 \times 10^4$, which conducts to a loss of homogeneity of the stress and strain distribution inside the material and a localization of high level damage at the right of the sample. The simulation results suggest that phase III is the consequence of a structural effect beyond a material behaviour.

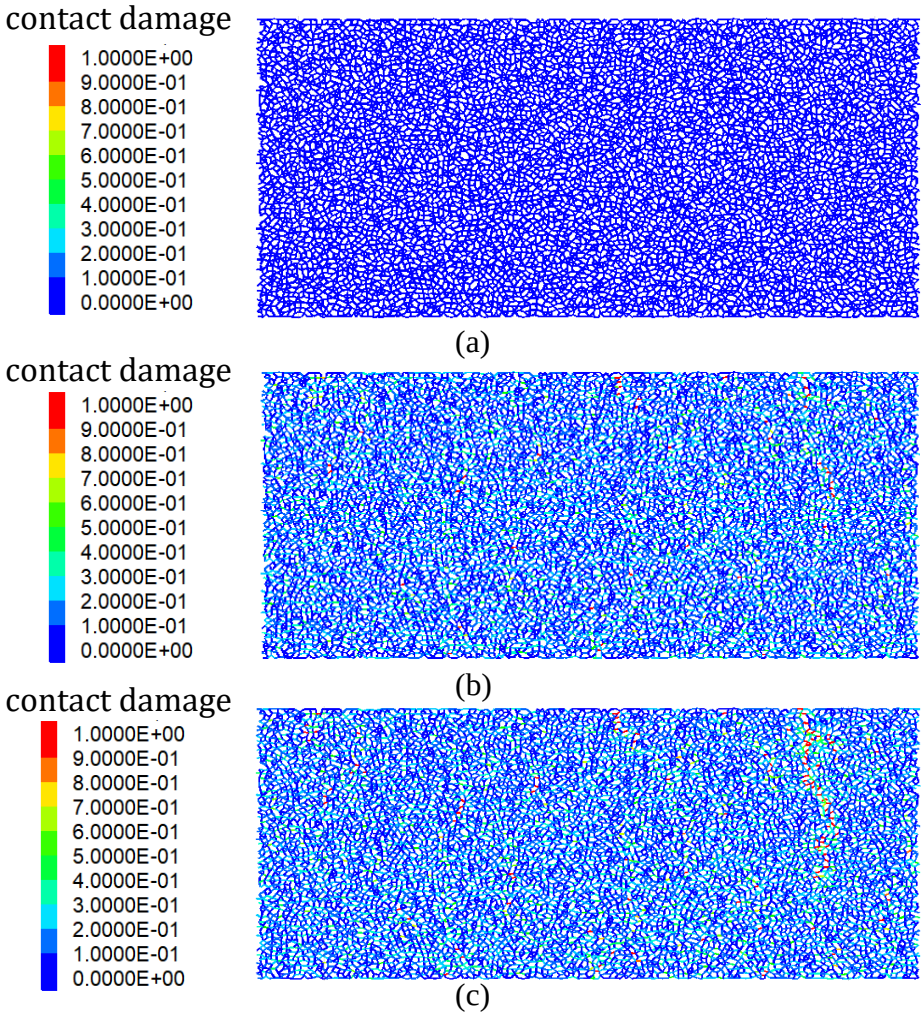

Figure 5.9: (a) Damage map of sample 1 before the test, (b) at cycle $N_C = 4.16 \times 10^4$ and (c) at the end of the fatigue test ($N_C = 4.90 \times 10^4$).

5.5 Cyclic 4-point bending (4PB) tests

5.5.1 Geometry and boundary conditions

4-point bending (4PB) tests are simulated by discrete element method (DEM). The geometry follows the dimensions of the experiments perfomed by [1] (see Section 5.2) as indicated in Figure 5.10a with length $L = 630\ mm$, height $h = 100\ mm$ and an equal spacing between supports $l = 200\ mm$.

The real supports of the beam work only in compression, which means that different positions of the beam are solicited depending on the signal of the imposed

displacements. To avoid this asymmetry of the load, the supports are modelled by a vertical range of particles with length $10\,mm$ in the horizontal axis of the beam. The range of particles is long enough to distribute the effort and short enough to avoid bending moment over the supports. The reduced dimension of the supports induces a concentration of efforts which may lead to an accelerated damage of the structure. This inappropriate behaviour is avoided by the deactivation of the damage calculation inside a rectangular zone ($10\,mm \times 15\,mm$) around the supports and symmetric around the neutral axis, which is large enough to prevent the damage around the supports and small enough to have no influence on the damage evolution of other parts of the sample. This unrealistic (but theoretically ideal) choice has the advantage of keeping the symmetry of the structure during cyclic loading. Furthermore, concerning the material behaviour, $L2R$ is a fatigue law adapted to centred tension/compression. Only compressive loading may be outside the bounds of the theoretical approach. The deactivation of the damage in the center of the beam does not lead to discontinuities of the damage field since this region is weakly solicited and naturally presents a very low damage.

Experimentally, supports 1 and 2 do not move, whilst supports 3 and 4 are driven by a cyclic centred displacement with a given amplitude $\delta_{v,\ max}$. As discussed in Section 5.3.2.3, these loading conditions are modelled by a static imposed displacement $\delta_{v,\ max}$ of the central supports. The maximum normal strain level ε_{max} is observed in the middle section of the beam in upper and bottom positions and can be calculated by the expression [1]

$$\delta_{v,max} = \frac{5}{3}\frac{A^2}{h}\varepsilon_{max}, \tag{5.15}$$

where $A = 200\,mm$ is the distance between two adjacent supports.

A vertical force F_v is measured as support reaction and evolves during the fatigue tests.

5.5.2 Verification of damage process under symmetric loading

In Section 5.3.2.3, the damage process of structures under centred loading can be simulated by static loading, with the assumption that contacts no matter in compression or tension reach the amplitude at the same time as the global cyclic load. Thus in this section, the damage process under static load is verified by

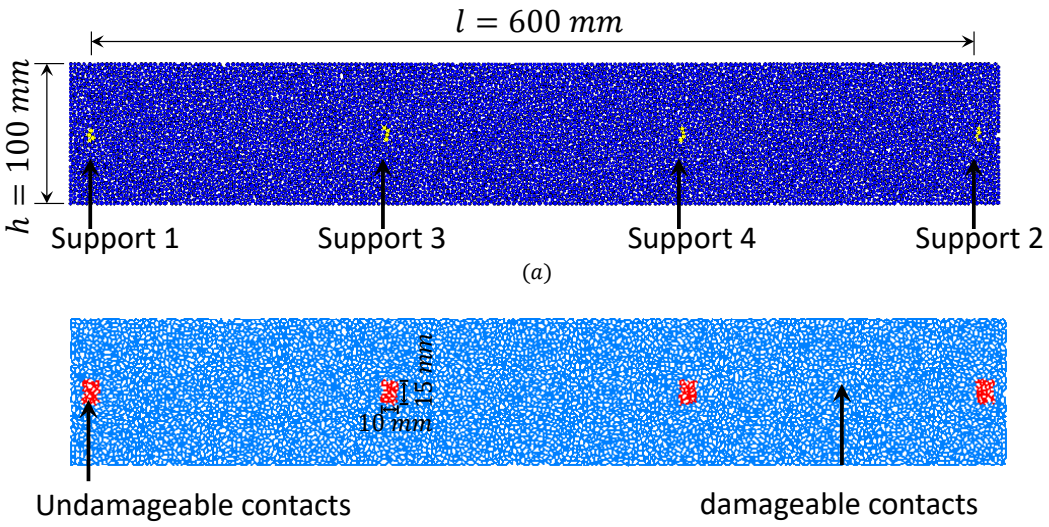

Figure 5.10: Geometry of the 4-point bending (4PB) samples in DEM. (a) Indication of the dimensions over the particle packing and (b) contact properties by zones.

4PB fatigue simulations with positive and negative displacements, respectively $+\delta_{v,\ max}$ and $-\delta_{v,\ max}$.

The sample presents 8282 particles with average radius $\overline{R} = 2.9\,mm$ and particle size ratio $R_{max}/R_{min} = 1.6$. The parameters of fatigue model are $C = 10^9$, $\alpha = -2.0$ and $\beta = 3.0$.

The applied displacements ($\delta_{v,\ max} = \pm 0.1\,mm$) correspond to the strain level $\varepsilon_{max} = 150\,\mu m/m$ (Equation 5.15) in Arsenie's experiments.

The responses of the sample in terms of stiffness factor F_v/F_{v0} as function of the number of cycles N_C for each loading case are presented in Figure 5.11. Precisely the same curves are obtained even for very high level of damage.

The same local effective strain ε (Equation 5.10), shown in Figure 5.12, is observed in absolute value ignoring the signal of $\delta_{v,\ max}$. This result is expected due to the identical behaviour of the contacts in tension and compression, even after the total damage of the contacts. The localized damage zones behave as cracks which cannot be closed and present a compressive response.

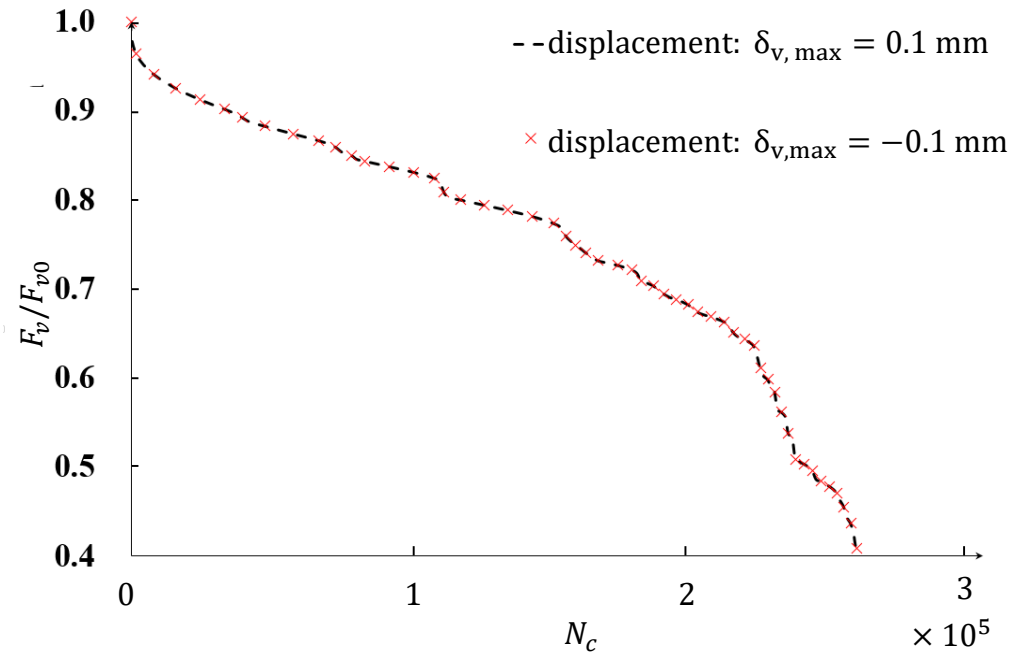

Figure 5.11: Stiffness factor F_v/F_{v0} as a function of the number of cycles N_C for $\delta_{v,\,max} = 0.1\ mm$ and $\delta_{v,\,max} = -0.1\ mm$.

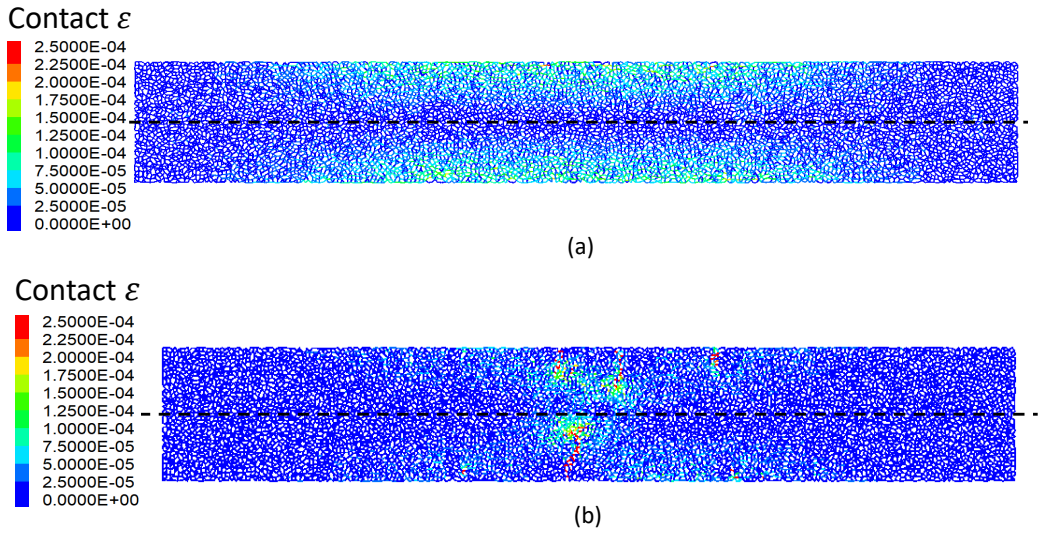

Figure 5.12: The effective strain distribution for $\delta_{v,\,max} = 0.1\ mm$ and $\delta_{v,\,max} = -0.1\ mm$ for a number of cycles (a) $F_v/F_{v0} = 1.0$ and (b) $F_v/F_{v0} = 0.4$.

5.6 Parametric study of the fatigue model

A complete understanding of the effect of each parameter of the fatigue law (C, α, β and the cycle increment ΔN_C) is fundamental to further analyse the experimental results. The study focuses on the stiffness factor F_v/F_{v0} during the fatigue test.

In the discrete element model, the following parameters are adopted: an average radius $\overline{R} = 2.9\ mm$, size ratio $R_{max}/R_{min} = 1.6$, contact modulus $E_{cmod} = 2.0 \times 10^{10}\,Pa$, stiffness ratio $k_r = 4.5$. They correspond to a Young's modulus $E = 11\,GPa$ and Poisson's ratio $\nu = 0.34$.

When not indicated differently, the following parameters are taken for the fatigue contact law: $C = 1 \times 10^9$, $\alpha = -2$ and $\beta = 3.0$; a vertical displacement $\delta_v = 100\,\mu m$, which is associated to a maximum normal strain $\varepsilon_{max} = 150\,\mu m/m$, and a cycle increment $\Delta N_C = 100$ is adopted.

5.6.1 Effect of ΔN_C and C

5.6.1.1 Effect of ΔN_C

The damage D is calculated incrementally with a cycle increment ΔN_C. The evolution of D with the number of cycles N_C is generally very slow, which opens the possibility of numerically 'jump' cycles (instead of performing one by one). The stiffness factor F_v/F_{v0} as a function of the number of cycles N_C for different increments of cycles $\Delta N_C = 100,\ 1000,\ 2000,\ 4000$ is presented in Figure 5.13a. Higher values of ΔN_C increases the propagation of errors during calculations of D, which explain the deviation of the results. A stable result is however observed for $\Delta N_C < 1000$.

5.6.1.2 Effect of parameter C

As it can be seen in Equation 5.7, under constant strain, the parameter C has an effect of multiplying the number of cycles N_C. In Figure 5.13b, the results of simulations with different C are presented ($C_1 = 1 \times 10^9, C_2 = 1 \times 10^{10}, C_3 = 2 \times 10^{10}$ and $C_4 = 4 \times 10^{10}$).

5.6.1.3 Relation between the parameters ΔN_C and C

According to Equation 5.11, the parameter C has a linear scaling effect on the increase of the damage. It can be observed by the collapse of the stiffness factor

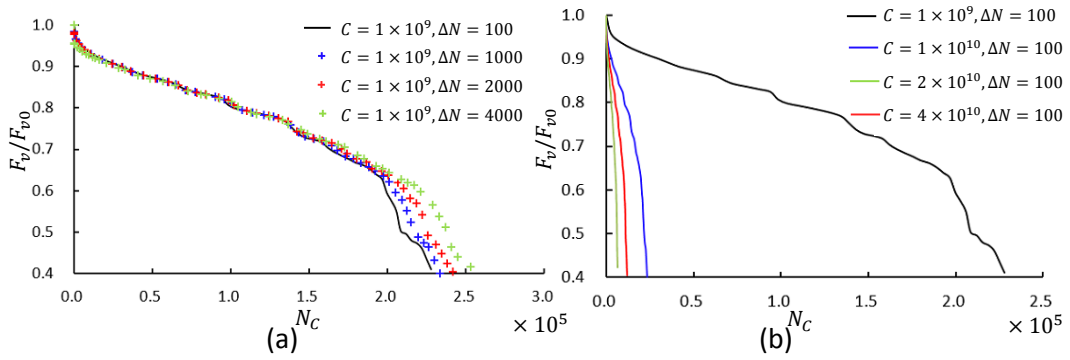

Figure 5.13: Stiffness factor F_v/F_{v0} as a function of the number of cycles N_C for (a) different increment of cycles ΔN_C and (b) different value of parameter C.

F_v/F_{v0} as a function of the product between the number of cycles and parameter C ($N_C \times C$) in Figure 5.14a. This collapse is not absolute, because of the accumulation of truncation errors which is intrinsic to the step by step integration of the damage variable in Equation 5.11. A biggest deviation can be observed at the end of the fatigue life, where locally the damage variable presents its highest evolution and consequently more integration errors.

The propagation of errors depends on the value C which scales the damage increment and also the cycle increment ΔN_C. As it can be seen in Figure 5.14b, the scaled fatigue curves (F_v/F_{v0} versus $N_C \times C$) are identical for equal values of the factor $N_C \times C$. It means globally that a faster damage evolution (associated, for example, to a higher value of C) demands a smaller value of ΔN_C for an equal level of precision. On the other hand, a structure composed by a material which presents a slow damage increase per cycle could be calculated with higher values of ΔN_C, which may represent a computational gain of time.

5.6.2 Effect of the parameter α

As shown by Bodin [100], under constant strain, α has a stronger effect in the beginning of the damage process, as shown in Figure 5.15a for different values of $\alpha = -1.0, -1.5, -2.0$ and -2.5. An indicative frontier between phase I and II can be represented, where the effect of α is concentrated in phase I. An approximative proportionality between the curves can be visualized with a normalization of the number of cycles by the corresponding value for a given value of $1 - D$. For

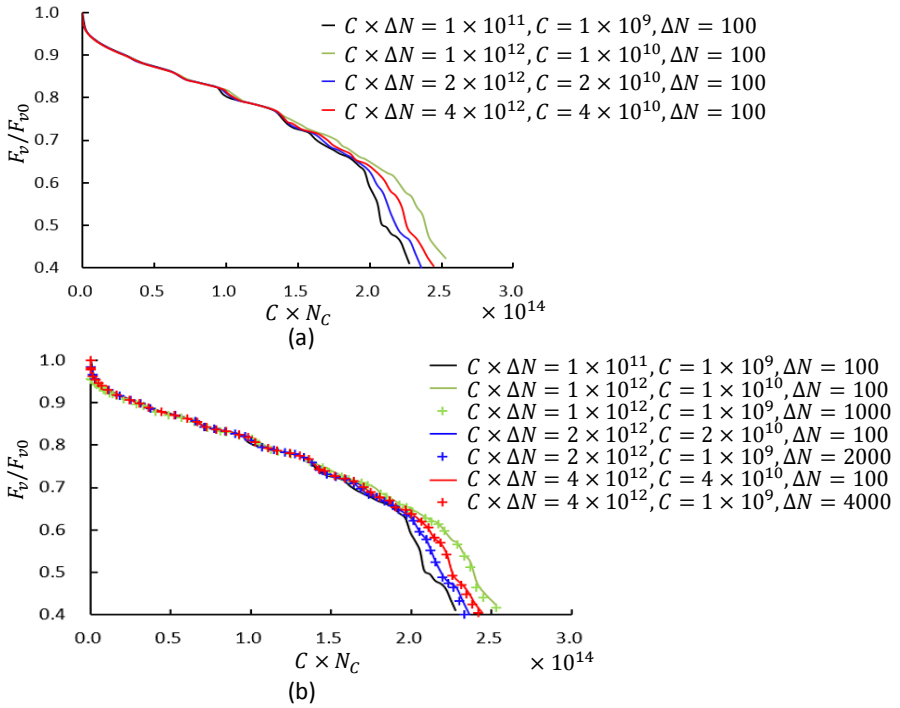

Figure 5.14: Stiffness factor F_v/F_{v0} as a function of the $C \times N_C$ for (a) different values of C, $\Delta N_C = 100$ and (b) different values of $C \times \Delta N_C$.

example, the normalized number of cycles can be defined as

$$N_{c,norm} = \frac{N_c}{N_{c,\,0.4}}, \tag{5.16}$$

where $N_{c,\,0.4}$ is the number of cycles associated to a stiffness fraction of $1-D = 0.4$.

In DEM, the heterogeneous strain conditions affects the damage evolution, which consequently is reflected on the stiffness fraction evolution, as shown in Figure 5.16a for 4PB simulations. The same results as a function of the number of cycles $N_{c,norm}$ normalized by Equation 5.16 show the absence of proportionality, revealing a global effect of α during the whole damage process, but more concentrated in the first phase.

5.6.3 Effect of the parameter β

Under constant strain ε_a, the parameter β is linked to the slope (equals to $-1-\beta$) of the S-N curve in log-log diagram, and it is directly deduced from the experimental tests of fatigue. Therefore, it has a strong effect on the stiffness fraction $1 - D$ as function of the number of cycles N_C as shown in Figure 5.17a for

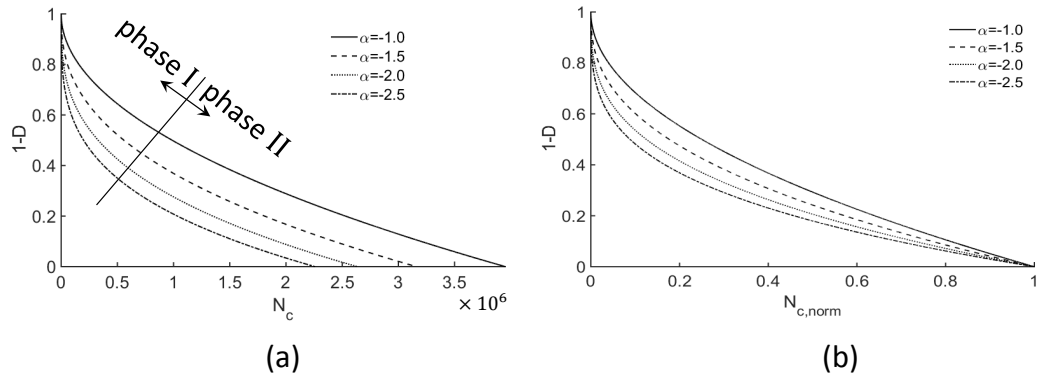

Figure 5.15: Stiffness factor $1-D$ for constant strain $\varepsilon_a = 1 \times 10^{-4}$ and different values of α (a) as a function of the number of cycles N_C and (b) as a function of the normalized number of cycles $N_{C,norm}$.

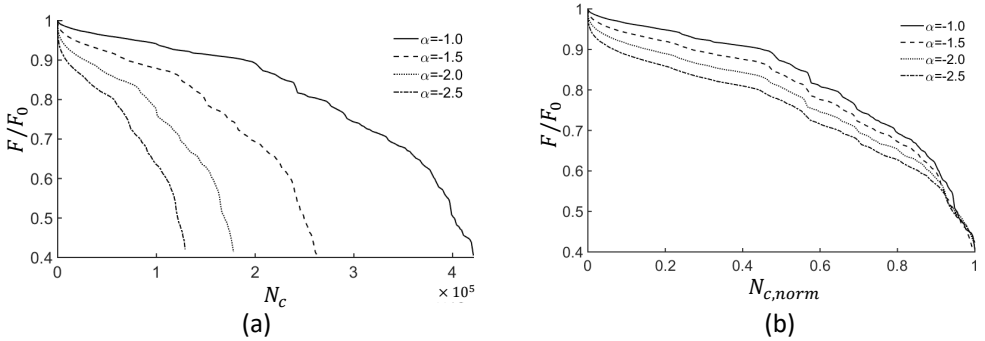

Figure 5.16: Stiffness fraction F_v/F_{v0} (a) as function of the number of cycles N_C and (b) as a function of the normalized number of cycles $N_{c,norm}$ for different values of α.

β = 2.8, 3.0, 3.2 and 3.4. The values of $1-D$ can be related to $N_{c,norm}$ as a single curve, as described in Figure 5.17b.

For the same values of the parameter β, the results of the stiffness fraction F_v/F_{v0} as function of the number of cycles N_C for 4PB tests (see Figure 5.18) show a similar trend as previously observed concerning the effect of β under constant strain ε_a: higher values of β induce a bigger fatigue life. The non proportionality between the curves of F_v/F_{v0} versus $N_{c,norm}$ reveals the complex effect of the parameter β, which compared to the effect of α, affects more the phase II of the fatigue behaviour.

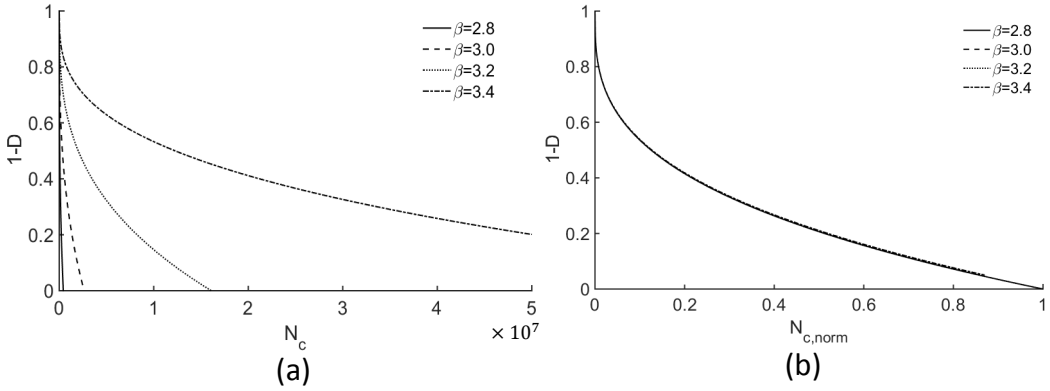

Figure 5.17: Stiffness factor $1-D$ for constant strain $\varepsilon_a = 1 \times 10^{-4}$ and different values of β (a) as a function of the number of cycles N_C and (b) as a function of the $N_{c,norm}$.

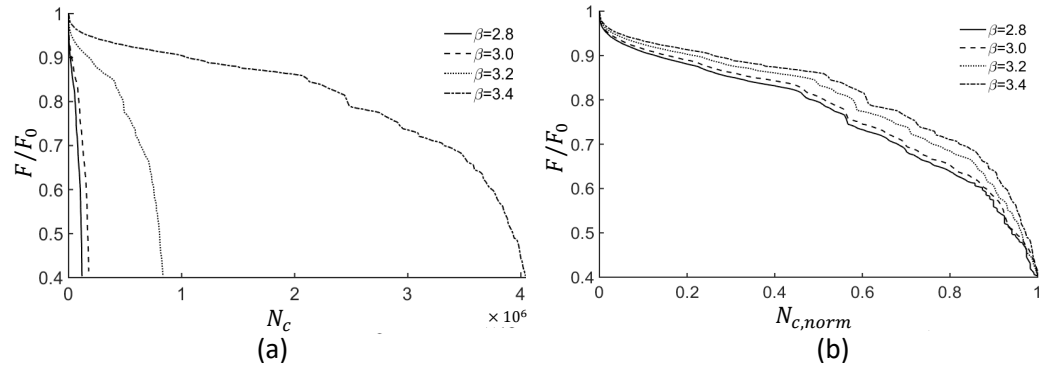

Figure 5.18: Stiffness factor F_v/F_{v0} (a) as a function of the number of cycles N_C and (b) as a function of the $N_{c,norm}$ for different values of β.

5.6.4 Effect of the strain scale ε_{max}

The effect of the strain level on the stiffness fraction $(1-D)$ under constant strain is shown in Figure 5.19a for different strain values $\varepsilon_a = 110\,\mu m/m$, $130\,\mu m/m$ and $150\,\mu m/m$. As indicated in Equation 5.7, the strain scales the effect of the number of cycles like the parameter C by the factor $\varepsilon_a^{1+\beta}$. A single curve is then obtained for the evolution of $1-D$ as a function of $\varepsilon_a^{1+\beta} N_C$ as shown in Figure 5.19b.

A similar effect of the strain level is observed for 4PB tests in Figure 5.20a. Different values of the maximum strain ε_{max} are adopted: $\varepsilon_{max} = 150\,\mu m/m$, which correspond to the following amplitudes of the support displacements $\delta_v = 100\,\mu m$. Despite the heterogeneity of the stress/strain fields, the normalization of the num-

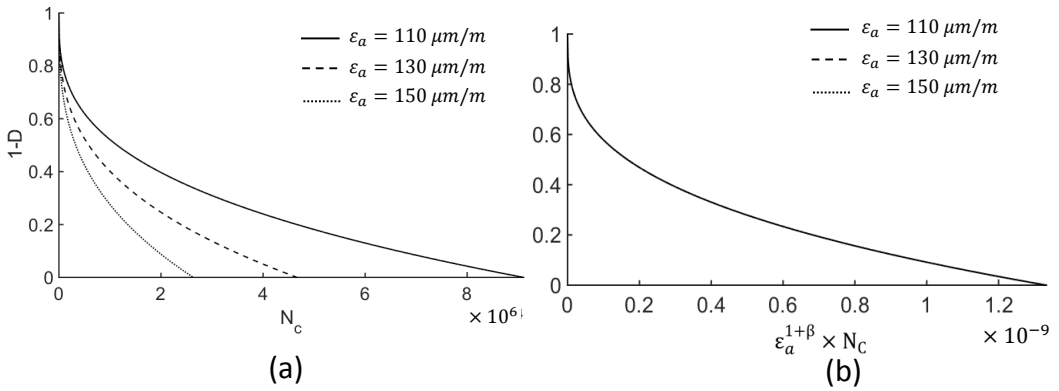

Figure 5.19: Stiffness factor $1-D$ for constant strain amplitude ε_a. The different curves indicate different values of $\varepsilon_a = 110\,\mu m/m,\ 130\,\mu m/m,\ 150\,\mu m/m$. (a) as a function of the number of cycles N_C and (b) as a function of the $\varepsilon_a^{1+\beta} N_C$.

ber of cycles by the factor $\varepsilon_a^{1+\beta}$ is shown to be consistent (see Figure 5.20b). This information is very important concerning the identification of the parameter β which physically relates the effect of the strain in different tests.

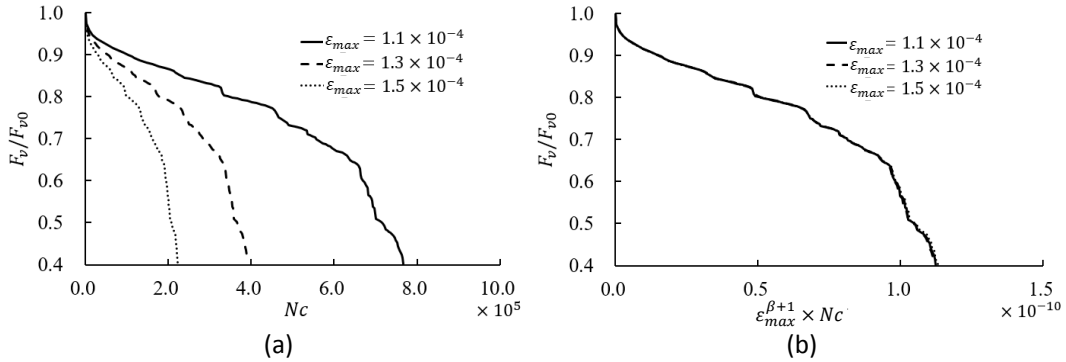

Figure 5.20: Stiffness fraction F_v/F_{v0} (a) as a function of the number of cycles N_C and (b) as a function of the $\varepsilon_{max}^{1+\beta} N_C$ for different values of ε_{max}.

This scale effect associated to the strain level ε_{max} and β indicates that damage distribution itself is independent on the strain scale. It may affect only the number of cycles associated to its evolution. In Figure 5.21 this effect can be visualized for two identical damage maps obtained in two different 4PB simulations with different values of strain amplitude: $\varepsilon_{max\ 1} = 115\ \mu m/m$ and $\varepsilon_{max\ 2} = 150\ \mu m/m$. The maps are registered for the same stiffness fraction $F_v/F_{v0} = 0.4$ but different number of cycles $N_{C\ 1} = 739703$ and $N_{C\ 2} = 256523$, respectively associated to $\varepsilon_{max\ 1}$ and $\varepsilon_{max\ 2}$. The strain and the number of cycles satisfy the relation: $\varepsilon_{max\ 1}^{1+\beta} N_{C\ 1} = \varepsilon_{max\ 2}^{1+\beta} N_{C\ 2}$.

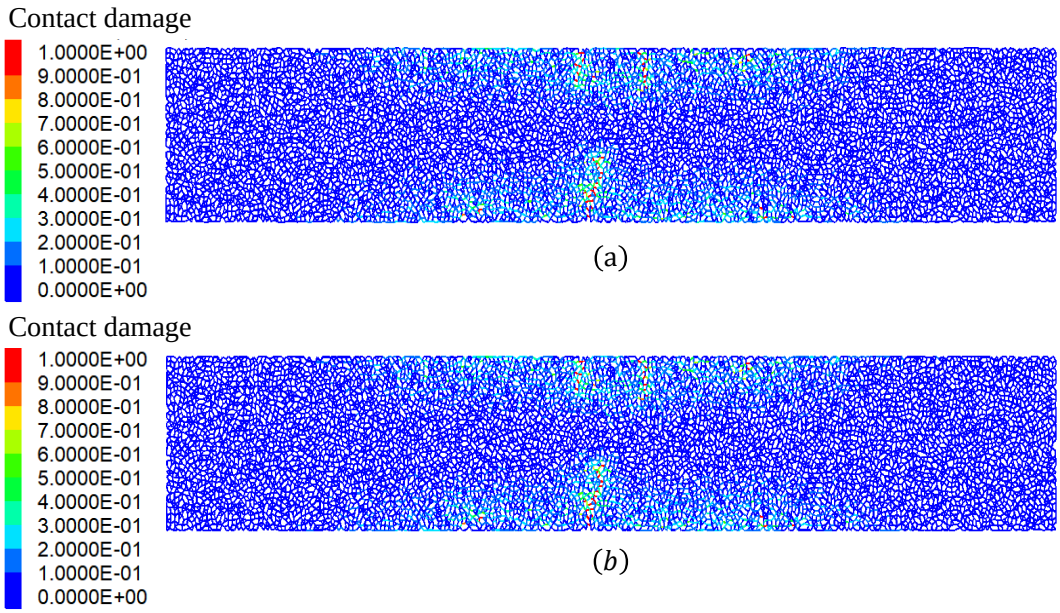

Figure 5.21: Damage maps obtained for a damage fraction $F_v/F_{v0} = 0.4$ with different strain levels (a)$\varepsilon_{max} = 115\ \mu m/m$ at $N_C = 739703$ and (b) $\varepsilon_{max} = 150\ \mu m/m$ at $N_C = 256523$.

5.6.5 Summary of parametric study

The parameter study is conducted in terms of the parameters of Bodin's damage model in Equation 5.7 and 5.8. Parameter C acts as a scaler of the whole fatigue curve F_v/F_{v0} versus N_C. Parameters α and β affects the shape of the fatigue curve. The parameter α has a stronger influence on the first phase of the fatigue curve. The accumulation of errors on the damage calculation depends on the evolution of the damage variable during the time integration. A faster evolution of the system should be associated to smaller values of the cycle jumping parameter ΔN_C to avoid larger numerical errors.

5.7 Calibration of the material parameters and comparison with 4PB experiments

In the 4PB tests of Arsenie [1], the strain level is driven by the value of maximum amplitude of the normal strain ε_{max} (obtained on the top and the bottom of the middle section). The values adopted in her experimental study were $\varepsilon_{max} = 115\,\mu m/m,\ 135\,\mu m/m,\ 150\,\mu m/m$. ε_{max} is theoretically related to the vertical

displacement of the central supports δ_v by Equation 5.15. Respectively, on the simulations the values $\delta_v = 76.7\,\mu m$, $90\,\mu m$, $100\,\mu m$ are adopted. For the discrete element material description, as in previous simulations, the radius of particles follows a uniform distribution. The average value is $\overline{R} = 2.9\,mm$ and the size ratio is $R_{max}/R_{min} = 1.6$. The contact stiffness is $k_n = 2.0 \times 10^{10} N/m$, $k_r = 4.5$, corresponding to a Young's modulus $E = 11\,GPa$ and a Poisson's ratio $\nu = 0.34$.

The experimental results are based on the analysis of 3 samples per strain amplitude ε_{max}. For the simulations, three different ensembles are generated with a similar internal structure and slightly different number of particles (8288, 8282 and 8317).

The value of the number of cycles N_C is averaged for equal levels of stiffness fraction F_v/F_{v0}. The fatigue life is defined as the necessary number of cycles N_C to reach a stiffness fraction $F_v/F_{v0} = 0.4$ in order to analyse the same ranges of values than Arsenie.

In Figure 5.22, the experimental results of the stiffness fraction F_v/F_{v0} as a function of the number of cycles N_C for $\varepsilon_{max} = 135\,\mu m/m$ and $150\,\mu m/m$ are presented. The envelope curves with minimum and maximum values show the relatively large variation of the results. The average curves are the reference for the calibration of the parameters of the fatigue model $C = 8.7 \times 10^8$, $\alpha = -2.0$ and $\beta = 3.0$.

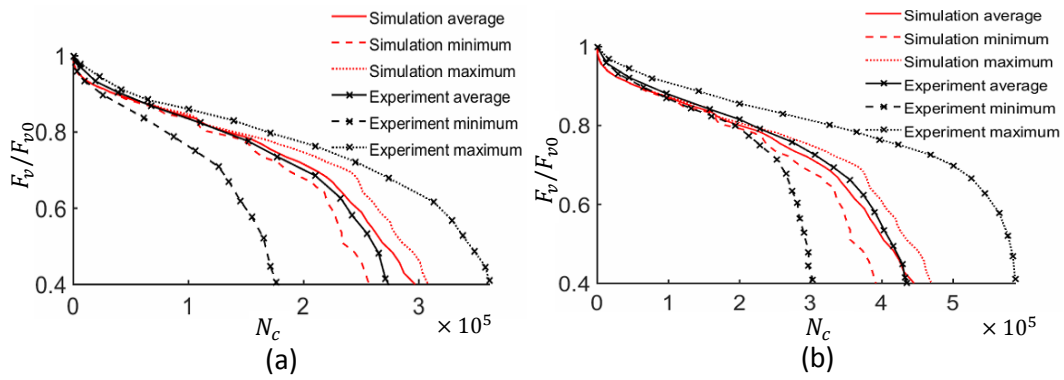

Figure 5.22: Stiffness fraction F_v/F_{v0} as a function of the number of cycles N_C for (a) $\varepsilon_{max} = 135\ \mu m/m$ and (b) $\varepsilon_{max} = 150\ \mu m/m$. Comparison between DEM simulations of 4PB tests and experiments of Arsenie [1].

The average results of the simulations are in very good agreement with the experimental results, which points out the capabilities of the DEM model. The

envelopes of results of the DEM simulations depends on the micro structure of the ensembles (granulometry, void ratio, etc.), which is an important feature of discrete approaches, even if not quantitatively correlated to experimental observations in all cases. Three numerical samples presents different damage evolutions and strain localizations due to different micro structures of each sample. The damage maps of each analysed sample (Figure 5.23) bring up some physical elements related to the variation of results. After a roughly homogeneous damage, mostly localized at the central span, the irregularity of the inner structure of the material induces different weak points. These points give rise to concentrated damage zones, physically associated to cracks. The propagation of this cracks affects the sample response which explain most of the visible differences between the curves $F_v/F_{v0} \times N_C$.

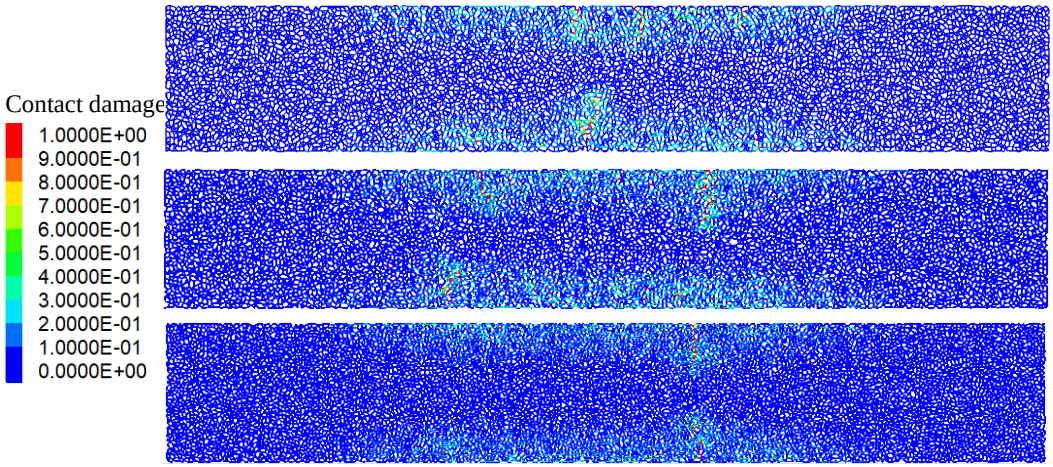

Figure 5.23: Damage map for all the three samples for a stiffness fraction $F_v/F_{v0} = 0.4$.

The Figure 5.24a synthesizes the calibration of the DEM fatigue model. The average curves of stiffness fraction F_v/F_{v0} evolution for all different strain levels studied experimentally and numerically are placed together. One may observe that calibrations take into account only experimental data for $\varepsilon_{max} = 135\ \mu m/m$ and $\varepsilon_{max} = 150\ \mu m/m$. This choice, which does not affects the generality of the further results, is based on some unusual aspects of the results for $\varepsilon_{max} = 115\ \mu m/m$. The most important is the absence of β relating all range of ε_{max} as indicated in Figure 5.24b, which is unusual considering that β is a typical pavement design parameter. Secondly, the shape of the fatigue curve for $\varepsilon_{max} = 115\ \mu m/m$ does not present a clear phase I, which suggests another atypical behaviour that is not captured by DEM simulations. Thus the following study

concerns on the strain level 150 $\mu m/m$ and 135 $\mu m/m$.

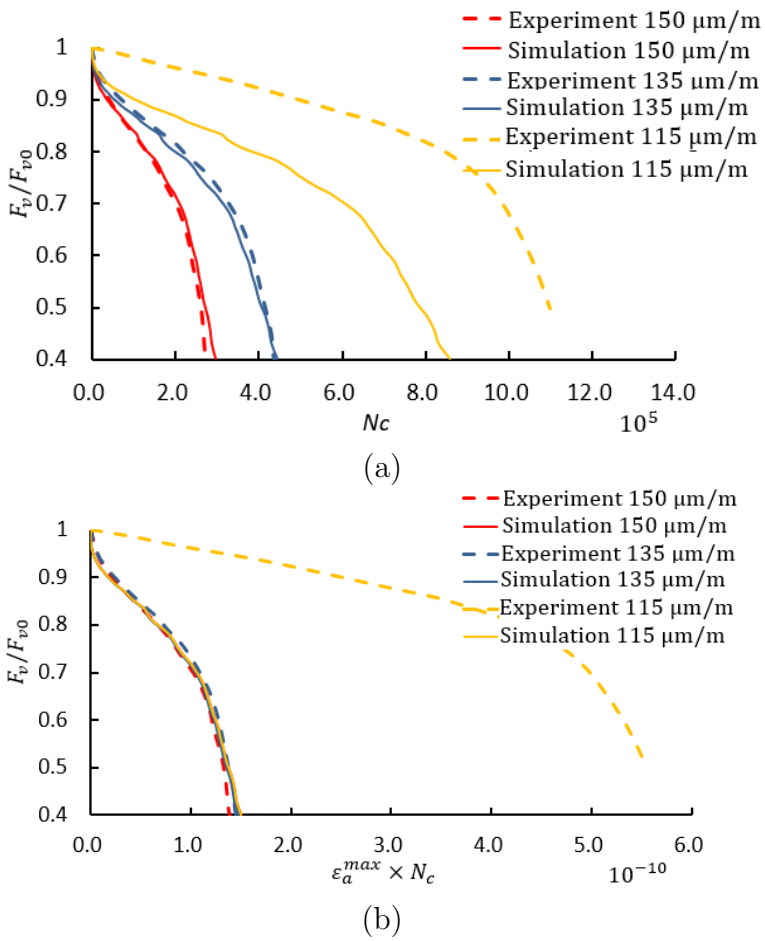

Figure 5.24: Stiffness fraction F_v/F_{v0} as a (a) function of the number of cycles N_C and as a (b) function of $\varepsilon_{max}^{1+\beta} \times N_C$ for different ε_{max}. Comparison between DEM simulations of 4PB tests and experiments of Arsenie [1].

5.8 Effect of the glass fiber grids in 4PB tests

The fiber grids present different mechanical effects in 4PB tests. Two main roles of the fibers are treated in this section: as reinforcements and as interfaces. Firstly, the simulation of the reinforcements and their individual effects in monotonic and cyclic loading are discussed. Then, the effect of interfaces is analyzed separately on fatigue process. After the integration of the both mechanical behaviours, a comparison with experimental results of Arsenie [1] is presented.

5.8.1 Simulation of the reinforcements

The cross section of the bending samples is presented in Figure 5.25a. Fatigue tests of the yarns indicate a neglectful modulus factor in the strain amplitude associated to the 4PB test performed usually in pavement design [121]. Considering the lack of precise information about the fatigue behaviour of the contact between asphalt concrete and fiber glass, a perfect adhesion hypothesis is adopted. Consequently, the contribution of the yarns in $2D$ is taken as elastic axial reinforcements working under tension and compression (bars). The elastic stiffness k_f of one segment i of a fiber glass reinforcement is determined by the expression:

$$k_{fi} = \frac{E_f A_f}{l_i}, \tag{5.17}$$

where E_f is the elastic modulus of the fiber grid and A_f is the total cross section of fiber grid per layer and l_i is the length of the segment. The effect of the bars are then taken into account on the discrete element model as additional contacts (Figure 5.25b) connecting particles located at the vertical position of each layer, as shown in Figure 5.25c. The contact properties are simply E_f and A_f, whilst the length l_i are automatically calculated based on the distance between the conected particles.

An advantage of the $2D$ approach presented here is that cracks and any defects may cross the fiber grid as in real experiments.

5.8.1.1 4PB monotonic test

A simple monotonic bending test is performed here to verify the fiber grid contribution. Considering a perfect adhesion between the reinforcements and the asphalt concrete matrix, and the small amplitude of the strain, the expected behaviour may be similar to the predictions of beam theory.

The addition of the fiber reinforcement has an effect on the flexural stiffness $\overline{EI}$ of the composite beam which writes

$$\overline{EI} = EI + E_f I_f, \tag{5.18}$$

where $EI = E \times wh^3/12$ is the flexural stiffness of the asphalt concrete section (without the reinforcements), E_f and I_f are, respectively, the Young's modulus of the fibers and the moment of inertia of the fibers with respect to the center of

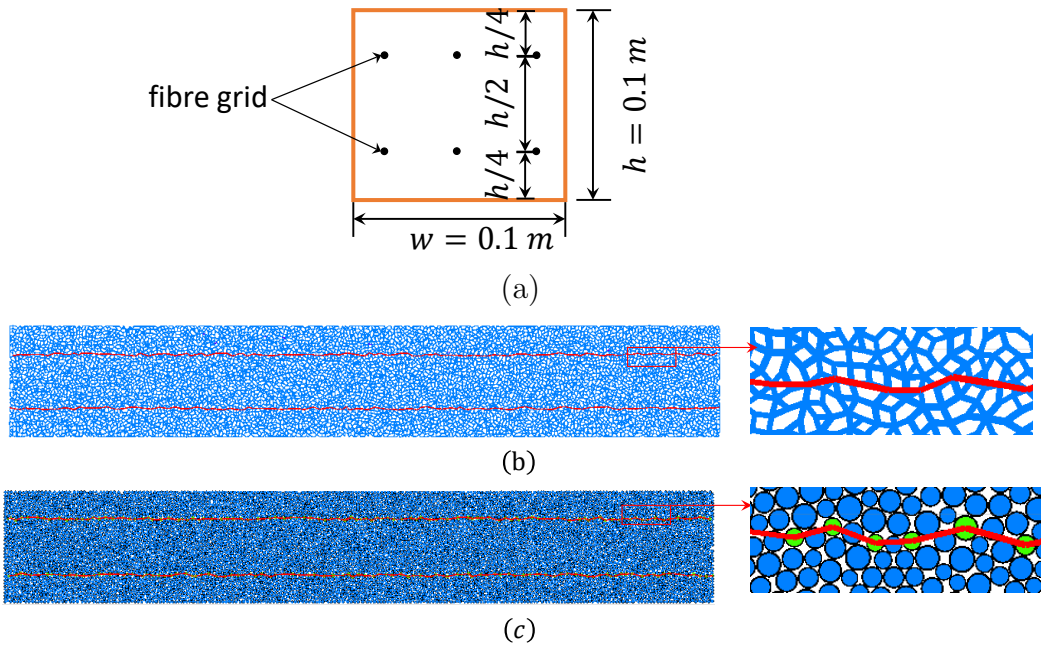

Figure 5.25: (a) Cross section of the 4PB samples. Representation of the reinforcement bars (b) as additional contacts (c) connecting particles in the same layer.

gravity (which coincides with the flexural center) of the section. The moment of inertia of the 2 layers of reinforcements can be calculated by the Huygens-Steiner theorem of parallel axis as

$$I_f = 2 \times A_f (d_f/2)^2, \tag{5.19}$$

where $d_f/2$ is the distance between the center of gravity of the beam and the position of the reinforcements.

The reaction force F_v can be related to a central support displacement δ_v (4PB configuration) by the expression [122]:

$$F_v = \frac{384\overline{EI}\delta_{v,mid}}{6.81L^3}, \tag{5.20}$$

where L is the length of the beam, $\delta_{v,mid}$ is the displacement in the middle of the beam.

For the 4PB beam, $\delta_{v,mid} = 1.15\delta_v$, where δ_v is displacement at two load

supports. Simulations with 3 different imposed displacements are considered $\delta_v = 76.7\ \mu m,\ 90\ \mu m,\ 100\ \mu m$. In order to precisely quantify the contribution of the fiber grid reinforcement, the first step is the identification of the flexural stiffness EI of the asphalt concrete beam. Based on the same elastic properties of Section 5.7 and no reinforcement ($A_f = 0$), one obtain EI from measured F_v and Equation 5.20 for $\overline{EI} = EI$.

In $2D$ simulations, the beam has a unit width $b = 1\ m$. The total quantity of fiber per meter in one layer of reinforcement $A_f = 30 \times 4 \times 10^{-6}\, m^2$. The Young's modulus of AC takes the value of $11\, GPa$, which is measured experimentally for a strain lever $\varepsilon_{max} = 40\, \mu m/m$, frequency $10\, Hz$ and temperature $10°C$ [1]. In Figure 5.26a, the reaction F_v is related to the different values of δ_v for the beam with and without reinforcements. The results with fibers follow the predictions of Equation 5.20 as can be seen in more detail in Figure 5.26 with less than 0.5% of relative error.

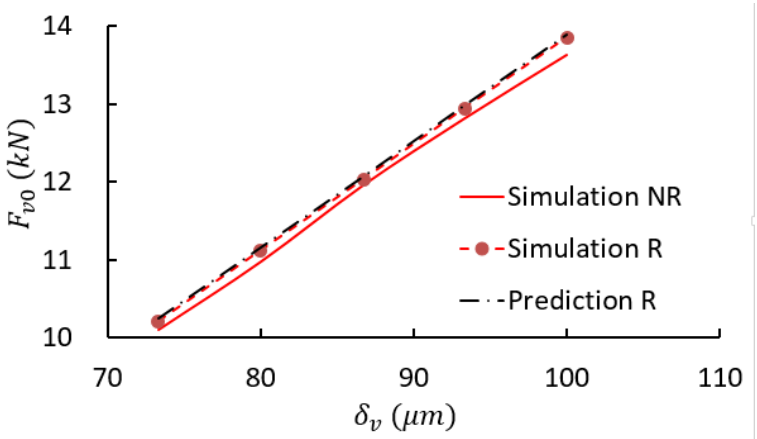

Figure 5.26: (a) Reaction force F_v as a function of the displacement of the central support δ_v. R: with reinforcement, NR: without reinforcement.

5.8.1.2 Effect of the fiber reinforcements on the fatigue behaviour of 4PB tests

In Section 5.8.1.1, a usual quantity of fiber reinforcements are adopted on the monotonic verification of the model. One may easily observe (in Figure 5.26) the relatively small increment on the stiffness of the composite beam due to the fibers. This results are not specially surprising, since this type of reinforcements is developed to improve the fatigue life of asphalt concrete components. The acceptable errors of simulations are from 10% to 12%, comparing to the theoretical

predictions by Equation 5.20.

The contribution of the reinforcements are then analyzed in fatigue with the same three DEM specimens used for 4PB simulation in Section 5.7. The average evolution of the stiffness factor F_v/F_{v0} as a function of the number of cycles N_C is shown in Figure 5.27 for a strain amplitude of $\varepsilon_{max} = 150\ \mu m/m$. The comparison between experiments [1] and simulations indicates an improvement of the fatigue life induced by the reinforcements, however the total effect of the grids seems underestimated by the simulations.

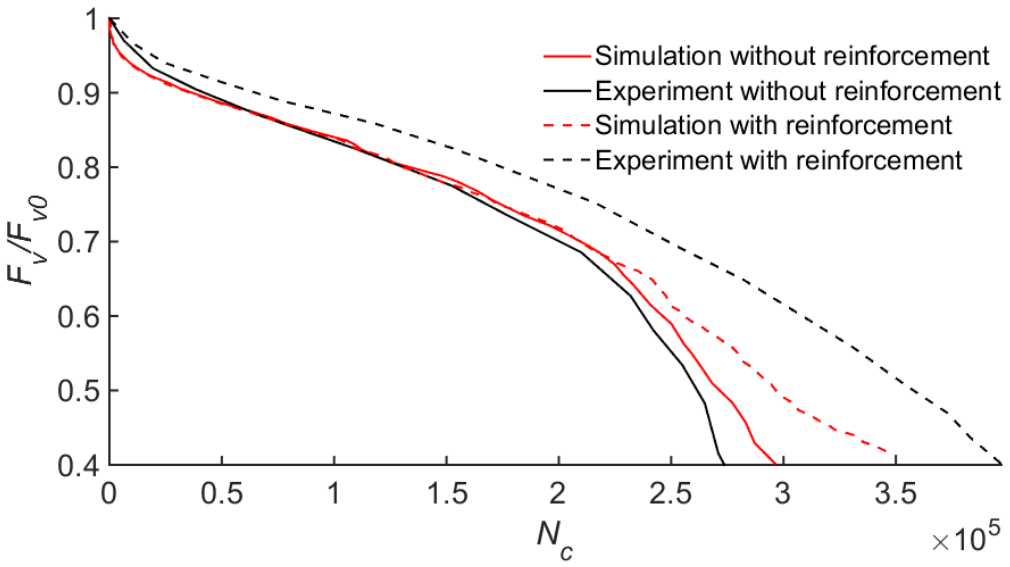

Figure 5.27: Stiffness fraction F_v/F_{v0} as a function of the number of cycle N_C in 4PB tests ($\varepsilon_{max} = 150\ \mu m/m$). Comparison between DEM simulations and the experiements of [1].

The mechanism of reinforcement reproduced by the simulations can be visualized in Figure 5.28 for one of the samples. The effect of the fiber is very reduced on the initial phase of the fatigue test (Figure 5.28a). It seems associated mostly to the elastic contribution observed in Figure 5.26, since the fibers are located in zones with reduced damage (Figure 5.28b). After approximately $F_v/F_{v0} = 0.7$, the fiber contribution increases considerably. This seems specially associated to the concentrated damage crossing the fiber position (Figure 5.28c). The strain at the fiber positions are locally increased which activates the mechanism of reinforcement.

The contribution of the reinforcements seems to be more effective when the fibers are located in a damaged zone. The experimental results indicate that fibers may

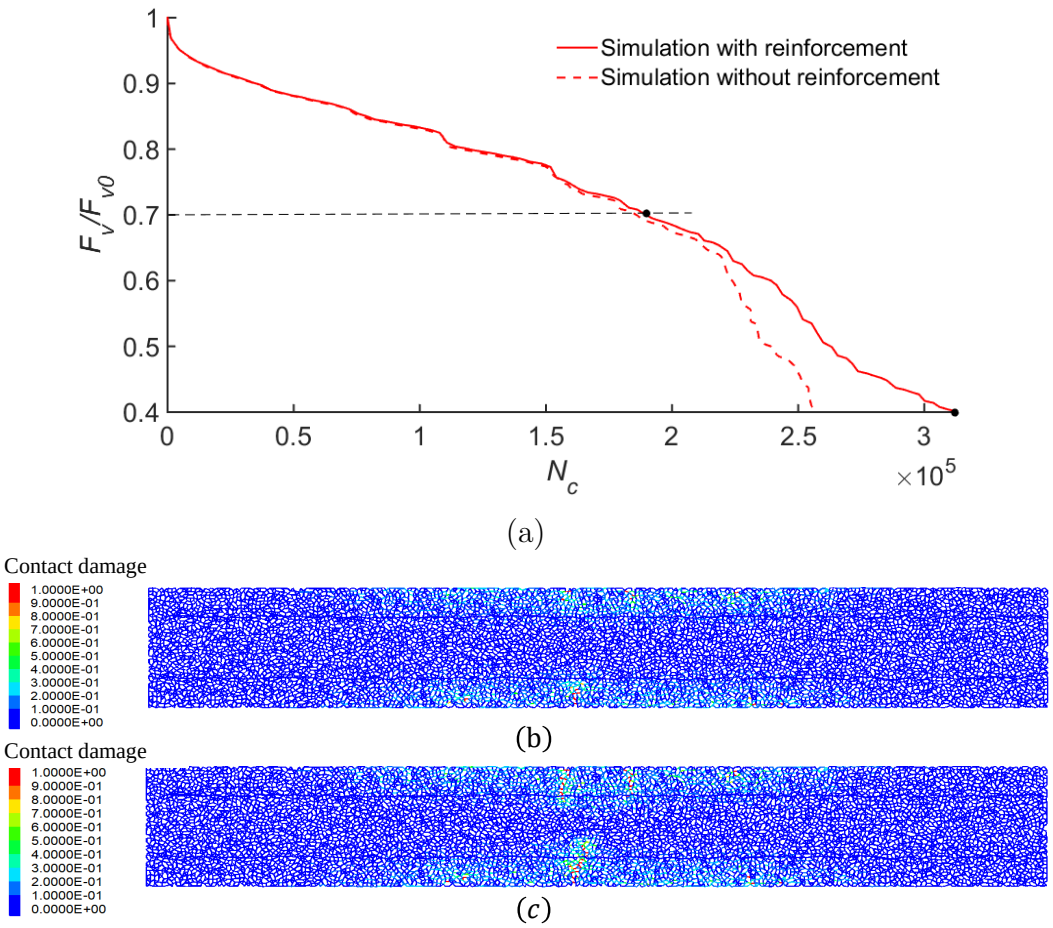

Figure 5.28: (a) Stiffness fraction F_v/F_{v0} as a function of the number of cycle N_C in 4PB simulations for one sample (particle number: 8282). Damage map with reinforcement for (b) $F_v/F_{v0} = 0.7$ and (c) $F_v/F_{v0} = 0.4$.

contribute since the beginning of the fatigue test and not only after a certain number of cycles (Figure 5.27a). More elements must be considered on the model to capture the complete mechanism of reinforcement.

5.8.2 Simulation of interfaces

As shown in Chapter 4, the fiber grid associates an interface between the asphalt layers with a lower normal stiffness. The tangential behaviour of this interface was not experimentally characterized in *SolduGri* project, however, a parametric study may show the effect of this mechanism in 4PB tests.

The interfacial behaviour is modelled by the introduction of different elastic prop-

erties in a thin layer of particles. The interface is represented by the contacts which cross the fictitious straight lines where the fiber glass grids may be located (see Figure 5.29a). When submitted to relative tangential displacements δ_s the interfaces may present a tangential stress response $\tau = F_s/(2L \times t)$, where L is the length of the beam and t its width. The setup in Figure 5.29b is adopted to identify the interface tangential stiffness

$$K_t = \frac{\tau}{\delta_s} = \frac{F_s}{2L \times t\delta_s}. \tag{5.21}$$

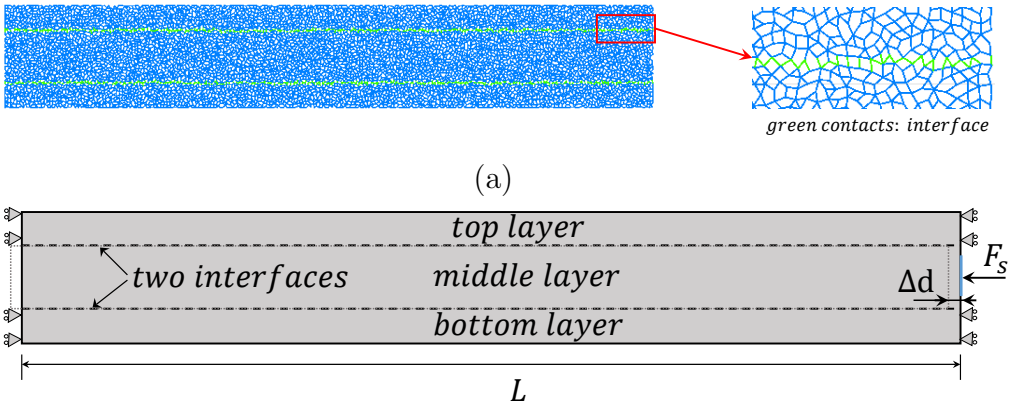

Figure 5.29: (a) Interface representation in DEM 4PB simulations. (b) Geometry of the shear test adopted in the characterisation of the interface.

Three samples (identical to 4PB ones) are used on the simulations of the shear test. A shear displacement $\delta_s = 0.4\,mm$ is imposed. Different contact stiffness $2.0 \times 10^6\,N/m \leq k_n \leq 2.0 \times 10^9\,N/m$ (for a stiffness ratio $k_{ratio} = k_n/k_s = 4.5$) are associated to the particles composing the interfaces. The relation between k_n and the interface shear stiffness K_t is shown in Figure 5.30. The identified trend is approximately reproduced by the expression

$$K_t = f(k_n) = 2\times10^7 \times (log_{10}k_n)^3 - 5\times10^8 \times (log_{10}k_n)^2 + 5\times10^9 \times log_{10}k_n - 2\times10^{10} \tag{5.22}$$

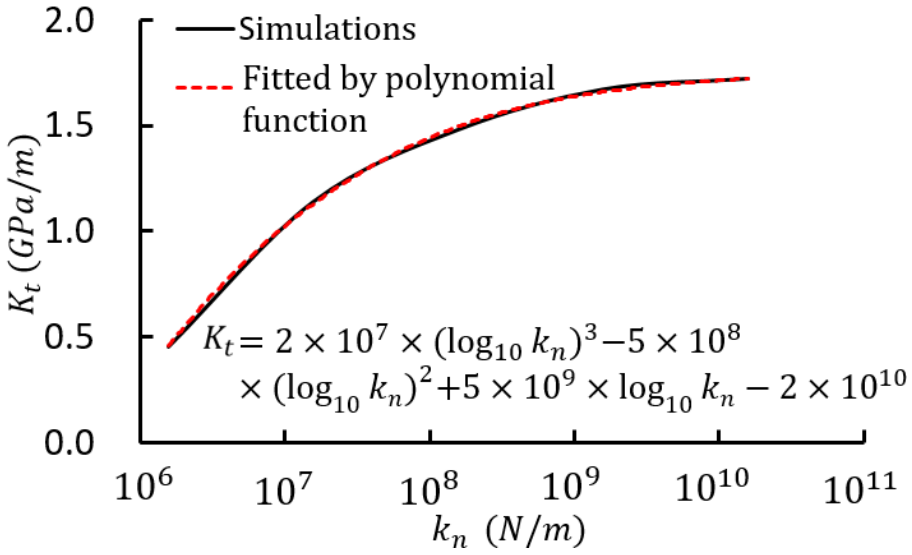

Figure 5.30: Relation between interface shear stiffness K_t and interface contact stiffness k_n in logarithm for the shear test presented in Figure 5.29

5.8.2.1 Effect of the interface on the fatigue behaviour of 4PB simulations

The three 4PB samples present a contact modulus $E_{cmod} = 2.0 \times 10^{10}\,Pa$ and a stiffness ratio $k_r = 4.5$, which corresponds to the material properties: Young's modulus $E = 11\,GPa$ and Poisson's ratio $\nu = 0.34$. The parameter of the damage model $\alpha = -2.0$, $\beta = 3.0$ and $C = 8.7 \times 10^8$ are the same of the simulations of Section 5.7. The interface is supposed to present an elastic behaviour (no damage is associated during the fatigue tests). A strain amplitude $\varepsilon_{max} = 150\,\mu m/m$ is applied in the following simulations. The effect of the shear stiffness of the interface K_t is presented in Figure 5.31 for $0.47\,GPa \leq K_t \leq 1.63\,GPa$. As it can be seen in Figure 5.31a, the decrease of K_t induces an increase of the fatigue life. Parallelly, a general decrease on the stiffness of the beams is associated to the decrease of K_t, visible by the reduction of the reaction force F_v in Figure 5.31b. The reduction of stiffness for intact beams ($D = 0$) visible on the beginning of the fatigue test is simply associated to the reduction of the moment of inertia of the beams when K_t is reduced. For $K_t \to K_{t\ max}$, the moment of inertia of the beams is $I_{max} = bh^3/12$. For $K_t \to 0$, the three layers works separately in bending, which conducts to a moment of inertia $I_{min} = 2 \times b(h/4)^3/12 + b(h/2)^3/12 = (5/32)bh^3/12$. The ratio $I_{min}/I_{max} = 5/32 \approx 0.156$ corresponds to the maximum reduction of nearly 84% on initial force F_v, while the observed

reduction at $K_t = 0.47\,GPa/m$ is approximately 0.3.

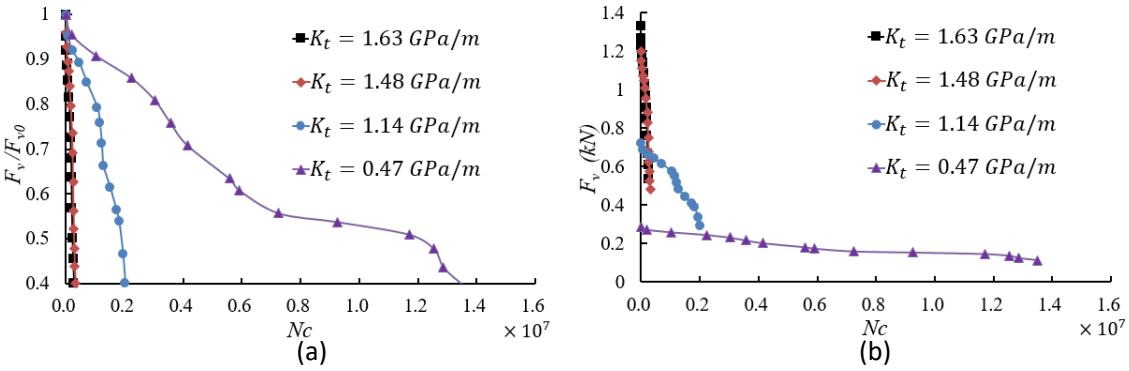

Figure 5.31: Results of 4PB fatigue tests: (a)Force ratio F_v/F_{v0} and (b) force F_v as a function of the number of cycles N_C for different interface shear stiffness K_t.

The shear stiffness K_t has a considerable effect on the distribution of damage inside a beam under 4PB test. In Figure 5.32, a comparison between 3 different values of $K_t = 1.63\,GPa/m$, $1.14\,GPa/m$, $0.47\,GPa/m$, respectively, stiff, intermediary and smooth interfaces is made. Different values of the shear stiffness induces consequently different distribution of the normal stress and strain for an intact structure before the fatigue loading (see the details in Figures 5.32a and 5.32c. For stiffer interfaces, the continuity of the strain distribution between each layer leads to higher values of strain on the top and the bottom of the beam, which causes faster damage evolution at this points, specially in middle section. On the other hand, for very smooth interfaces, each beam presents a roughly independent strain distribution, associated only to the imposed displacements and moment of inertia. It gives rise to faster damage evolution on the top and bottom of each layer, with higher values of damage in the middle layer compared to the other layers, due to its higher height and bending stiffness. The intermediary interface in Figure 5.32b shows the continuous transition between the two extreme conditions with distributed damage over the middle span of the beam.

5.8.3 Coupled effect of reinforcements and interface on 4PB fatigue simulations

The glass fiber grids play a dual role in 4PB tests: as normal reinforcements and as tangential interfaces. Each of these aspects are analysed independently in Sections 5.8.1 and 5.8.2. In this section the interaction between these two mechanical contributions are analysed by DEM simulations. The reinforcements

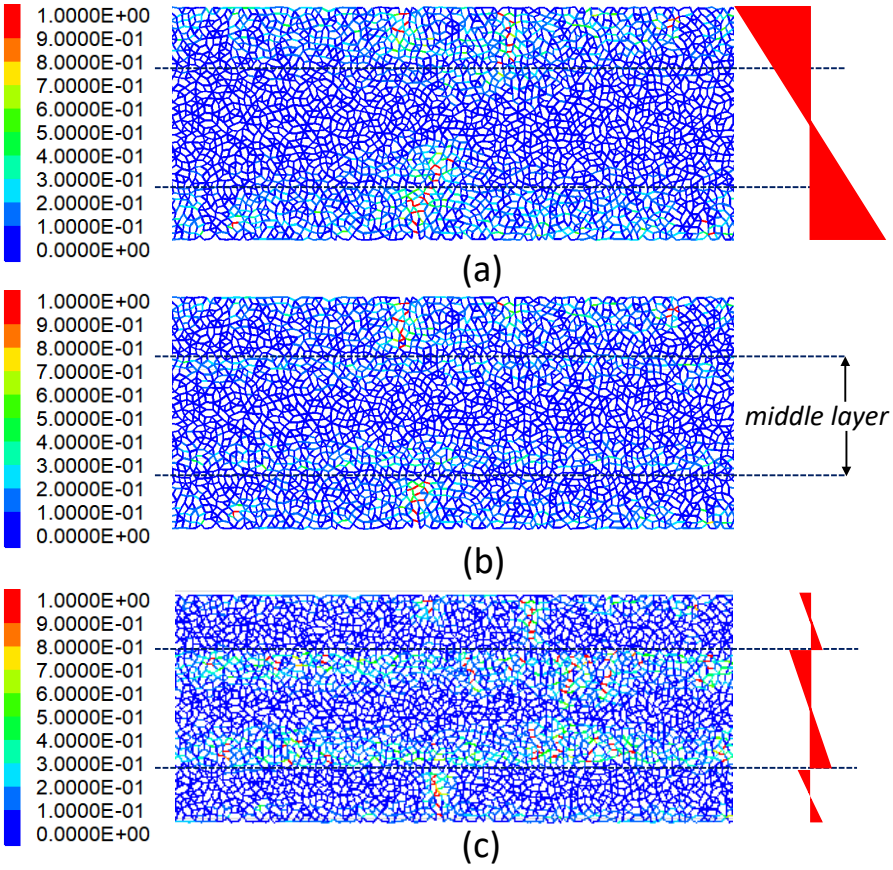

Figure 5.32: Map of contact damage D for a stiffness fraction $F_v/F_{v0} = 0.4$ after 4PB fatigue tests for (a) a stiff interface $K_t = 1.63\,GPa/m$, (b) an intermediary interface $K_t = 1.14\,GPa/m$ and (c) a smooth interface $K_t = 0.47\,GPa/m$. In detail, the scheme of the distribution of normal stress (and strain) for stiff and smooth interfaces with static load before damage.

are placed inside the middle layer close to the interfaces, as shown in Figure 5.33. The same samples and the same material properties (asphalt concrete, interface and reinforcement) from previous sections are adopted.

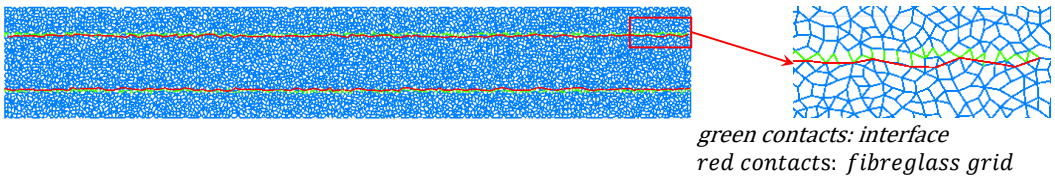

Figure 5.33: Interface and the position of the reinforcements in DEM 4PB simulations.

A comparison between the effect of the reinforcements for a stiff interface ($K_t = 1.63\,GPa/m$) and a smooth interfaces ($K_t = 0.47\,GPa/m$) is presented in Figure 5.34 for an amplitude of $\varepsilon_{max} = 150\,\mu m/m$. The stiffness of the interface effectively dominates the effect over the bending stiffness of the beams, as visible in Figure 5.28a. The quantity of reinforcements is relatively small to affect the elastic behaviour of the samples, however, it can affect considerably the fatigue response under certain conditions. As shown in Figure 5.28, the damage takes a certain number of cycles N_C to reach the reinforcements and activate their (relatively small) contribution, as presented again in Figure 5.33. For smooth interfaces, as shown in Figure 5.32c, the damage is concentrated close to the position of the reinforcements, which explains the activation of the contribution of the reinforcements practically since the beginning of the fatigue test. A much stronger effect of the reinforcements is observed, with a fatigue life increased by almost twice in comparison to the results without them.

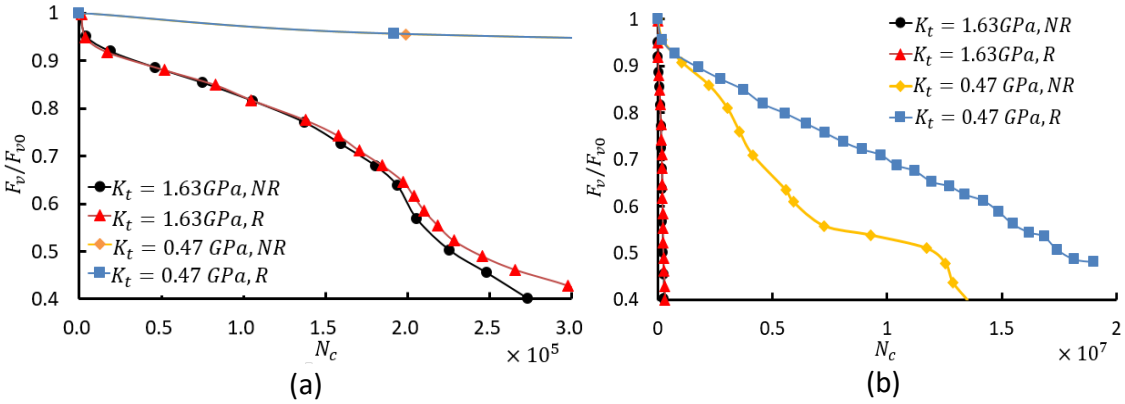

Figure 5.34: Reinforcement effect with stiff and smooth interfaces on the stiffness factor F_v/F_{v0} as a function of N_C: (a) $0 \leq N_C \leq 3\times10^5$ and (b) $0 \leq N_C \leq 2\times10^7$ for $\varepsilon_{max} = 150\ \mu m/m$.

5.8.4 Model for the contribution of fiber grids on the fatigue behaviour of 4PB tests

The contribution of each mechanism (reinforcement/interface) is inferred based on the comparison with experimental results [1]. The precise information about the cross section of the fiberflass grids simplifies the quantification of their reinforcement behaviour. As in Section 5.8.1, a cross section of fiberglass per meter and per layer $A_f = 30\times4\times10^{-6}\,m^2$ is adopted on the following simulations. The interface effect is more uncertain; for this reason 2 different values of interface

stiffness are analysed on the simulations $K_t = 1.48\,GPa/m$, *and* $1.38\,GPa/m$, which induces respectively an initial loss of stiffness with respect of the results without fiberglass grids of 9% and 17% as shown in Table 5.1, which is in the range of about 10% identified by Arsenie [1].

Table 5.1: F_{v0} comparison of (non-)reinforced numerical samples with different interface K_t. NR: without reinforcement, R: with Reinforcement and interface.

strain level ($\mu m/m$)	**150**		**135**	
F_{v0} $NR\,(N)$	13658		11985	
$K_t\,(GPa/m)$	1.48	1.38	1.48	1.38
F_{v0} $R\,(N)$	12241	11228	10945	10106
Reduction (%)	10	17	9	16

The comparison of the simulation results and experiments is presented for two different strain levels $\varepsilon_{max} = 135\ \mu m/m$ (Figure 5.35a) and $\varepsilon_{max} = 150\ \mu m/m$ (Figure 5.35b). The simulations results represent the average behaviour of 3 samples, whilst experiments average, maximum and minimum envelopes are the results of the analysis of 6 samples.

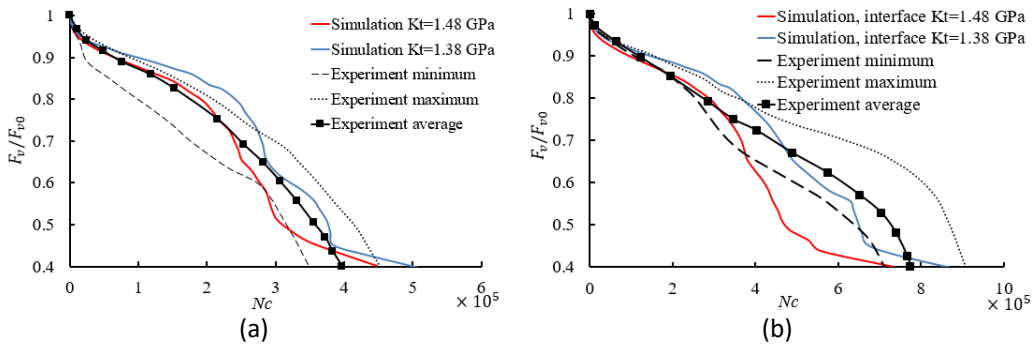

Figure 5.35: Stiffness factor F_v/F_{v0} as a function of the number of cycles N_C for 2 different strain levels (a) $\varepsilon_{max} = 150\ \mu m/m$ and (b) $\varepsilon_{max} = 135\ \mu m/m$. Comparison between simulations for different $K_t = 1.48\,GPa$ *and* $1.38\,GPa$ and experimental results [1].

Despite the absence of more precise information about the values of interface stiffness K_t the simulations capture the main trends of the experimental results. One may observe that experimental average behaviour remains roughly close to the simulation results with the proposed values of interface stiffness

$1.48\,GPa < K_t < 1.38\,GPa$. Considering the variation of the experimental results, the simulations remain globally inside the maximum to minimum envelopes. The deviation from the experimental results may result from the limitations of 2D structure of the simulations, the position of the interface (assume to be beside the fiber grid) and the undamageable nature of the interface in simulations. The combination of the fiber grid and the resultant interface between them can roughly reproduce the experimental results, which inspires to the further study of the interface behaviour.

5.9 Summary of the chapter

A fatigue damage model for asphalt concrete is adapted and implemented in a discrete element environment. A simple model describing material bulk fatigue behaviour (phases I and II) associated to the natural disordered micro structure of the discrete model is shown to be able to describe the entire fatigue behaviour (phases I, II and III) in a sample scale. Phase III appears as a structure effect manifested even under uniform boundary conditions, which is characterized by a loss of homogeneity induced by the concentration of defects and a localization of the strain.

After a parametric study and the calibration of the discrete model for 4PB tests, the effect of glass fiber grids is analysed. Two main contributions are evoked for the effect of fiber grids: as normal reinforcements and as tangential interface. The results indicate that reinforcements are activated near very damaged points. The low quantity of fiber is not apparently enough to explain individually the improvement of the fatigue life observed on the experiments [1]. However, the fatigue life can be highly extended in spite of the initial stiffness of the sample.

The damage distribution seems to be considerably affected by the interface mechanism. It seems to be related to its effects on the distribution of the strain, which allows a better mobilisation of the middle asphalt layer and consequently improves the reinforcement behaviour.

Finally, a comparison between simulations and experiments [1] shows the quantitative consistency of the model on describing the main trends and the corresponding mechanisms affecting 4PB fatigue tests of asphalt concrete with fiber glass grids.

Chapter 6

Conclusions and perspectives

Contents

6.1 Conclusions

In this thesis, the mechanical response of the asphalt concrete (AC) under monotonic and fatigue loadings was modelled by discrete element method. Based on this material behaviour, the effect of fiber glass grids associated to asphalt concrete was taken into account and its mechanical contribution was analysed.

As discussed in Chapter 3, the materials were modelled by random packed ensemble of particles. An inner stress release method was used to induce a nearly isotropic and homogeneous internal structure with reduced inner voids. A parametric study allowed to relate the contact parameters (contact modulus E_{cmod} and stiffness ratio k_{ratio}) to the material parameters (Young's modulus E and Poisson's ratio ν) in elasticity.

Quasi-brittle behaviour is limited by two rupture mechanisms: one related to the stress level and the other by the stress intensity factor. These two mechanisms are usually associated to two material properties, respectively, tensile strength and toughness. A calibration procedure based on the analysis of the nominal strength of pre-cracked samples allowed the identification of relation between these material parameters and the contact parameters: normal and tangential strengths, and the particle average radius. The control of the parameters of (quasi-brittle) rupture was verified by the comparison of the results of wedge-splitting simulations with the prediction of linear elastic fracture mechanics.

In Chapter 4, the limits of a quasi-brittle approach on the description of asphalt

concrete are discussed. The energy released during the (monotonic) rupture of asphalt concrete (wedge-splitting) samples is much higher than the prediction of linear elastic fracture mechanics, which is based on the value of the toughness. This non-linearity associated to the rupture can be explained by the notion of fracture process zone. In terms of discrete element modelling, a bilinear cohesive contact law was implemented, where the control of the rupture energy was clearly introduced as a parameter. As a consequence, realistic simulation results of asphalt concrete were obtained. The subsequent analysis of wedge-splitting tests with interfaces between asphalt concrete and fiber glass grids has shown that rupture process is almost integrally dominated by the interface mechanical properties. The asphalt concrete behaving as a rigid body leads to a simplified modelling of WST based only on the three parameters: stiffness, strength and energy release rate of the interface. The comparison of this interface model has shown good agreement with experimental results.

In Chapter 5, an alternate fatigue model for asphalt concrete was implemented in discrete element method. A damage contact model describing phases I and II, associated with the natural disorder of the inner structure of the material in DEM is shown to be able to describe the whole fatigue behaviour (phases I, II and III) in a sample scale. Phase III appears as a structure effect manifested even under uniform boundary conditions, which is characterized by a loss of homogeneity induced by the concentration of defects and a localization of the strain. Simulations of 4 point bending tests were then performed to analyse the influence of the fiber glass grids on the fatigue response of the composite beams.

The damage increments per cycle were defined by the strain amplitude. Alternate cycles were numerically replaced by a static imposed deflection of the samples, which accelerated the calculation and allowed the study of the fatigue behaviour under a realistic high number ($10^5 - 10^6$) of cycles.

A parametric study and the calibration of the 3 fatigue parameters of the discrete model for 4PB tests has shown the capabilities of the model on reproducing experimental results of asphalt concrete samples. Thus the effects of the fiber grids were analysed from two points of views: as normal reinforcements and as interfaces. The normal reinforcements were represented by complementary elastic contacts at the same position of the fiber grids and presenting the same stiffness. The advantage of this bidimensional approach is to allow a free propagation of defects through the fiber grid (as it happens in reality). The interface was characterized by a thin layer of particles with lower elastic stiffness to induce

relative sliding between two adjacent layers. The normal contribution of this layer was neglectful considering the low cross section of the interface layer. The effect of each of the mechanisms was first separately quantified. The simulation results indicate that reinforcements are activated near very damaged points, where the strain is localized. The low quantity of fiber is not apparently enough to explain individually the improvement of the fatigue life observed in the experiments [1]. However, the sliding induced by the interface may cause a redistribution of the normal strain with a reduction of maximum values, which extends the fatigue life of the whole beam in spite of its initial stiffness. Considering the coupled effect of the reinforcements and the interface, the redistribution of the strain has the consequence of increasing the damage near the position of the reinforcements, which improves the efficiency of the effect of the reinforcements. Finally, the comparison between simulations and experiments has shown the consistency of the model and the trends indicated by the simulations.

6.2 Perspectives

The numerical models developed and discussed in this thesis have indicated some trends, clarified some experimental results and instigate some questions.

For all calculations, the granularity of the simulated materials was kept the same. In Chapter 3, the effect of the average particle size was raised in the relation between the tensile strength and the toughness of a quasi-brittle material. As shown in Appendix B the quasi-brittle behaviour may also depend on the transition between the rupture mechanisms based on strength and toughness, characterized by the parameter r. A physical explanation for the size effects in quasi-brittle rupture may emerge from the analysis of the effect of the granularity on the rupture of pre-cracked samples.

The damage models were oriented to simulate asphalt concrete behaviour and its interactions with glass fiber grids. However, the approaches in monotonic and repeated loads can be extended to other (geo)materials and other (geo)grids.

Some important effects related to the mechanical behaviour of asphalt concrete were not explicitly isolated. An important aspect to be included on the modelization is the identification of the elastic and viscous contributions on the material response. The fatigue tests are usually conducted at relatively high frequencies which affects the material response. The temperature is also a parameter to be

considered in future, which affects the viscosity of the asphalt in laboratory and in real structures.

The fatigue tests associated to asphalt concrete samples are usually strain controlled. The reinforcement behaviour of the fiber grid seems to be activated at elevated levels of damage and consequently low levels of sample stiffness. Stress controlled tests may eventually be able to show more clearly the contribution of the fiber grid at residual levels of stiffness.

The fiber grid properties were considered to be perfectly elastic in all calculations. The grid itself presents a roughly constant stiffness in fatigue tests with strain levels comparable to the ones of the bending test that were presented [121]. However, the behaviour of the connection between the fiber glass and the asphalt concrete is not forcedly independent on the number of cycles. Repeated cycles pull out tests may give important information about the fatigue behaviour of this connection. The normal and, specially, the tangential behaviour of the interface asphalt concrete/grids under fatigue is also an important future input for the modelizations of composite beams. An interface which presents a considerable loss of stiffness during the tests may contribute very differently than proposed by the numerical results of this work. Despite all the present uncertainty with respect to the characterization of the interfaces, the control of the properties of these thin layers seems to be a possible path for the optimization of the fatigue performance of structural elements in asphalt concrete.

Appendix A

Discrete element method

DEM was originally developed to model granular systems [123–125]. Afterwards, it is used to study the fracture of quasi-brittle materials such as concrete and rocks [113, 126, 127]. Materials are regarded as assemblies of particles and contacts, as shown in Figure 3.1 (a) for a two-dimension assembly. Particles are interacted by contact forces and their motion follow Newton's laws. Particle motion and contact force update in each time-step, which makes the numerical calculation.

A.1 Contact detection and activation

The contacts are detected automatically in each time-step. PFC imposes a kinematic constraint on the time-step in order to guarantee that contacts are created between particles (or walls) prior to the cycle that forces develop [120]. The contact activation is operated in two steps. Firstly, the particle proximity (the geometry distance) is detected and compared with the reference critical proximity δ_{rp}, beyond which value the generation of contact is impossible, i.e. the contact is potential to be created within this particle distance of critical proximity δ_{rp}. Secondly, the contact activation is done within the defined contact gap *agap*. For the linear contact without bond, the *agap* value equals to the reference gap, for the bonded contact, the *agap* value can be defined, which is larger than reference gap (*rgap*) and smaller than the critical proximity δ_{rp}.

A.2 Energy dissipation and Damping

Energy dissipation may occur due to three different mechanisms: friction at contacts, dissipation at contacts (e.g., viscous damping, inelastic contact laws, etc.) or dissipation introduced in the equations of motion of balls and/or clumps. The latter item is called local damping. Local damping acts on each ball, while viscous damping acts at each contact.

A.2.0.1 Global damping

Global damping applies a damping force, with magnitude proportional to unbalanced force, to each ball, as expressed in Equation A.1.

$$\vec{f_d} = -\alpha \mid \vec{f_i} \mid sign(v_i), \tag{A.1}$$

$$sign(y) = \begin{cases} 1 & (if\ y > 0) \\ -1 & (if\ y < 0) \\ 0 & (if\ y = 0) \end{cases} \tag{A.2}$$

where α is the local damping factor, $\mid \vec{f_i} \mid$ is the norm of the vector, and $\vec{f_i} = \vec{f_{n,i}} + \vec{f_{s,i}}$.

Global damping is usually set to a large value (0.7 as indicated and used in [97, 106]) to accelerate convergence toward a stable configuration for quasi-static simulations. This value should be tuned down for dynamic analyses, or even set to zero. Refer to the manual [120] for more information.

A.2.0.2 Viscous damping

Viscous damping adds normal and shear dashpots at each contact, which is given by the following equation:

$$D_i = c_i \mid v_i \mid, \tag{A.3}$$

where c_i is the critical damping constant, which is given by:

$$c_i = \beta c_{i,crit} = 2\beta\sqrt{mk_i}, \tag{A.4}$$

where β is the critical damping ratio and it can be directly set in PFC by user, and $c_{i,crit}$ is the critical damping constant.

A.2.0.3 Usage

For compact assemblies, global damping, using the default parameter setting, is the most appropriate form to establish equilibrium and to conduct quasi-static deformation simulations. When a dynamic simulation of compact assemblies is

required, the local damping coefficient should be set to a low value appropriate to energy dissipation of dynamic waves. Alternatively, viscous damping should be used. For problems involving free flight of particles and/or impacts between particles, global damping is inappropriate, and viscous contact damping should be used.

It should be noticeable that, due to the quasi-static process in this thesis, all the simulations performed in this thesis adopted the global damping ($\alpha = 0.7$) as presented by [120], so that the particles' acceleration is heavily damped.

A.3 Time-step determination

The DEM solution requires a valid, finite time-step, which should be small enough to keep stability of the model, and large enough for the acceptable computing time. For one contact, the critical time-step is calculated by $t_{crit} = \sqrt{\frac{m}{k_{trans}}}$ or $t_{crit} = \sqrt{\frac{I}{k_{rot}}}$, where m is the mass, I is the inertia of the particle, k_{trans} and k_{rot} are respectively the translational and rotational stiffness. The critical time-step for the whole DEM assembly is determined to by the smallest t_{crit} of all the contacts.

A.4 Stabilisation

For a simulation under (quasi-)static condition, the model requires the stable state of force distribution or particle equilibrium, which means that enough time or time-steps are required in order to reach such a balance state or equilibrium. For a quasi-static load, the method of stabilisation is low loading rate or small time-step. It should be noted the critical time-step is in fact the maximum time-step to keep a stable state of model, but may not small enough for the quasi-static load.

In the simulation with requirement of extreme equilibrium, the stabilisation within a certain tolerance should be worked out with all boundary condition fixed unmovable, taking the stress control in model generation (See Section 3.3.1) as an example.

A.5 Generator random seed

In the randomly generated model, the graded particles are randomly created within the assigned domain. Therefore, their locations and sizes are affected by the state of the random-number generator. The random-number generator itself is affected by the random seeds. The previous literatures [120] used a default random seed of 10,000 and the value specified should be of the same magnitude as the default value.

Appendix B

Energetic model of size effects in quasi-brittle rupture

For an intact structure, the criterion of material strength can indicate the crack propagation. On the other hand, the fracture toughness criterion can work on the prediction of large crack propagation. When the crack size is between these two situations, the prediction of rupture behaviour is an important research issue. Figure B.1 presents a plate with crack length a and finite width w, which suffered a remote uniform stress σ.

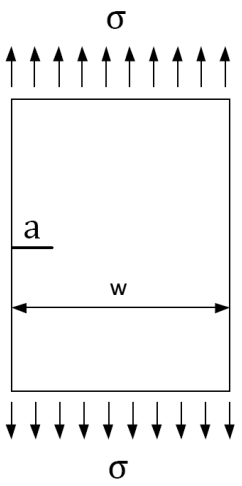

Figure B.1: Plate subjected to uniform tensile strength σ (Modified from [45]).

In Gao's study, the size effect [70, 110] and boundary effect [128–130], were combined and a general formula to predict the crack propagation for different crack sizes was presented as follows,

$$\left[\frac{H_\alpha \sigma_N}{1.12 f_t}\right]^{2r} + \left(\frac{G}{G_c}\right)^{r} = 1, \tag{B.1}$$

where H_α is material geometry factor, σ_N is the nominal failure stress, f_t is the tensile strength of material, G is the energy release rate, G_c is the critical energy release rate. After the reasonable derivation, Equation B.1 can be expressed as follows,

$$\left[\frac{dG/da}{max\, dG/da}\right]^{2r} + \left(\frac{G}{G_c}\right)^{r} = 1. \tag{B.2}$$

Figure B.2 presents the results of the energetic method in successfully description of the transition from the material strength to the LEFM criterion as crack length increases.

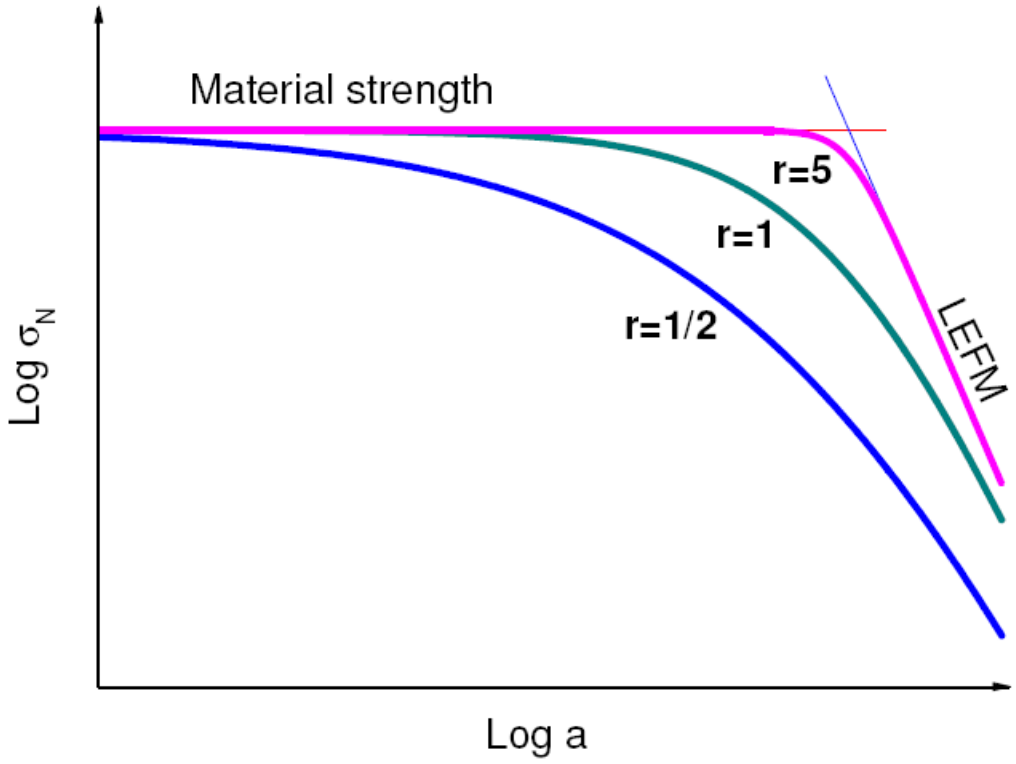

Figure B.2: Nominal strength σ_N as a function of crack length a for different r (Modified from [45]).

Appendix C

Implementation of the cohesive model in PFC

The proposed cohesive traction separation law (Section 4.3) is implemented in PFC 5.0 as a *user-defined* subroutine [120]. It is modified from an intrinsic contact *linearcbond* model in PFC. The source code of the force displacement law has been modified with $C++$ and then compiled as *Dynamic Link Library* (DLL) file so that PFC 5.0 can invoke it.

The logic flow for the calculation of damage and force is described in Figure C.1 for each contact at each time step: - The value of θ is obtained from the present force components by $\theta = arctan(f_n/f_s)$ and;

- K is obtained by Equation 4.9.

- The value of δ, δ_e and δ_{max} are taken into account on the calculation of the damage factor D (Equation 4.14) until the complete failure of contact ($D = 1$).

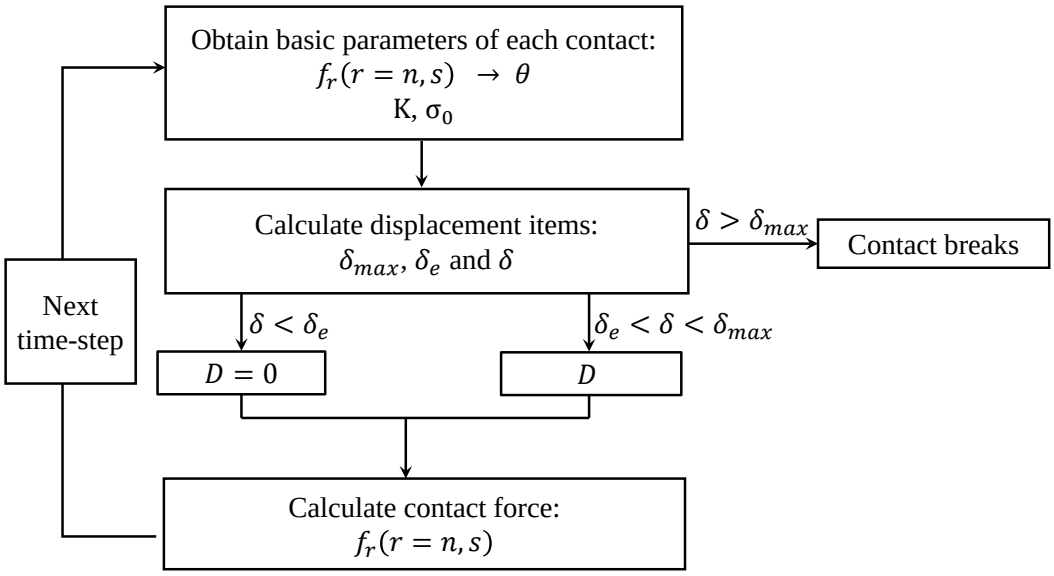

Figure C.1: Scheme of the algorithm for cohesive contact model implemented in PFC 5.0

Appendix D

Interface model applied in a wedge-splitting test without interface

The capacity of the interface model to capture the rupture mechanism in wedge-splitting geometry might go beyond the initial assumptions.

As an exemple, the WST results of [94] presented in Section 4.2.1 are analyzed by means of the interface model (IM), despite the fact the samples do not present any interface. In Figure D.1 the experimental results are compared to IM and to a complex bi-phasic DEM (MDEM) proposed by [94].

The IM geometry has been adjusted in terms of the height $H = 110\,mm$, width $w_i = 4\,mm$, thickness $t = 50\,mm$ and initial crack $a = 27.5\,mm$ to approximate the experiment's geometry shown in Figure 4.1a. The IM parameters: stiffness $E_i/w_i = 3.4 \times 10^{11} Pa/m$, tensile strength $\Sigma_i^t = 2.48 MPa$ and energy release rate $G_i = 238 N/m$ are adopted on the approximations. These values are very close to the parameters identified by the authors ($\Sigma^t = 2.81 MPa$ and $G_{IC} = 272 N/m$).

Despite the simplicity of the assumptions of IM, the shape of the curve $F_h \times \delta_h$ follows apparently better the experimental results than the complex MDEM proposed by the authors [94].

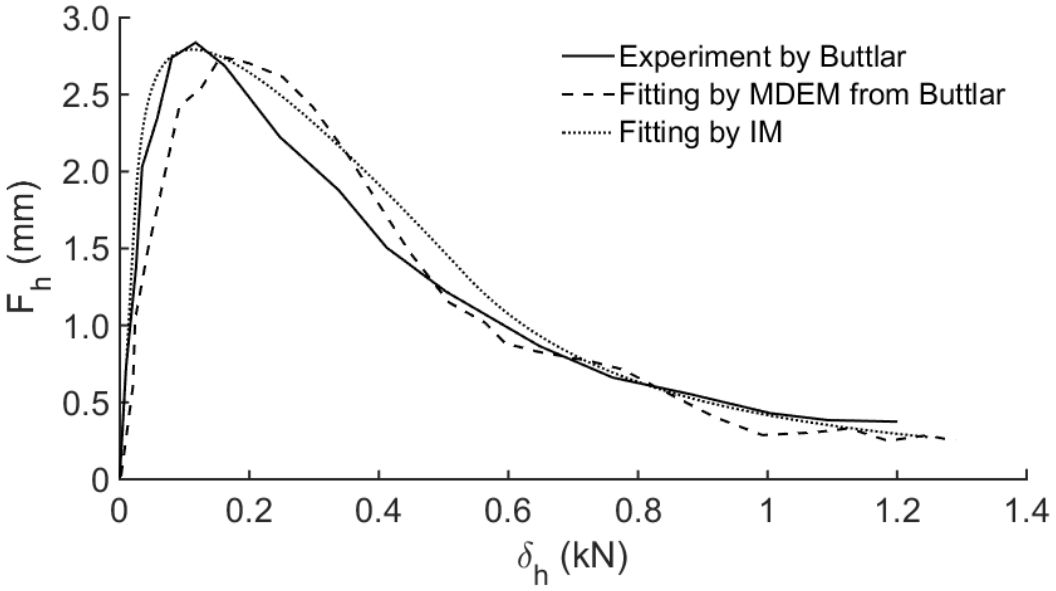

Figure D.1: Opening force F_h as a funtion of the displacement δ_h of WST from [94]. Experiments are compared to discrete element simulations from the authors (MDEM) and to IM.

Bibliography

[1] I.M. Arsenie. *Etude et modélisation des renforcements de chaussées à l'aide de grilles en fibre de verre sous sollicitations de fatigue*. PhD thesis, Université de Strasbourg, 2013. (Cited on pages xxv, 2, 10, 43, 44, 46, 58, 102, 103, 104, 109, 113, 114, 123, 124, 126, 129, 130, 136, 137, 138 and 141.)

[2] E. Masad, B. Muhunthan, N. Shashidhar, and T. Harman. Internal structure characterization of asphalt concrete using image analysis. *Journal of computing in civil engineering*, 13(2):88–95, 1999. (Cited on page 8.)

[3] Q. Guo, L. Li, Y. Cheng, Y. Jiao, and C. Xu. Laboratory evaluation on performance of diatomite and glass fiber compound modified asphalt mixture. *Materials & Design (1980-2015)*, 66:51–59, 2015. (Cited on pages 8 and 9.)

[4] Q. Ye, S. Wu, and N. Li. Investigation of the dynamic and fatigue properties of fiber-modified asphalt mixtures. *International Journal of Fatigue*, 31(10):1598–1602, 2009. (Cited on page 8.)

[5] S. Wu, Q. Ye, and N. Li. Investigation of rheological and fatigue properties of asphalt mixtures containing polyester fibers. *Construction and Building Materials*, 22(10):2111–2115, 2008. (Cited on page 9.)

[6] Z. Ge, H. Wang, Q. Zhang, and C. Xiong. Glass fiber reinforced asphalt membrane for interlayer bonding between asphalt overlay and concrete pavement. *Construction and Building Materials*, 101:918–925, 2015. (Cited on page 9.)

[7] X. Hu and L.F. Walubita. Modelling tensile strain response in asphalt pavements: Bottom-up and/or top-down fatigue crack initiation. *Road Materials and Pavement Design*, 10(1):125–154, 2009. (Cited on page 9.)

[8] M.L. Nguyen, J. Blanc, J.P. Kerzreho, and P. Hornych. Review of glass fibre grid use for pavement reinforcement and apt experiments at ifsttar. *Road Materials and Pavement Design*, 14(sup1):287–308, 2013. (Cited on pages 9, 10 and 11.)

[9] C. Bathias and C. Wolff. *Matériaux composites*. Dunod, 2005. (Cited on page 9.)

[10] J.W. Button and R.L. Lytton. Evaluation of fabrics, fibers and grids in overlays. In *INTERNATIONAL CONFERENCE ON THE STRUCTURAL DESIGN*, 1987. (Cited on page 10.)

[11] A. Vanelstraete and L. Francken. *Prevention of reflective cracking in pavements*. CRC Press, 2014. (Cited on page 11.)

[12] F.P. Jaecklin and J. Scherer. Asphalt reinforcing using glass fibre grid" glasphalt". In *RILEM PROCEEDINGS*, pages 268–277. CHAPMAN & HALL, 1996. (Cited on page 11.)

[13] H. Piber, F. Canestrari, G. Ferrotti, X. Lu, A. Millien, M. Partl, C. Petit, A. Phelipot-Mardelle, and C. Raab. Rilem interlaboratory test on interlayer bonding of asphalt pavements. In *7th International RILEM Symposium on Advanced Testing and Characterisation of Bituminous Materials. Rhodes, GREECE. MAY 27-29, 2009*, pages 1181–1189, 2009. (Cited on page 11.)

[14] R. Leutner. Untersuchung des schichtenverbundes beim bituminösen oberbau. *Bitumen*, 41(3), 1979. (Cited on page 11.)

[15] S. Vismara, A.A.A. Molenaar, M. Crispino, and M.R. Poot. Characterizing the effects of geosynthetics in asphalt pavements. In *7th RILEM International Conference on Cracking in Pavements*, pages 1199–1207. Springer, 2012. (Cited on page 11.)

[16] I.M. Arsenie, C. Chazallon, J.L. Duchez, and S. Mouhoubi. Modelling of the fatigue damage of a geogrid-reinforced asphalt concrete. *Road Materials and Pavement Design*, 18(1):250–262, 2017. (Cited on pages 11, 16, 17, 42, 44 and 46.)

[17] I.M. Arsenie, C. Chazallon, J.L. Duchez, and P. Hornych. Laboratory characterisation of the fatigue behaviour of a glass fibre grid-reinforced asphalt concrete using 4pb tests. *Road Materials and Pavement Design*, 18(1):168–180, 2017. (Cited on pages 11, 42, 44 and 46.)

[18] R.L. Lytton. Reinforcing fiberglass grids for asphalt overlays. *Texas Transportation Institute Report for Bay Mills Limited, Texas A&M University, College Station, Texas*, 1988. (Cited on page 11.)

[19] S.J. Lee. Mechanical performance and crack retardation study of a fiberglass-grid-reinforced asphalt concrete system. *Canadian Journal of Civil Engineering*, 35(10):1042–1049, 2008. (Cited on pages 11, 16 and 17.)

[20] T. Scullion and C. Von-Holdt. Performance report on jointed concrete pavement repair strategies in texas. Technical report, 2004. (Cited on page 11.)

[21] A.H. De Bondt. 20 years of research on asphalt reinforcement–achievements and future needs. In *7th RILEM International Conference on Cracking in Pavements*, pages 327–335. Springer, 2012. (Cited on page 11.)

[22] M. Gharbi, M.L. Nguyen, S. Trichet, and A. Chabot. Characterization of the bond between asphalt layers and glass grid layer with help of a wedge splitting test. In *10th International Conference on Bearing Capacity of Roads, Railways and Airfields (BCRRA 2017)*. CRC Press, 2017. (Cited on pages 11, 15, 58, 77, 80, 81 and 93.)

[23] C.M. Aldea and J.R. Darling. Effect of coating on fiberglass geogrid performance. In *Fifth International RILEM Conference on Reflective Cracking in Pavements*, pages 81–88. RILEM Publications SARL, 2004. (Cited on page 11.)

[24] S. Hakimzadeh, N.A. Kebede, W.G. Buttlar, S. Ahmed, and M. Exline. Development of fracture-energy based interface bond test for asphalt concrete. *Road materials and pavement design*, 13(sup1):76–87, 2012. (Cited on page 11.)

[25] T.L. Anderson. *Fracture mechanics: fundamentals and applications*. CRC press, 2017. (Cited on pages 12, 13 and 35.)

[26] ASTM Committee E08 on Fatigue and Fracture. *Standard test method for measurement of fracture toughness*. ASTM International, 2011. (Cited on page 14.)

[27] T. Nose and T. Fujii. Evaluation of fracture toughness for ceramic materials by a single-edge-precracked-beam method. *Journal of the American Ceramic Society*, 71(5):328–333, 1988. (Cited on page 14.)

[28] E. Brühwiler and F.H. Wittmann. The wedge splitting test, a new method of performing stable fracture mechanics tests. *Engineering fracture mechanics*, 35(1-3):117–125, 1990. (Cited on page 14.)

[29] E.K. Tschegg, R.J.A. Ehart, and M.M. Ingruber. Fracture behavior of geosynthetic interlayers in road pavements. *Journal of transportation engineering*, 124(5):457–464, 1998. (Cited on page 14.)

[30] H. Kim and W.G. Buttlar. Multi-scale fracture modeling of asphalt composite structures. *Composites Science and Technology*, 69(15-16):2716–2723, 2009. (Cited on page 14.)

[31] H. Kim, M.P. Wagoner, and W.G. Buttlar. Numerical fracture analysis on the specimen size dependency of asphalt concrete using a cohesive softening model. *Construction and Building Materials*, 23(5):2112–2120, 2009. (Cited on pages 14 and 37.)

[32] H. Kim and W.G. Buttlar. Discrete fracture modeling of asphalt concrete. *International Journal of Solids and Structures*, 46(13):2593–2604, 2009. (Cited on pages 14, 37, 40 and 41.)

[33] H. Kim, M.P. Wagoner, and W.G. Buttlar. Micromechanical fracture modeling of asphalt concrete using a single-edge notched beam test. *Materials and Structures*, 42(5):677, 2009. (Cited on pages 14 and 37.)

[34] M. Gharbi. *Caractérisation du collage des interfaces de chaussées par essais de rupture en mode I*. PhD thesis, École centrale de Nantes, 2018. (Cited on pages 15, 70, 80, 82, 84, 96, 97 and 98.)

[35] F. Moreno-Navarro and M.C. Rubio-Gámez. A review of fatigue damage in bituminous mixtures: Understanding the phenomenon from a new perspective. *Construction and Building Materials*, 113:927–938, 2016. (Cited on pages 15, 16 and 32.)

[36] Salvatore Mangiafico, Cédric Sauzeat, Hervé Di Benedetto, S Pouget, F Olard, and L Planque. Quantification of biasing effects during fatigue tests on asphalt mixes: non-linearity, self-heating and thixotropy. *Road Materials and Pavement Design*, 16(sup2):73–99, 2015. (Cited on page 15.)

[37] M. Sabouri and Y.R. Kim. Development of a failure criterion for asphalt mixtures under different modes of fatigue loading. *Transportation Research Record*, 2447(1):117–125, 2014. (Cited on page 15.)

[38] R. Reese. Properties of aged asphalt binder related to asphalt concrete fatigue life. *Journal of the Association of Asphalt Paving Technologists*, 66, 1997. (Cited on page 15.)

[39] S. Luo, Z. Qian, X. Yang, and Q. Lu. Fatigue behavior of epoxy asphalt concrete and its moisture susceptibility from flexural stiffness and phase

angle. *Construction and Building Materials*, 145:506–517, 2017. (Cited on pages 15 and 34.)

[40] B.W. Tsai, J. Harvey, and C. Monismith. Application of weibull theory in prediction of asphalt concrete fatigue performance. *Transportation Research Record: Journal of the Transportation Research Board*, (1832):121–130, 2003. (Cited on page 15.)

[41] V. Dattoma, S. Giancane, R. Nobile, and F.W. Panella. Fatigue life prediction under variable loading based on a new non-linear continuum damage mechanics model. *International Journal of Fatigue*, 28(2):89–95, 2006. (Cited on page 15.)

[42] K.P. Fathima and J.C. Kishen. A thermodynamic framework for fatigue crack growth in concrete. *International Journal of Fatigue*, 54:17–24, 2013. (Cited on pages 15 and 40.)

[43] D. Weichert and G. Maier. *Inelastic behaviour of structures under variable repeated loads: direct analysis methods*, volume 432. Springer, 2014. (Cited on page 16.)

[44] J. Zhang, W.Q. Shen, A. Oueslati, and G. De Saxce. Shakedown of porous materials. *International Journal of Plasticity*, 95:123–141, 2017. (Cited on page 16.)

[45] X. Gao. *Modelling of nominal strength prediction for quasi-brittle materials: application to discrete element modelling of damage and fracture of asphalt concrete under fatigue loading*. PhD thesis, Université de Strasbourg, 2017. (Cited on pages 16, 18, 44, 45, 46, 64, 147 and 148.)

[46] A.A. Griffith. The phenomena of rupture and flow in solids. *Philosophical transactions of the royal society of london. Series A, containing papers of a mathematical or physical character*, 221:163–198, 1920. (Cited on pages 18 and 23.)

[47] G.R. Irwin. Fracturing of metals. *ASM, Cleveland*, 147:19–9, 1948. (Cited on page 18.)

[48] H.M. Westergaard. Bearing pressures and cracks. *SPIE MILESTONE SERIES MS*, 137:18–22, 1997. (Cited on page 18.)

[49] C.T. Sun and Z.H. Jin. *Fracture Mechanics*. Academic Press. Academic Press, 2012. (Cited on pages 18, 20, 21, 23, 24, 27, 28, 29, 36, 59 and 71.)

[50] B.R. Lawn. *Fracture of brittle solids*. Cambridge solid state science series. Cambridge University Press, Cambridge ; New York, 2nd ed edition, 1993. (Cited on page 19.)

[51] P. Paris and F. Erdogan. A critical analysis of crack propagation laws. *Journal of basic engineering*, 85(4):528–533, 1963. (Cited on page 29.)

[52] J. Glucklich. Fracture of plain concrete. *Journal of the Engineering Mechanics Division*, 89(6):127–138, 1963. (Cited on page 30.)

[53] S. Kumar and S.V. Barai. Fracture mechanics of concrete–state-of-the-art review. In *Concrete Fracture Models and Applications*, pages 9–63. Springer, 2011. (Cited on page 30.)

[54] K.N. Derucher. Application of the scanning electron microscope to fracture studies of concrete. *Building and Environment*, 13(2):135–141, 1978. (Cited on page 30.)

[55] S. Mindess and S. Diamond. A preliminary sem study of crack propagation in mortar. *Cement and Concrete Research*, 10(4):509–519, 1980. (Cited on page 30.)

[56] S. Mindess and S. Diamond. A device for direct observation of cracking of cement paste or mortar under compressive loading within a scanning electron microscope. *Cement and Concrete Research*, 12(5):569–576, 1982. (Cited on page 30.)

[57] J. Bhargava and Å. Rehnström. High-speed photography for fracture studies of concrete. *Cement and Concrete Research*, 5(3):239–247, 1975. (Cited on page 30.)

[58] F. Ansari. Mechanism of microcrack formation in concrete. *ACI Materials Journal*, 86(5):459–464, 1989. (Cited on page 30.)

[59] X. Hu and F.H. Wittmann. Experimental method to determine extension of fracture-process zone. *Journal of Materials in Civil Engineering*, 2(1):15–23, 1990. (Cited on page 30.)

[60] Y. Sakata and M. Ohtsu. Crack evaluation in concrete members based on ultrasonic spectroscopy. *Materials Journal*, 92(6):686–698, 1995. (Cited on page 30.)

[61] A. Maji and S.P. Shah. Process zone and acoustic-emission measurements in concrete. *Experimental mechanics*, 28(1):27–33, 1988. (Cited on page 30.)

[62] K. Otsuka and H. Date. Fracture process zone in concrete tension specimen. *Engineering Fracture Mechanics*, 65(2-3):111–131, 2000. (Cited on pages 30, 31 and 35.)

[63] F. Wu. *Assessment of residual life of bituminous layers for the design of pavement strengthening.* PhD thesis, Polytechnic of Wales, 1992. (Cited on page 33.)

[64] M.A. Gul, M. Irfan, S. Ahmed, Y. Ali, and S. Khanzada. Modelling and characterising the fatigue behaviour of asphaltic concrete mixtures. *Construction and Building Materials*, 184:723–732, 2018. (Cited on pages 33, 34 and 40.)

[65] G.I. Barenblatt. The formation of equilibrium cracks during brittle fracture. general ideas and hypotheses. axially-symmetric cracks. *Journal of Applied Mathematics and Mechanics*, 23(3):622–636, 1959. (Cited on page 35.)

[66] D.S. Dugdale. Yielding of steel sheets containing slits. *Journal of the Mechanics and Physics of Solids*, 8(2):100–104, 1960. (Cited on page 35.)

[67] Z.P. Bažant and B.H. Oh. Crack band theory for fracture of concrete. *Matériaux et construction*, 16(3):155–177, 1983. (Cited on page 35.)

[68] Y. Jenq and S.P. Shah. Two parameter fracture model for concrete. *Journal of engineering mechanics*, 111(10):1227–1241, 1985. (Cited on page 35.)

[69] Y.S. Jenq and S.P. Shah. A fracture toughness criterion for concrete. *Engineering Fracture Mechanics*, 21(5):1055–1069, 1985. (Cited on page 35.)

[70] Z.P. Bažant. Size effect in blunt fracture: concrete, rock, metal. *Journal of Engineering Mechanics*, 110(4):518–535, 1984. (Cited on pages 35 and 147.)

[71] P. Nallathambi and B.L. Karihaloo. Determination of specimen-size independent fracture toughness of plain concrete. *Magazine of Concrete Research*, 38(135):67–76, 1986. (Cited on page 35.)

[72] S. Xu. Determination of parameters in the bilinear, reinhardt's non-linear and exponentially non-linear softening curves and their physical meanings. werkstoffe und werkstoffprüfung im bauwesen, hamburg. *Libri Bod*, 15:410–424, 1999. (Cited on page 35.)

[73] S. Xu and X. Zhang. Determination of fracture parameters for crack propagation in concrete using an energy approach. *Engineering Fracture Mechanics*, 75(15):4292–4308, 2008. (Cited on page 35.)

[74] M.F. Kanninen and C.L. Popelar. Advanced fracture mechanics. 1985. (Cited on page 35.)

[75] Z.P. BazÏant and L. Cedolin. Stability of structures. *ASME Appl. Mech. Rev.(submitted)*, 1991. (Cited on page 35.)

[76] S. Suresh. *Fatigue of materials*. Cambridge university press, 1998. (Cited on page 35.)

[77] K.B. Broberg. *Cracks and fracture*. Elsevier, 1999. (Cited on page 35.)

[78] K. Park and G.H. Paulino. Cohesive zone models: a critical review of traction-separation relationships across fracture surfaces. *Applied Mechanics Reviews*, 64(6):060802, 2011. (Cited on pages 35, 36, 38 and 73.)

[79] H.A. Elliott. An analysis of the conditions for rupture due to griffith cracks. *Proceedings of the Physical Society*, 59(2):208, 1947. (Cited on page 35.)

[80] A. Hillerborg, M. Modéer, and P.E. Petersson. Analysis of crack formation and crack growth in concrete by means of fracture mechanics and finite elements. *Cement and concrete research*, 6(6):773–781, 1976. (Cited on page 36.)

[81] T.J. Boone, P.A. Wawrzynek, and A.R. Ingraffea. Simulation of the fracture process in rock with application to hydrofracturing. In *International Journal of Rock Mechanics and Mining Sciences & Geomechanics Abstracts*, volume 23, pages 255–265. Elsevier, 1986. (Cited on page 36.)

[82] M.G.G.V. Elices, G.V. Guinea, J. Gomez, and J. Planas. The cohesive zone model: advantages, limitations and challenges. *Engineering fracture mechanics*, 69(2):137–163, 2002. (Cited on page 36.)

[83] Z.P. Bažant and E. Becq-Giraudon. Statistical prediction of fracture parameters of concrete and implications for choice of testing standard. *Cement and concrete research*, 32(4):529–556, 2002. (Cited on page 36.)

[84] J. Roesler, G.H. Paulino, K. Park, and C. Gaedicke. Concrete fracture prediction using bilinear softening. *Cement and Concrete Composites*, 29(4):300–312, 2007. (Cited on page 36.)

[85] G.T. Camacho and M. Ortiz. Computational modelling of impact damage in brittle materials. *International Journal of solids and structures*, 33(20-22):2899–2938, 1996. (Cited on pages 37 and 74.)

[86] P.H. Geubelle and J.S. Baylor. Impact-induced delamination of composites: a 2d simulation. *Composites Part B: Engineering*, 29(5):589–602, 1998. (Cited on pages 37 and 74.)

[87] H.D. Espinosa and P.D. Zavattieri. A grain level model for the study of failure initiation and evolution in polycrystalline brittle materials. part i: Theory and numerical implementation. *Mechanics of Materials*, 35(3-6):333–364, 2003. (Cited on pages 37 and 74.)

[88] P.E. Petersson. Crack growth and development of fracture zones in plain concrete and similar materials. 1981. (Cited on page 37.)

[89] F.H. Wittmann, K. Rokugo, E. Brühwiler, H. Mihashi, and P. Simonin. Fracture energy and strain softening of concrete as determined by means of compact tension specimens. *Materials and Structures*, 21(1):21–32, 1988. (Cited on page 37.)

[90] V. Tvergaard. Theoretical investigation of the effect of plasticity on crack growth along a functionally graded region between dissimilar elastic–plastic solids. *Engineering Fracture Mechanics*, 69(14-16):1635–1645, 2002. (Cited on page 37.)

[91] I. Scheider and W. Brocks. Simulation of cup–cone fracture using the cohesive model. *Engineering Fracture Mechanics*, 70(14):1943–1961, 2003. (Cited on page 37.)

[92] V. Tvergaard. Effect of fibre debonding in a whisker-reinforced metal. *Materials science and engineering: A*, 125(2):203–213, 1990. (Cited on page 37.)

[93] M. Ortiz and A. Pandolfi. Finite-deformation irreversible cohesive elements for three-dimensional crack-propagation analysis. *International journal for numerical methods in engineering*, 44(9):1267–1282, 1999. (Cited on page 37.)

[94] H. Kim and W.G. Buttlar. Micromechanical fracture modeling of asphalt mixture using the discrete element method. In *Advances in Pavement Engineering*, pages 1–15. 2005. (Cited on pages 37, 71, 151 and 152.)

[95] H. Kim, M.P. Wagoner, and W.G. Buttlar. Simulation of fracture behavior in asphalt concrete using a heterogeneous cohesive zone discrete element model. *Journal of Materials in Civil Engineering*, 20(8):552–563, 2008. (Cited on pages 37, 39 and 72.)

[96] C.L Monismith and J.A. Deacon. Fatigue of asphalt paving mixtures. *Transportation Engineering Journal of ASCE*, 95(2):317–346, 1969. (Cited on page 40.)

[97] N.H. Nguyen, H.H. Bui, J. Kodikara, S. Arooran, and F. Darve. A discrete element modelling approach for fatigue damage growth in cemented materials. *International Journal of Plasticity*, 2018. (Cited on pages 40, 95 and 144.)

[98] R.Y. Liang and J. Zhou. Prediction of fatigue life of asphalt concrete beams. *International journal of fatigue*, 19(2):117–124, 1997. (Cited on page 40.)

[99] L. Gao and C.T.T. Hsu. Fatigue of concrete under uniaxial compression cyclic loading. *Materials Journal*, 95(5):575–581, 1998. (Cited on page 40.)

[100] D. Bodin. Modèle d'endommagement cyclique: Application à la fatigue des enrobés bitumineux. *PhD, University of Nantes (In French) Google Scholar*, 2002. (Cited on pages 41, 42, 102, 105 and 118.)

[101] M.H.J.W. Paas. *Continuum damage mechanics with an application to fatigue*. PhD thesis, Eindhoven University of Technology, The Netherlands, 1990. (Cited on pages 42, 105 and 106.)

[102] D. Bodin, G. Pijaudier-Cabot, C. de La Roche, and A. Chabot. A continuum damage approach of asphalt concrete fatigue tests. In *15th ASCE engineering mechanics conference*, pages 2–5. Columbia University New York, USA, 2002. (Cited on pages 42 and 105.)

[103] P.A. Cundall and O.D. Strack. A discrete numerical model for granular assemblies. *geotechnique*, 29(1):47–65, 1979. (Cited on page 48.)

[104] K. Bagi. An algorithm to generate random dense arrangements for discrete element simulations of granular assemblies. *Granular Matter*, 7(1):31–43, 2005. (Cited on pages 52 and 53.)

[105] B. Yang, Y. Jiao, and S. Lei. A study on the effects of microparameters on macroproperties for specimens created by bonded particles. *Engineering Computations*, 23(6):607–631, 2006. (Cited on pages 52, 54, 55, 56 and 57.)

[106] D.O. Potyondy and P.A. Cundall. A bonded-particle model for rock. *International journal of rock mechanics and mining sciences*, 41(8):1329–1364, 2004. (Cited on pages 52, 53, 54, 59, 61 and 144.)

[107] J. Yoon. Application of experimental design and optimization to pfc model calibration in uniaxial compression simulation. *International Journal of Rock Mechanics and Mining Sciences*, 44(6):871–889, 2007. (Cited on pages 53, 54, 56 and 57.)

[108] C. Ergenzinger, R. Seifried, and P. Eberhard. A discrete element model to describe failure of strong rock in uniaxial compression. *Granular Matter*, 13(4):341–364, 2011. (Cited on page 54.)

[109] C.J. Coetzee. Calibration of the discrete element method. *Powder Technology*, 310:104–142, 2017. (Cited on page 54.)

[110] Z.P. Bazant. Probabilistic modeling of quasibrittle fracture and size effect. In *Proc., 8th Int. Conf. on Structural Safety and Reliability (ICOSSAR)*, pages 1–23. Swets and Zeitinger, Balkema, 2001. (Cited on pages 59 and 147.)

[111] X. Gao, G. Koval, and C. Chazallon. Energetical formulation of size effect law for quasi-brittle fracture. *Engineering Fracture Mechanics*, 175:279–292, 2017. (Cited on pages 59 and 64.)

[112] B.D. Le, G. Koval, and C. Chazallon. Discrete element model for crack propagation in brittle materials. *International Journal for Numerical and Analytical Methods in Geomechanics*, 40(4):583–595, 2016. (Cited on page 63.)

[113] B.D. Le, G. Koval, and C. Chazallon. Discrete element approach in brittle fracture mechanics. *Engineering Computations*, 30(2):263–276, 2013. (Cited on pages 63 and 143.)

[114] H. Tada, P.C. Paris, and G.R. Irwin. The stress analysis of cracks. *Handbook, Del Research Corporation*, 1973. (Cited on pages 64, 72 and 73.)

[115] J.E. Srawley. Wide range stress intensity factor expressions for astm e 399 standard fracture toughness specimens. *International Journal of Fracture*, 12(3):475–476, 1976. (Cited on pages 65 and 66.)

[116] H.D. Benedetto, C. De La Roche, and L. Francken. Fatigue of bituminous mixtures: Different approaches and rilem interlaboratory tests. *Mechanical Tests for Bituminous Materials*, pages 15–26, 1997. (Cited on page 104.)

[117] M.N. Partl, D. SYBILSKI, J.B. Sousa, H. Di Benedetto, and H. Piber. Current research projects of the new rilem tc peb" performance testing and evaluation of bituminous materials". In *PROCEEDINGS OF THE PAPERS SUBMITTED FOR REVIEW AT 2ND EURASPHALT AND EUROBITUME CONGRESS, HELD 20-22 SEPTEMBER 2000, BARCELONA, SPAIN. BOOK 1-SESSION 1*, 2000. (Cited on page 104.)

[118] D. Bodin, G. Pijaudier-Cabot, C. de La Roche, J.M. Piau, and A. Chabot. Continuum damage approach to asphalt concrete fatigue modeling. *Journal of Engineering Mechanics*, 130(6):700–708, 2004. (Cited on page 105.)

[119] B.C. Le, J.F. Dubé, G. Pijaudier-Cabot, and B. Gérard. Calibration of nonlocal damage model from size effect tests. *European Journal of Mechanics-A/Solids*, 22(1):33–46, 2003. (Cited on page 105.)

[120] PFC 5.0 Itasca. User manual. In *Itasca Consulting group, Inc.* Washington DC, United State, 2014. (Cited on pages 110, 143, 144, 145, 146 and 149.)

[121] T.A. Dinh. Etude de la fatigue de grilles en fibre de verre. *Projet de fin d'études, Ecoles des Mines de Douai*, 2018. (Cited on pages 127 and 142.)

[122] F.P. Beer, E.R. Johnston, J.T. DeWolf, and D.F. Mazurek. Mechanics of materials. *MacGraw-Hill Engineering Series,*, 1992. (Cited on page 128.)

[123] J.K. Morgan and M.S. Boettcher. Numerical simulations of granular shear zones using the distinct element method: 1. shear zone kinematics and the micromechanics of localization. *Journal of Geophysical Research: Solid Earth*, 104(B2):2703–2719, 1999. (Cited on page 143.)

[124] P. Cleary. Modelling comminution devices using dem. *International Journal for Numerical and Analytical Methods in Geomechanics*, 25(1):83–105, 2001. (Cited on page 143.)

[125] G. Koval, J.N. Roux, A. Corfdir, and F. Chevoir. Annular shear of cohesionless granular materials: From the inertial to quasistatic regime. *Physical Review E*, 79(2):021306, 2009. (Cited on page 143.)

[126] K. Meguro and M. Hakuno. Fracture analyses of concrete structures by the modified distinct element method. *Doboku Gakkai Ronbunshu*, 1989(410):113–124, 1989. (Cited on page 143.)

[127] Y. Matsuda and Y. Iwase. Numerical simulation of rock fracture using three-dimensional extended discrete element method. *Earth, planets and space*, 54(4):367–378, 2002. (Cited on page 143.)

[128] X. Hu and F. Wittmann. Size effect on toughness induced by crack close to free surface. *Engineering fracture mechanics*, 65(2-3):209–221, 2000. (Cited on page 147.)

[129] X. Hu. An asymptotic approach to size effect on fracture toughness and fracture energy of composites. *Engineering Fracture Mechanics*, 69(5):555–564, 2002. (Cited on page 147.)

[130] K. Duan, X. Hu, and F.H. Wittmann. Scaling of quasi-brittle fracture: Boundary and size effect. *Mechanics of Materials*, 38(1-2):128–141, 2006. (Cited on page 147.)

Guixian LIU

Discrete element modelling of asphalt concrete reinforced with fiber glass grids.

Résumé

L'effet du renforcement de la grille en fibre de verre sur le béton bitumineux est étudié numériquement par la méthode des éléments discrets. En ce qui concerne les matériaux quasi-fragiles, l'élasticité de la modélisation est calibrée et le comportement à la rupture est vérifié par une mécanique de la rupture élastique Le comportement et la défaillance de l'interface prédominent dans la fracture des échantillons, ce qui donne lieu à un modèle d'interface simplifié. L'étalonnage des paramètres sur le module de Young et le coefficient de Poisson est effectué entre le modèle d'interface et la méthode des éléments discrets. Grâce à l'ajustement avec les résultats expérimentaux, la résistance de l'interface et le taux de libération d'énergie sont également identifiés par la méthode des éléments discrets et un modèle d'interface simplifié. En comparaison avec la mécanique de la rupture élastique linéaire, la rupture de l'interface présente une plus grande quantité du taux de libération d'énergie. La force et le taux de libération d'énergie sont réduits en raison de l'application de la grille en fibre de verre. Le comportement en fatigue est étudié à l'aide de simulations d'essais de fatigue en flexion en 4 points. Le modèle de fatigue de Bodin 'L2R' est adapté à la méthode des éléments discrets. L'effet de chaque paramètre sur l'évolution des dommages est étudié séparément. L'effet d'interface est observé lors de la prolongation de la résistance à la fatigue de toutes les phases. Les essais monotoniques et les essais de fatigue indiquent qu'une bonne liaison entre deux couches de béton bitumineux est importante pour la résistance de rupture.

Mots-clés: béton bitumineux; renforcement par des grille en fibre de verre; rupture; la vie de fatigue; modélisation d'éléments discrets

Abstract

The effect of fiberglass grid reinforcement in asphalt concrete is studied numerically by discrete element method in this work. Firstly, concerning on the quasi-brittle material, the elasticity of modelling are calibrated, and the rupture behaviour is verified with linear elastic fracture mechanics. Then the simulations of wedge splitting tests are performed under monotonic load. The interface elasticity and failure dominate in the fracture propagation of samples, which gives rise to a simplified interface model. The parameter calibration on Young's modulus and Poisson's ratio is conducted between interface model and discrete element method. Through the fitting with experimental results, the interface strength and energy release rate are also identified by discrete element method and simplified interface model. Comparing with linear elastic fracture mechanics, the interface rupture presents more released energy. The strength and energy release rate are reduced because of the application of the fiber glass grid. The fatigue behaviour is studied by simulations of 4-point bending fatigue tests. Bodin's fatigue model 'L2R' is adapted with discrete element method. The effect of each parameter on the damage evolution is studied respectively. The fiber glass grid helps to extent the fatigue life mainly after the fatigue cracks cross the grid. The interface effect is observed on prolonging the fatigue life of all the phases. From both monotonic and fatigue tests, it indicates that good bonding between two asphalt concrete layers is important to the resistance of rupture.

Keywords: asphalt concrete; fiber glass grid reinforcement; rupture; fatigue life; discrete element modelling